THE EFFECT OF BUFFER THERAPY ON THE ACID-MEDIATED TRANSITION TO MALIGNANCY: A MATHEMATICAL MODEL OF ACIDOSIS IN SPHEROID AND XENOGRAFT CULTURE

Mathematics

Honors Thesis

by

Frederika Rentzeperis

DARTMOUTH COLLEGE

Hanover, New Hampshire

May 28, 2020

Abstract

This thesis consists of the expansion and development of a model of cancer growth with vasculature to include acidification of the tumor microenvironment and an acid mediated transition to malignancy via the acquisition of acid resistance and the use of constitutive glycolysis. This model has been parametrized using data from transgenic adenocarcinoma of the mouse prostate, or TRAMP mice which spontaneously develop prostate adenocarcinoma, the most common form of prostatic cancer in humans. The results of simulations using this model match prostate cancer data in monolayers, spheroids, and *in vivo* and show tumor responses to early and late buffer therapy which match the results observed in the lab - early intervention with sodium bicarbonate is sufficient to stop the development of malignancy but treatment just six weeks later does not hinder malignancy. Unexpectedly, the late administration of buffer therapy in this model resulted in a greater proportion of malignant cells in the tumor than in tumors without treatment, suggesting that late buffer therapy may result in worse outcomes. Additionally, simulations under varied angiogenic conditions were carried out to explore the various behaviors of the model and three behaviors emerged - tumor death, a tumor volume equilibrium, and unlimited tumor growth, all of which are observed physiologically.

Acknowledgements

I would like to thank my advisor, Professor Dorothy Wallace, for her unwavering support of this thesis and for her help with its many iterations and parametrizations. Additionally, Dr. Bob Gatenby, Dr. Bob Gillies, and Dr. Arig Ibrahim-Hashim were the sources of many of the hypotheses and data from which this project was developed; without their help this research project would not have been possible. I also would like to thank Dr. Heiko Enderling for challenging us at Moffitt to automate the parameter optimization process via a genetic algorithm and Bradley Fox for his contributions to the genetic algorithm used in this study.

Contents

List of Figures

Chapter 1

Literature Review

Section 1.1

Introduction

It is known that acidosis is a consequence of tumor growth, the effects of which may be measured directly on the surface of a tumor[1]. Two studies have shown that alkalinization can delay the progress of prostate cancer and reduce the development of malignancy [2, 3]. Both of these phenomena are consistent with the hypotheses put forth about the role of acid in tumor progression and the competitive nature of cancer phenotypes and genotypes. Specifically, it has been suggested that increasing acidosis, a natural consequence of hypoxic regions in the tumor, both encourages the appearance of acid resistance, selects for acid resistant strains in a passive Darwinian process, and thereby produces malignancy via the Warburg effect [4].

During early tumor growth prior to angiogenesis, central regions of the tumor become hypoxic because oxygen is unable to diffuse to the center of the tumor, thereby preventing complete progression through the Krebs cycle/oxidative phosphorylation.

This lack of oxygen means there are too few oxygen atoms to serve as electron receptors which causes ATP levels to decline, thus forcing the cells to become quiescent *i.e.* temporarily frozen in the G_0 phase of the cell cycle. This hypoxic, nutrient poor, tumor microenvironment selects for glycolysis to enable cells to continue proliferating, which acidifies the extracellular environment, further increasing its hostility. In addition to altering the phenotype of cells, these environmental factors destabilize the genome of cells introducing mutation and increasing the genetic diversity of cells within the tumor[5].

Additionally, the acid degrades extracellular matrix (ECM) permitting tumor cells to invade thus further accelerating their approach toward malignancy. The article by Damaghi et al., develops an acid-mediated invasion model through long term experiments in which premalignant cancer cells were cultured at low pH. The protein LAMP2 is upregulated which is important as it typically is heavily glycosylated and present on lysosomal membranes to protect them from hydrolysis by the acid in the lumen of the lysosomes [6]. In acid resistant cancer cells, they saw both an upregulation of LAMP2 and a relocalization of LAMP2 protein to the cell membrane. They found that in becoming adapted, tumor cells become aggressive and migratory; the more acidic central portion of the tumor is initially the highest proportion of malignant cells but these cells eventually migrate toward the perimeter of the tumor and outcompete other cells. These experimental results indicating acid resistance and tumor aggressiveness in the presence of acid support the study presented here.

The model proposed in this paper is motivated largely by Fang et al. which describes a model of carcinogenesis through which cells must experience acidosis and related acid resistance in order to become malignant, shown schematically in Fig-

ure 1.1. [7]

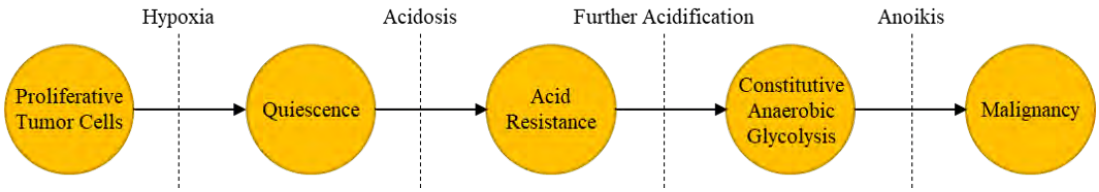

Figure 1.1: The progression to malignancy as described in (Fang et al)

A qualitative description of Figure 1.1 can be summarized as:

(a) transition from proliferation to quiescence due to hypoxia

(b) phenotypic change from quiescent hypoxic cells to acid resistant cells in acidic and hypoxic surroundings

(c) further phenotypic and/or genotypic change to acid resistant anaerobic glycolysis in acidic surroundings, consistent with the development of malignancy

(d) selection for acid resistant phenotypes, increased aggression associated with cell motility, and faster aerobic glycolysis

Prostate cancers are globally the second most common cancer to affect men and the most common cancer in men in the United Kingdom.[8] This prevalence and the high death rate associated with prostate cancers are likely connected to the lack of symptoms in early cancers – they often go undetected until they are more advanced. For this reason, screening for Prostate Specific Antigen (PSA) which increases rapidly upon the emergence of prostate cancers has been employed but overdiagnosis and unnecessary treatment of cancers which may never have progressed has garnered considerable controversy around the use of this early detection method.[9] Additionally, the treatments which have become the standard of care for prostate cancer – surgery,

radiotherapy, and proton beam therapy – are associated with significant side effects so alternative therapy options are being explored.[11] Because the prostate is comprised primarily of glandular tissue, more than 95% of prostate cancers are adenocarcinoma, so a model calibrated to experiments from a mouse model of prostate adenocarcinoma and buffer therapies to combat the acidifying tumor environment will be developed and analyzed in this thesis.

Section 1.2

Tumor Growth Modeling

Mathematical modeling in biology and specifically oncology is beneficial as it allows for the exploration of biological systems without the use of time consuming and expensive bench research, both of which are especially pertinent to *in vivo* experiments. Moreover, math models serve as a means to further explore the impacts of various aspects of cancers such as the rates of angiogenesis or the relative impacts of TNF-α and acidosis, which are difficult to manipulate and measure in the lab but are nevertheless central to the behaviors of cancer. To model tumor growth, data from experiments at increasing levels of complexity are utilized to establish a model parametrization that can capture behaviors at the cellular and whole tumor level. First, data for a monolayer is used to establish the transition between cell cycle stages and the rates of tumor cell development, then a spheroid is used to first model solid tumor growth without the added complexity of vasculature. Next, measurements of pH are used to determine the parameter values associated with acidification and the acquisition of malignancy, and finally, data from xenotransplanted tumor cells in a mouse flank and the spontaneously arising tumors in transgenic adenocarci-

noma of the mouse prostate (TRAMP mice) are used to develop the full model. The characteristics of the levels of the model are described below.

1.2.1. Monolayer

One mode of studying cellular behavior involves culturing cells in a flat dish under highly controlled conditions which thus enables monitoring of the relative prevalence of the various cell cycle stages and a determination of the doubling time for the cells. Monolayer cultures provide an opportunity to model short-term, essentially unconstrained exponential cell growth, since the only limiting factors are nutrient availability (which can experimentally be made sufficiently large to not constrain growth) and space which is remedied through cell passaging or restriction of monitoring to a short time window.

Monolayer growth and the cell cycle are easily described by a three-dimensional linear model.[12] The monolayer is parametrized by treating the unsynchronized cell cycle limiting distribution as an eigenvector of the system with the eigenvalue $\lambda = \frac{\ln(2)}{\text{Doubling Time}}$. Three parameters c_1, c_s, and c_2, correspond to a transition rate between stages of the cell cycle and d_a is the natural death rate which, for this model, is taken to be 0. The values G_1^*, G_2^*, and S^* represent the proportions of cells in each stage. These equations are reproduced from He et al. below:

$$c_2 = \frac{(\lambda + d_a G_2^*)}{G_2^*}$$
$$c_1 = \frac{(2c_2 G_2^* - \lambda G_1^*)}{G_1^*}$$
$$c_s = \frac{(c_1 G_1^* - \lambda S^*)}{S^*}$$

1.2.2. Spheroid

Because solid tumors in the body are three-dimensional, 2D monolayer cultures are inadequate to capture all of the characteristics of a tumor. Specifically, cells grown in a monolayer lack the cell-cell interactions and the microenvironmental differences between a cell on the outside and one in the center of a cluster of cells. A somewhat more complex model of tumor development that is evaluated in the lab are multi-cellular tumor spheroids (MCTS) - spherical cellular aggregates comprised of one or more cell types that effectively represent avascular tumors up to roughly one cubic millimeter in size.[13] MCTS greater than $500\mu m$ in diameter exhibit physiochemical gradients similar to small metastases in the body including the gradient of oxygen, metabolic wastes, and nutrients and can thus capture patterns of quiescence, hypoxia, and acidosis observed in tumors in the body.

When MCTS are cut in cross-section, they exhibit a characteristic pattern of three concentric layers of cells: a necrotic core surrounded by a layer of quiescent cells which receive inadequate nutrients and oxygen to divide, further surrounded by a layer of proliferative cells on the surface of the spheroid where oxygen and nutrients are abundant.[14] Nutrients and oxygen exist in a gradient with the greatest concentrations in the proliferative layer nearest the culture media and very low levels within the quiescent and necrotic regions; the gradient of lactic acid is opposite with acid accumulation in the center of the MCTS and relatively low acid levels in the proliferative region.[14] In order to commit to cellular division, cells must overcome specific energy barriers, and in cells with inadequate access to oxygen this is impossible so the cells arrest their cycle in the G_0 phase in which they do not divide.[15] As such, the development of quiescence is modeled as a transition from the G_1 phase to the

quiescent compartment and the return to the cell cycle is modeled as a transition from quiescence into the S phase. In spheroids, there is a critical depth which varies by cell type below which cells can no longer proliferate and thus a quiescent layer develops; with further oxygen deprivation, cells can no longer survive so they become necrotic thereby generating a necrotic core. A model of spheroid growth is expected to meet certain qualitative observations common to all spheroids: an equilibrium for the radius of the proliferating and quiescent shells as well as a cessation of growth. A visualization of the three MCTS layers is presented in Figure 1.2.

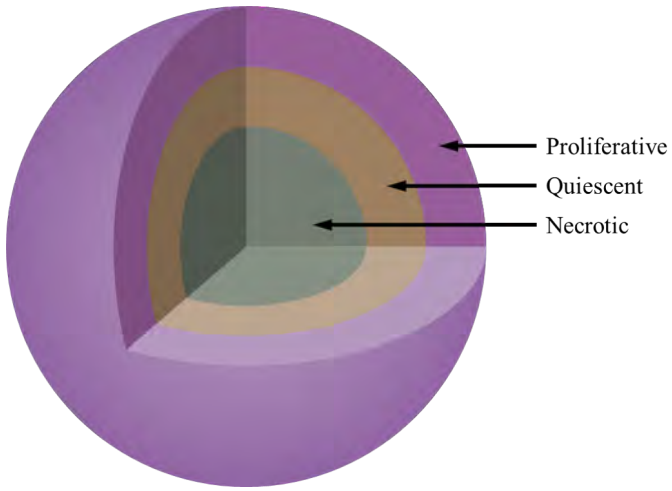

Figure 1.2: A visual representation of a spheroid indicating the relative positions of the proliferative layer, quiescent layer, and the necrotic core. The level of oxygen and pH decline moving from the outside toward the core.

1.2.3. Xenograft

The most complex and thus the most similar experimental system to human tumors are *in vivo* studies which take place in the body of an animal. Several options to study tumor growth *in vivo* include xenotransplantation or the insertion of human cells into nude mice which lack an immune system, xenotransplantation of tumor

cells from one location of an animal's body to a location with more favorable conditions to study, or the use of either carcinogenic agents or transgenic mice that will spontaneously develop cancers. For this thesis, data from studies using transgenic TRAMP mice which spontaneously develop adenocarcinoma in their prostates and xenotransplantation of TRAMP prostate cancer cells from the prostate to the flank where they can more readily be monitored are considered.

Because these studies take place in the body, there is no longer an avascular constraint as in the spheroids. The tumors experience two phases, first an avascular phase that lacks its own blood supply and matches the spheroids in most aspects except nutrient availability, and a later vascular phase which is most similar to the tumors that are detected in people.[16] The model for the xenograft thus includes a compartment for vascular endothelial growth factor (VEGF) which is secreted under low oxygen conditions to signal for the addition of vasculature. In the spheroid there is considerable accumulation of acid due to the glycolytic activity of the tumor cells and TNF-α which is secreted by necrotic cells in the necrotic core region. In the body the vasculature carries away both necrosis and acid making this a more representative means of modeling the role of acid in tumor malignancy.

Section 1.3

Cancer Physiology - VEGF and TNF-α

Metastasis and growth of cancers is closely linked to vascularization of the tumor – without access to blood vessels, solid tumors cannot reliably grow larger than a few millimeters in size and thus are not of considerable concern.[17] One of the major secretable factors employed by tumors is vascular endothelial growth factor

(VEGF) which is a glycoprotein that is over-expressed in pancreatic cancers among others and is closely associated to disease progression and angiogenesis.[17] VEGF has several roles in angiogenesis, first involving upregulation of enzyme secretion for basement membrane and extracellular matrix degradation, followed by upregulation of endothelial cell proliferation and maintenance of the new vessels.[18] Therapies targeting VEGF have been shown to slow angiogenesis considerably thereby confirming its role in the development of blood vessels in cancers, but the effect of these therapies is limited and tumors will begin to secrete other factors to signal for blood vessels, thereby evading these therapies.[19] As it pertains to acidosis, VEGF was found to increase endothelial proliferation at physiological pH (7.4) but had diminishing effect on endothelial cell proliferation with decreasing pH and zero effect at pH 6.4.[19]

Another secretable factor which is important to tumor development and is thus incorporated into the model is Tumor Necrosis Factor alpha (TNF-α). In relatively simple models of spheroids, the presence of TNF$-\alpha$ along with depleted oxygen and nutrient conditions is adequate to generate results that match data for spheroid growth thus suggesting its importance.[20] TNF-α is secreted by necrotic cells and plays dual and seemingly contradictory roles in oncology – it is implicated in the stimulation of angiogenesis as evidenced by upregulated VEGF mRNA in the presence of TNF-α but also induces cancer cell apoptosis.[21, 22] Thus, TNF-α is implicated both in tumor regression through cell death and in the recruitment of vasculature which can prevent the otherwise imminent death of quiescent cells experiencing severe hypoxia and nutrient deprivation thereby resulting in tumor growth. Both of these factors are included as compartments in the model described in this thesis in arbitrary units.

Section 1.4

Tumor Metabolism and the Warburg Effect

Under typical conditions, vascularized tissue receives sufficient oxygen for its cells to maximize the energy gained from glucose through glycolysis, the mitochondrial tricarboxylic acid (TCA) cycle and subsequent oxidative phosphorylation in the mitochondria .[23] As such, well oxygenated cells maintain their cellular processes by maximizing the utility of the glucose they receive, but do not take up more glucose than they require. Otto Warburg noted that even in the presence of adequate oxygen, cancer cells often take up considerably more glucose than they require and ferment the resultant pyruvate from glycolysis into lactic acid instead of further oxidizing it in the TCA cycle .[24] As a result, the pH of the tumor, surrounding tissue, and eventually the entire body decreases as the tumor becomes more aggressive. The use of glycolysis in the presence of oxygen is considerably less efficient than progressing completely through oxidative phosphorylation, yielding 2 ATP molecules per molecule of glucose as opposed to 36 and the cause of this switch to constitutive glycolysis is thus a point of interest.[23]

Some hypotheses as to why cells switch to a less efficient metabolic strategy are outlined by Heiden et al. and summarized here. It is possible that while non-proliferating cells evolved to maximize their use of glucose to account for the scarcity of resources, proliferating cells in the body are exposed to an essentially constant source of nutrients; thus cancers that have undergone the Warburg effect have access to sufficient glucose to maintain a high ratio of ATP to ADP using aerobic glycolysis regardless of how frequently they divide. This thesis explores one possible explana-

tion for constitutive glycolysis as a competitive strategy for the cancer which enables malignant cells to secrete acid and withstand acidification better than their non-malignant proliferating counterparts. Because of the rapidity with which the tumor cells convert to acid resistance and subsequently malignancy, it is assumed that the acquisition of acid resistance in acidified hypoxic conditions is phenotypic but irreversible, quiescence is a reversible phenotypic change, and malignancy can be either phenotypic or genotypic and is associated with increased motility and other hallmarks of cancer.

To complement their evaluation of prostate tumor response to buffer therapy at various buffer concentrations, Ibrahim-Hashim et al. 2017 carried out an analysis of breast cancer xenografts and spheroids. For this experiment, they generated a well mixed combination of two breast cancer cell lines, the non- invasive MCF-7 and the highly invasive MDA-MB-231. MCF-7 cells are non-motile, exhibit typical levels of glycolysis, and are non-invasive which closely matches the properties we have defined for the proliferating tumor cells. The MDA-MB-231 cells on the other hand exhibited Warburg-like glycolytic levels, were highly motile, and highly invasive as would be expected of the malignant cells defined here. In spheroid culture, the more aggressive MDA-MB-231 cells migrated to the outside of the spheroid, surrounding a core of MCF-7 cells within hours; this experiment will serve as justification for the greater transition rate of M_Q cells back to M_S cells as the malignant cells will have a tendency to move rapidly toward well-oxygenated regions where they can proliferate. Additionally, the cells were injected into mouse mammary fat pads and experiments were carried out in which the mice were either in the control case or received $NaHCO_3$ buffer therapy; mice who did not receive therapy posessed primarily aggressive MDA-

MB-231 while those who did receive the treatment showed significant increases in the ratio toward the less aggressive MCF-7 cells.

Section 1.5

Buffer Therapy and Prostate Cancer

Prostate cancer is one of the most common cancers in men and carries a particularly low survival rate upon metastasis – a mere 29.3% survival rate over five years.[10] Unfortunately, detection is particularly difficult because it is typically asymptomatic until the cancer is considerably advanced or has already metastasized; thus, many men undergo annual prostate specific antigen testing as a precautionary measure thereby permitting early intervention. Treatments are typically comprised of combination and low-dose therapies to prolong survival but not necessarily cure the cancer as the treatments are not perfectly effective and all carry considerable side effects – some of the currently available treatment options include surgery, radiotherapy hypofractionation, and proton beam therapy. Additionally, there are currently clinical trials exploring chemotherapy, hormonal therapy, cryosurgery, and high intensity focused ultrasound.[11]

There are currently several modes of studying prostate cancers including cultures of mouse and human cell lines of prostate cancer, xenotransplantation of human prostate cancer (such as the PC3 and LNCaP cell lines) in mice, and a transgenic mouse in which prostatic adenocarcinoma arises known as TRAMP mice. TRAMP mice are of particular interest as the cancer arises spontaneously and the cells undergo a series of mutations comparable to those in human men with prostatic adenocarcinoma thereby making this model uniquely suited to studying the cancer. Specifically,

the mice undergo a predictable series of events, developing the invasive cancer precursor prostatic epithelial neoplasia (PIN) by 12 weeks, well differentiated adenocarcinoma by 24 weeks, and metastasis by 30 weeks of age.[25, 26, 27] Additionally, the mice are found to die from the disease within 52 weeks but this can be prolonged through the administration of buffer therapy.[28] Some experiments employ the xenotransplantation of cancer cells harvested from the TRAMP prostate into the flank thereby enabling measurements of tumor volume and growth which would not otherwise be measurable as the cancer is spread throughout the prostate and not in one distinct tumor.

As described previously, solid tumors undergo the Warburg effect which is characterized by an increase in acid levels due to constitutive glycolysis even in the presence of adequate oxygen. Buffer therapy is a mode of cancer treatment which attempts to slow the growth of cancers and their progression toward malignancy through the administration of an alkaline substance. While this therapy has not yet been administered in humans, several studies in mouse have shown that individuals that have received alkaline water orally prior to the development of tumors showed significant delays in tumor progression both in prostate and breast cancer.[2] Other studies found complete elimination of malignant cells in TRAMP prostate cancers when buffer therapy was administered sufficiently early but essentially no response to therapy with late administration.[3, 28] Additionally, a hybrid cellular automata model of a metabolically heterogeneous tumor calibrated to TRAMP prostate growth showed a decline in malignancy with early buffer intervention but a selection for the most aggressive malignant cells when the therapy is administered late.[29]

Chapter 2

Model Development

A system of fifteen nonlinear ordinary differential equations has been generated to represent the transitions between compartments as presented in Figure 2.1. The variables of interest are listed below in Table 2.1 and the differential equations and their descriptions are presented in this chapter.

Table 2.1: Model Variables

Variable	Meaning
G_1	Proliferating Tumor Cells (G_1 Phase)
S	Proliferating Tumor Cells (S Phase)
G_2	Proliferating Tumor Cells (G_2 Phase)
Q	Quiescent Tumor Cells
N	Necrotic Cells
T	TNF-α
R	VEGF
V	Vasculature
A_H	Anaerobic/Glycolytic and Acid Resistant Cells
M_Q	Quiescent Malignant Cells
M_{G_1}	Malignant Cells (G_1 Phase)
M_S	Malignant Cells (S Phase)
M_{G_2}	Malignant Cells (G_2 Phase)
L_1	Acidification of the Hypoxic Region
L_2	Acidification of the Oxygenated Region

Table 2.1

Section 2.1

The Original Model

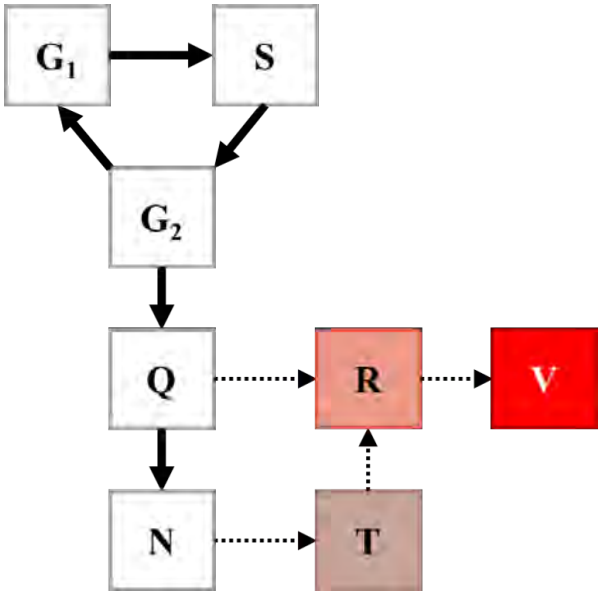

Figure 2.1: White boxes represent the various cancer cells: proliferative (G_1, S, and G_2), quiescent (Q), and necrotic (N). Solid arrows represent cell transitions. Dotted arrows reflect influence of one compartment on another such as the secretion of VEGF (R) by quiescent cells, secretion of TNF-α (T) by necrotic cells, and the development of vasculature (V) due to VEGF signaling.

Equations 1-8 as presented below were taken from Wallace et al. and He et al. and built upon;[32, 12] Figure 2.1 is a box visualization of these equations. The new terms from this thesis in the first eight equations have been marked by under-brackets and the descriptions of these new terms are highlighted in grey. Additional equations that have been incorporated into the model will be described later.

1. Proliferating Tumor Cells (G_1 Phase).

$$\frac{dG_1}{dt} = 2c_2G_2 - c_1(B)G_1 - c_1(1-B)G_1 - c_fFG_1 \underbrace{-D_2G_1}$$

$$= \text{cell division and transition to } G_1 \text{ phase} - \text{transition to S phase} - \text{quiescence}$$

$$- \text{apoptosis due to TNF-}\alpha - \text{death due to acid}$$

2. Proliferating Tumor Cells (S Phase).

$$\frac{dS}{dt} = c_1BG_1 - c_sS + CQ - c_fFS \underbrace{-D_2S}$$

$$= \text{transition to the S phase} - \text{transition to the } G_2 \text{ phase} + \text{return of cells from } Q$$

$$- \text{apoptosis due to TNF-}\alpha - \text{death due to acid}$$

3. Proliferating Tumor Cells (G_2 Phase).

$$\frac{dG_2}{dt} = c_sS - c_2G_2 - d_aG_2 - c_fFG_2 \underbrace{-D_2G_2}$$

$$= \text{transition to the } G_2 \text{ phase} - \text{cell division and transition to } G_1 \text{ phase}$$

$$- \text{natural cell apoptosis} - \text{apoptosis due to TNF-}\alpha - \text{death due to acid}$$

4. Quiescent Cells.

$$\frac{dQ}{dt} = c_1(1-B)G_1 - CQ - eHQ \underbrace{-D_1Q - a_hq_3Q}$$

$$= \text{transition of hypoxic cells from } G_1 - \text{return of cells to S} - \text{necrotic death of } Q$$

$$- \text{death due to acid} - \text{development of acid resistance}$$

5. Necrotic Cells.

$$\frac{dN}{dt} = eHQ + [D_2(G_1 + S + G_2) + D_1Q + D_3(A_H + M_Q) + D_4(M_{G1} + M_S + M_{G2})] - m(v_0 + V)N$$

$$= \text{necrotic death of } Q + \text{acid related death of proliferative, quiescent, acid resistant glycolytic, and acid resistant malignant cells} - \text{natural removal of dead matter}$$

6. TNF-α.

$$\frac{dT}{dt} = jN - k(v_0 + V)T$$

$$= \text{production of TNF-}\alpha \text{ from necrotic tissue} - \text{removal of } T \text{ by vasculature}$$

7. VEGF Production and Removal.

$$\frac{dR}{dt} = c_R(G_2 + S + G_1 + M_{G1} + M_S + M_{G2})\frac{T}{s_R + T} + c_{qv}(Q + A_H + M_Q) - q_R(v_0 + V)R$$

$$= \text{production of VEGF by proliferating and malignant cells in the presence of TNF-}\alpha + \text{production of VEGF by quiescent, acid resistant hypoxic, and quiescent malignant cells} - \text{natural removal of VEGF signal}$$

8. Development of Vasculature.

$$\frac{dV}{dt} = (1 - D_V)\, c_v \frac{R(v_0 + V)}{s_v + R + v_0 + V} - D_V V$$

$$= \text{acid mediated vasculature growth in the presence of VEGF signal} - \text{tissue death due to acid}$$

Section 2.2

Additions to the Model

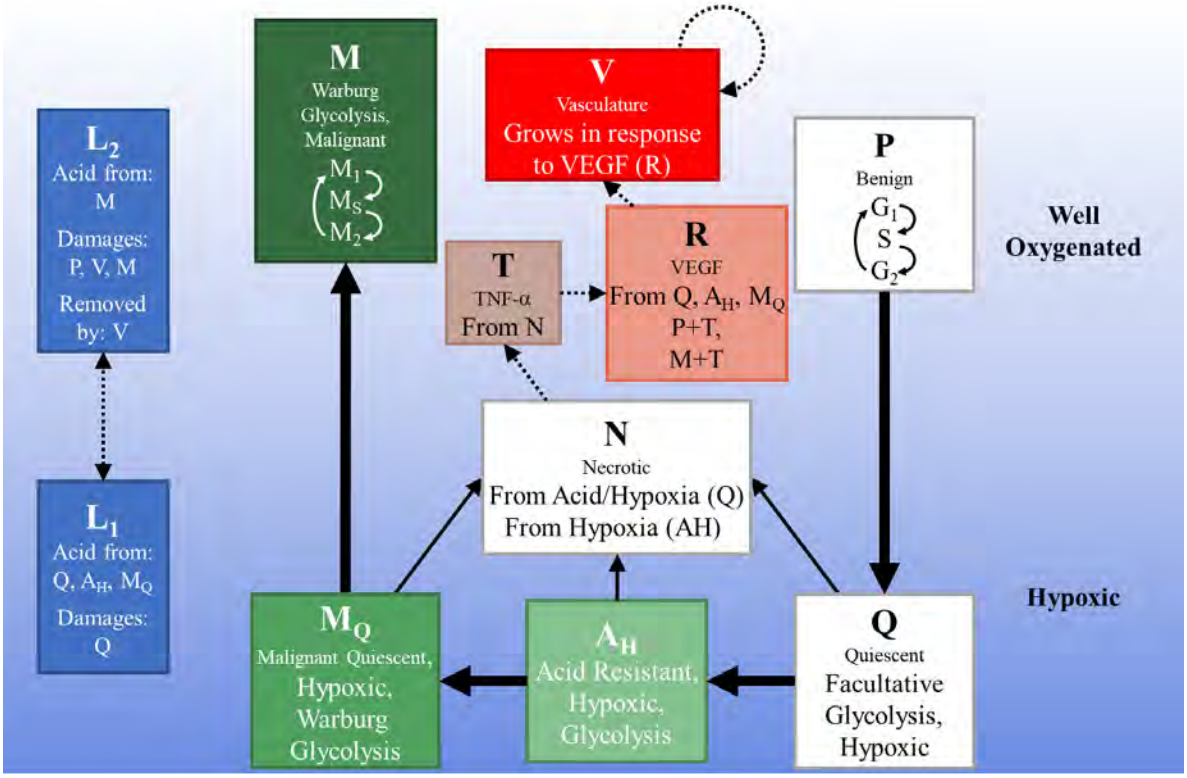

Figure 2.2: A representation of the structure of the model developed in this study. Transitions between cell compartments including cell necrosis are shown as solid black arrows and the basic progression to malignancy proposed is shown by the large black arrows. Additions to the model due to Wallace et al and extended by He et al are represented by the blue and green boxes. Although no specific geometry is assumed, all cells are allocated to either a well-oxygenated or hypoxic region, each with its own level of acidity.

To evaluate the impacts of acidosis on tumor development quantitatively, the mechanistic tumor model developed by Wallace et al. and extended in He et al., which includes compartments for proliferating, quiescent, and necrotic cells, VEGF and TNF-alpha signals, and growing vasculature is further developed.[32, 12] The

extended model includes the process by which the initial tumor growth produces a population of hypoxic cells which in turn engenders glycolysis. The resulting acid production is modeled explicitly in the hypoxic region and cell death depends on levels of acid in that region. In addition, the acid produced in the hypoxic region mediates the emergence of an acid resistant phenotype whose death rate also depends on the surrounding acidic environment but they are more tolerant to low pH. Continued exposure to acidity further mediates a transition to malignancy and then malignant aerobic glycolysis via the Warburg Effect at a low rate. The model conflates the appearance of a constitutively glycolytic, acid resistant phenotype with malignancy, assuming such cells will migrate to oxygen rich regions which they further acidify, modeled as a separate compartment with some diffusion between the hypoxic and normoxic acid compartments. Selection of rapidly proliferating cells in this model occurs due to differing tolerance for the increasingly acidic environment. The model includes the growth of vasculature, which has multiple roles: delivering nutrients and oxygen, removing necrotic material, VEGF signals, TNF-alpha, and acid. A schematic diagram of the resulting model is shown in Figure 2.2 and the new equations are described as follows.

9. Anaerobic/Glycolytic Acid Resistant Cells.

$$\frac{dA_H}{dt} = a_h q_3 Q + c_{ga} A_H - m_h A_H - D_3 A_H$$

$$= \text{conversion from quiescent to acid resistant} + \text{cell division} - \text{acquisition of malignancy}$$

$$- \text{death due to acid exposure in the hypoxic region}$$

10. Malignant Cells (G_1 Phase).

$$\frac{dM_{G1}}{dt} = 2k_2M_{G2} - k_1(B_M)M_{G1} - k_1(1-B_M)M_{G1} - k_fFM_{G1} - D_4M_{G1}$$

$$= \text{cell division and transition to G1 phase} - \text{transition to S phase} - \text{quiescence}$$

$$- \text{apoptosis due to TNF-}\alpha - \text{death due to acid in oxygenated region}$$

11. Malignant Cells (S Phase).

$$\frac{dM_S}{dt} = k_1B_MM_{G1} - k_sM_S + C_MM_Q - k_fFM_S - D_4M_S$$

$$= \text{transition to the S phase} - \text{vasculature dependent transition to the } G_2 \text{ phase}$$

$$+ \text{return of cells from } M_Q - \text{apoptosis due to TNF-}\alpha$$

$$- \text{death due to acid in oxygenated region}$$

12. Malignant Cells (G_2 Phase).

$$\frac{dM_{G2}}{dt} = k_sM_S - k_2M_{G2} - d_aM_{G2} - k_fFM_{G2} - D_4M_{G2}$$

$$= \text{transition to the } G_2 \text{ phase} - \text{cell division and transition to } G_1 \text{ phase} - \text{natural apoptosis}$$

$$- \text{apoptosis due to TNF-}\alpha - \text{death due to acid in oxygenated region}$$

13. Quiescent Malignant Cells.

$$\frac{dM_Q}{dt} = m_HA_H + k_1(1-B_M)M_{G1} - C_MM_Q - D_3M_Q$$

$$= \text{development of malignancy from } A_H + \text{transition of hypoxic cells from } G_1$$

$$- \text{return of cells to } M_S - \text{death due to acid}$$

14. Acidification of the Hypoxic Region.

$$\frac{dL_1}{dt} = x_h(Q + A_H + M_Q) - l(L_1 - L_2) - s_b q_1 L_1 H(t - \tau)$$

$$= \text{input of acid from acid resistant hypoxic cells and glycolytic cells}$$

$$\text{in hypoxic region} - \text{diffusion of acid} - \text{removal of acid treatment at time } \tau$$

15. Acidification of the Oxygenated Region.

$$\frac{dL_2}{dt} = x_m(M_{G1} + M_S + M_{G2}) - l(L_2 - L_1) + q(3.9810717 \times 10^{-14} - L_2)(V + v_1) - s_b q_2 L_2 H(t - \tau)$$

$$= \text{input of acid from each of the three phases of malignant cells} - \text{diffusion of acid}$$

$$- \text{restoration of normal pH} - \text{removal of acid treatment at time } \tau$$

In these equations, it is assumed first that the dynamics of the malignant cells are essentially the same as the normal proliferative cells in that they become quiescent under hypoxic conditions and they are modeled in three cell cycle stages. They differ however in their response to acidosis; the proliferative cells can withstand a pH as low as 6.3 while the malignant cells are able to withstand a pH as low as 6.0. Additionally, because malignant cells are assumed here to have acquired motility, they will be parametrized to return to proliferation from the quiescent compartment at a different rate than the non-malignant proliferative cells such that there is a new functional parameter. C_M.

2.2.1. Functional Parameter Descriptions

Equations for not-yet-defined variables in the above system include a series of rate-bounded transitions characterized as functional responses, expressions for the pH corresponding to a region, as well as a few notational shortcuts.

(a) $B = \frac{v_0+V}{s_1+G_1+v_0+V}$

= availability of nutrients relative to the volume of cells in G_1

(b) $C = c_q \frac{v_0+c_{qs}V}{s_q+P+v_0+c_{qs}V}$

= available nutrients as a fraction of the quiescent cells that become proliferative

(c) $B_M = \frac{v_0+V}{s_1+M_{G1}+v_0+V}$

= availability of nutrients relative to the volume of cells in M_{G1}

(d) $C_M = c_{qm} \frac{v_0+c_{qs}V}{s_q+M+v_0+c_{qs}V}$

= available nutrients as a fraction of the malignant quiescent cells that become proliferative (malignant)

(e) $H = 1 - \frac{V}{s_h+f_hP+g_hQ+V}$

= describes the transition of quiescent cells to necrotic

(f) $F = \frac{T}{s_n+T}$

= a rate based on TNF-α production which controls apoptosis

(g) $P = G_1 + S + G_2$

= total proliferating cells = G_1 phase + S phase + G_2 phase cells

(h) $M = M_{G1} + M_S + M_{G2}$

= total proliferative malignant cells = G_1 phase + S phase + G_2 phase cells

(i) $pH_1 = -\log(L_1 \times 10^6)$

= pH of hypoxic region

(j) $pH_2 = -\log(L_2 \times 10^6)$

$= pH$ of oxygenated region

The next three parameters control the response of various compartments under acidifying conditions. q_1 and q_2 relate to the clearance of acid during the application of buffer therapy. Because the bicarbonate solution used in TRAMP mouse experiments has a pH of about 8.5 [37], the therapy is only permitted to increase the pH of each acid compartment until it has attained the same pH as the therapy; above the therapy pH, these two parameters are set to zero and thus the therapy ceases to have an effect. The q_3 parameter works similarly and only permits the acquisition of acid resistance below a pH slightly below 7.2 which is the lower limit for a healthy physiological pH.[34, 36]

(k) $q_1 = -min(0, (pH_1 - 8.5))$

$=$ control of the pH increase of the hypoxic region to buffer therapy

(l) $q_2 = -min(0, (pH_2 - 8.5))$

$=$ control of the pH increase of the normoxic region to buffer therapy

(m) $q_3 = -min(0, (pH_1 - 7.185))$

$=$ acid mediated transition to acid resistant

The following four parameters represent the acid related death of various cell types. Here, the acidity of interest is local environmental pH instead of blood pH (7.35 - 7.45 but taken here to just be the average, 7.4) because a person

cannot survive with pH 7 and a pH of 7.2 is considered extremely acidotic. Cells, however can survive to pH as low as 6.3 for normal tissue and as low as 6 for acid resistant cells.[1, 35] As such, functions are established such that non-malignant cells have no response when the pH is above the lower bound for healthy tissue which is 7.2 and increasing in their death probability on a sine curve to 1 for the threshold pH for death. Malignant cells only begin to die from acid exposure at a pH of 7.185 which is taken here to be the pH at which a transition to acid resistance takes place. Finally, the vascular recruitment is allowed to proceed as usual at pH 7.4 and responsiveness to VEGF ceases altogether at pH 6.4 as per the research of Faes et al.[19]

(n) Acid-related death of tumor cells in the hypoxic region (Q)

$$D_1 = \begin{cases} 1 & pH_1 \leq 6.3 \\ 0.5 \cdot \sin\left(\dfrac{pH_1 \cdot \pi}{0.9} + 4.712\right) + 0.5 & 6.3 < pH_1 < 7.2 \\ 0 & pH_1 \geq 7.2 \end{cases}$$

(o) Acid-related death of tumor cells in the oxygenated region (G_1, S, G_2)

$$D_2 = \begin{cases} 1 & pH_2 \leq 6.3 \\ 0.5 \cdot \sin\left(\dfrac{pH_2 \cdot \pi}{0.9} + 4.712\right) + 0.5 & 6.3 < pH_2 < 7.2 \\ 0 & pH_2 \geq 7.2 \end{cases}$$

(p) Acid-related death of malignant cells in the hypoxic region (A_H,M_Q)

$$D_3 = \begin{cases} 1 & pH_1 \leq 6 \\ 0.5 \cdot \sin\left(\dfrac{pH_1 \cdot \pi}{1.185} + 4.51313\right) + 0.5 & 6 < pH_1 < 7.185 \\ 0 & pH_1 \geq 7.185 \end{cases}$$

(q) Acid-related death of malignant cells in the oxygenated region (M_{G1}, M_S, M_{G2})

$$D_4 = \begin{cases} 1 & pH_2 \leq 6 \\ 0.5 \cdot \sin\left(\dfrac{pH_2 \cdot \pi}{1.185} + 4.51313\right) + 0.5 & 6 < pH_2 < 7.185 \\ 0 & pH_2 \geq 7.185 \end{cases}$$

(r) Acid-related death of endothelial cells (V)

$$D_V = \begin{cases} 1 & pH_2 \leq 6.4 \\ 0.5 \cdot \sin\left(pH_2 \cdot \pi + 0.31378\right) + 0.5 & 6.4 < pH_2 < 7.4 \\ 0 & pH_2 \geq 7.4 \end{cases}$$

Chapter 3

Parameter Development

The model was parametrized first as a monolayer for which data for the cell cycle was utilized; next as a spheroid for which data about proliferation, quiescence, and necrosis was available; finally, *in vivo* experimental data was used to parametrize tumor growth in a mouse model. By establishing parameters sequentially, behavior at the cellular, tumor, and body levels is captured in a way that would be impossible if the model was simply parametrized to *in vivo* data.

Section 3.1

Monolayer Experimental Parameters, c_1, c_s, c_2, d_a

To parametrize the monolayer, the equations to calculate the parameters c_1, c_s, c_2 from He et al. as described in chapter 1 were utilized. This thesis is concerned with modelling tumor growth in TRAMP mice, so TRAMP monolayer cell cycle data from Ghosh et al. was utilized in computing the three cell cycle parameters. The results from Ghosh et al. show a doubling time of 0.833333 days, 59.55 percent of the cells were in G1 phase, 28.83 percent of the cells were in S phase, and 11.63 percent of

the cells were in G2 phase for TRAMP prostate cancer cells in culture [31]. Thus, the parameters $c1$, cs, and $c2$ can be found in Table 3.1 and the growth curves are plotted below in Figure 3.1.

Plugging the values for doubling time and percentage of cells in each phase into the equations from He et al., the parameter values were calculated to be the following:

$$c_1 = \frac{(\lambda + d_a G_2^*)}{G_2^*} = 1.961763658\ day^{-1}$$
$$c_s = \frac{(2c_2 G_2^* - \lambda G_1^*)}{G_1^*} = 3.220357473\ day^{-1}$$
$$c_2 = \frac{(c_1 G_1^* - \lambda S^*)}{S^*} = 7.151991545\ day^{-1}$$

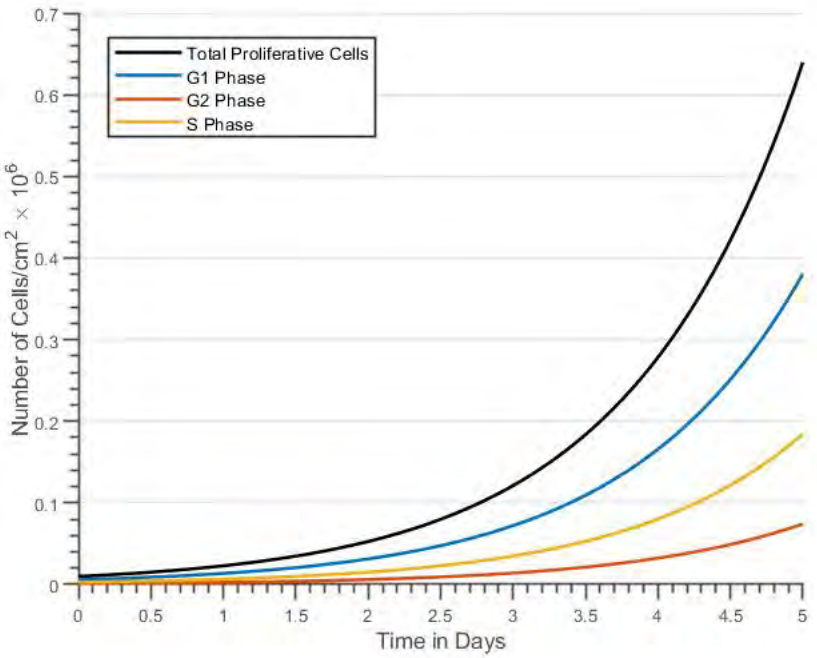

Figure 3.1: Plot of the change in monolayer cell population and the populations of each cell cycle phase over time using the parameters obtained from Ghosh et al.

Section 3.2

Spheroid Experimental Parameters

3.2.1. Spheroid Parameters, $v_0, j, k, s_1, s_q, e, s_n, c_q, c_f$

The data for the spheroid tumor growth was less directly available but was possible to compute from a paper on prostate cancer spheroid growth from 1999 by Ballangrud et al. The paper made use of measurements of spheroid volume, prostate specific antigen (PSA) secretion, and (BrdUrd) staining in the LNCaP-FGC human prostatic cancer cell line. The cell line is designated FGC or "fast growing clone" and is commonly used in mouse xenografts; it is assumed here that the growth dynamics of the fast growing LNCaP cells more closely match those of TRAMP cells and as such the data will be used in the spheroid fit.

Ballangrud et al. recorded spheroid volume data for 24 LNCaP spheroids and plotted them; the MATLAB function GRABIT was utilized to pull data from the paper's figures. The values for volume and day are included in the second appendix in Table A2-1 as well as the conversion from volume to radius. These radii were plotted against time to generate Figure 3.2 and a linear regression was used to find the days at which the spheroid had radius $200\mu m$ and $300\mu m$ which correspond to the sizes at which measurements of quiescent and necrotic cells were obtained.

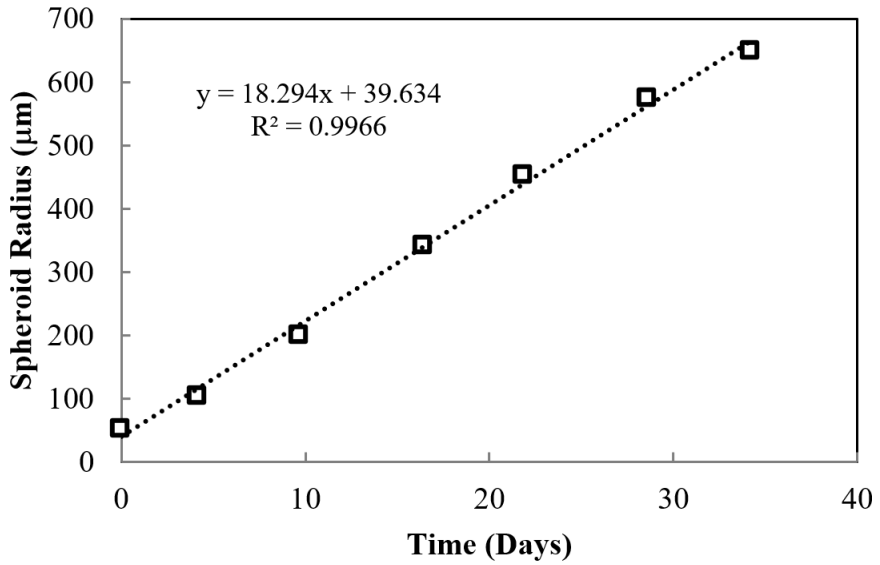

Figure 3.2: Linear fit of the data pulled from Balangrud et al. as observed in Appendix II, Table A2-1

Next, several conversions between cross sectional area in the spheroid (as recorded in the data by Ballangrud et al.), radius, and volume had to take place. A visualization of a spheroid in cross section is provided below in Figure 3.3.

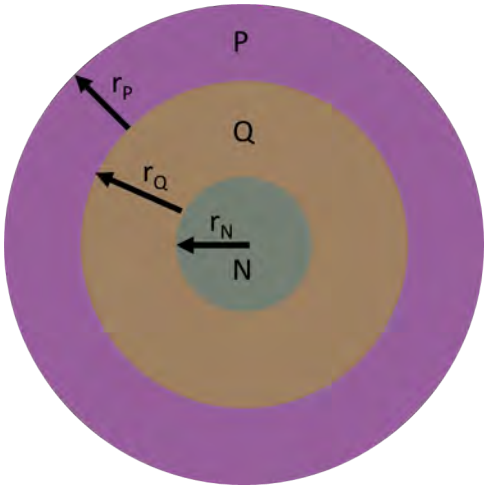

Figure 3.3

The necrotic radii were determined by subtracting the radius of the viable region

from the total radius of each spheroid. Only about 50% of the viable cells stained for BrdUrd which means that only half were proliferating; this is taken to indicate that half of the cross sectional area of cells in the viable region are proliferative and the other half are quiescent because the cell counts were taken in slices of the spheroid.[30] Thus, the viable area (A_v), necrotic radius (r_N) and the following computations are used to determine the radii of the proliferative (r_P) and quiescent (r_Q) compartments:

$$r_Q = \sqrt{\frac{A_v}{2\pi} + r_N^2} - r_N$$
$$r_P = \sqrt{\frac{A_v}{\pi} + r_N^2} - r_Q - r_N$$

The values determined from this calculation are listed in Appendix II Table A2-2. The radii for the proliferative, quiescent, and necrotic regions were converted to volumes under the assumption that the spheroid is a perfect sphere and that it is comprised of perfect layers of quiescent and then proliferative cells surrounding a necrotic core as illustrated in Figure 1.2. The equations for the three compartment volumes are below:

$$vol_N = \frac{4}{3}\pi(r_N)^3$$
$$vol_Q = \frac{4}{3}\pi(r_Q + r_N)^3 - vol_N$$
$$vol_P = \frac{4}{3}\pi(r_P + r_Q + r_N)^3 - vol_Q - vol_N$$

Parameter Selection. The parameters $v_0, j, k, s_1, s_q, e, s_n, c_q, c_f$ were tuned to get the best fit of the data for the volumes of the whole spheroid and the proliferative, quiescent, and necrotic compartments by hand. The fit was then refined using the custom genetic algorithm described in Chapter 7, which minimizes the relative mean

squared error between the curves output by the model and the data points. The parameters associated with this fit and a description of their roles can be seen in Table 3.1 and the figures associated with this fit can be seen in Appendix I.

3.2.2. Acidosis Parameters, $a_h, k_1, k_s, m_h, k_f, k_2, x_h, l, x_m, q, c_{ga}$

To incorporate acid into the model, the data from Ballangrud et al. used previously is again utilized at the same time as data for the pH of each spheroid compartment to develop a parametrization for the spheroid with acidosis and malignancy. Additionally, data from several sources are utilized to develop the acidic conditions below which each cell type cannot survive. The parameters determined here will be maintained in the parametrization for the complete model.

The data for extracellular pH of spheroids measured by the depth from the surface of the spheroid was limited and it was not possible to find such data for prostate cancer spheroids; thus, an assumption is made that spheroids of any cell type will have a comparable pH gradient when cultured under identical conditions. A study by Alvares-Pérez et al. measured pH in spheroids cultured in the same media as those in Ballangrud ed at., and developed from the C6 and H35 cell lines which are rat glioma and hepatoma cell lines respectively. They measured pH at a resolution of 0.1 pH unit and determined iso-pH shells in the spheroids based on probe depth.

As described in the previous section, there is data for the radii of each of the layers of the spheroid at model days 8.766 and 14.23. The proliferative compartment had radius $33.6\mu m$ and $35.3\mu m$ and the quiescent compartment had radius $42.4\mu m$ and $40.7\mu m$ on the two days. Because the radii essentially did not change over the five day period, it is assumed that the compartments have reached their terminal thicknesses at this size although their volumes will continue to increase as the necrotic

compartment grows. The pH of each compartment is taken as the pH at the half way point between the compartment boundaries as shown in Figure 3.4 The proliferative region thus falls within the iso-pH region from Alvares-Pérez et al. for pH 7.1 and the quiescent compartment is in the iso-pH region for pH 7.0. Thus, these are taken to be the pH to which the spheroid compartments P and Q will equilibrate.

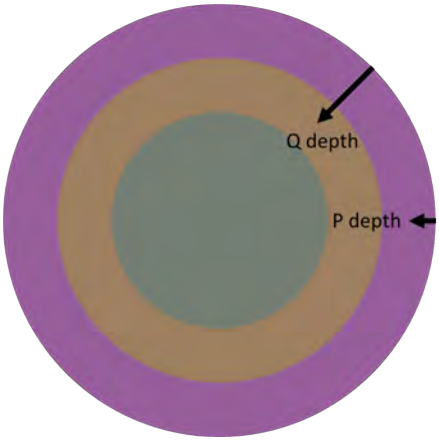

Figure 3.4: A representation of the depths corresponding to the centers of the quiescent and proliferative regions in a prostate cancer spheroid. These depths were matched to data for pH organized by probe depth in rat glioma and hepatoma.

Anderson et al. provides data concerning the probability of death of the various cell types as a result of acid exposure. While this study was carried out in tumors comprised of HeLa cells which are not directly pertinent to this study, interesting results about the pH tolerance of highly metastatic vs non metastatic tumor cells emerged. Inside non-metastatic tumors, the external pH at the cell surface was found to be 6.7-6.9 but inside highly metastatic tumors the cell surface pH was 6.1-6.4. Additionally, they found that the average pH was 7.4 without tumors producing acid by glycolysis which matches physiological pH and provides an initial condition for both L1 and L2. Thus, it is tentatively assumed that this pH indicates that the lethal levels of pH for non-acid-adapted cancer cells are somewhere in the range of

6.4-6.7 thereby providing a threshold at which a percentage of non-resistant cells will die off. Recall the general equation for death due to acid exposure for all cell types:

$$D = \begin{cases} 0 & pH \leq pH_{death} \\ 0.5 \cdot \sin\left(\dfrac{pH \cdot \pi}{(pH_{physio} - pH_{death})} + n\right) + 0.5 & pH_{death} < pH < pH_{physio} \\ 1 & pH_2 \geq pH_{physio} \end{cases}$$

where pH_{death} is the pH below which cells of a given type cannot survive, pH_{physio} is a healthy blood pH, and n which is a numeric factor that guarantees that the curve begins at zero and ends at one within the range of pH_{death} and pH_{physio}. Because there is evidence that malignant cells survive in a pH of 6.1, further substantiated by a study on PC3-M and PNEC cells which are human prostate cancer cell lines which found that few to no cells survive below a pH of 6.0, the pH_{death} for malignant cells was set to 6.0.[1, 35] Additionally, because the less malignant spheroids typically maintained a pH 0.3 greater than the highly metastatic spheroids and because there was evidence that the centers of these spheroids attained pH 6.4, the pH_{death} for cells that have not acquired acid resistance is set to 6.3.

Normal tissue pH can be as low as 7.2 so this was taken to be the value for pH_{physio} for the non-acid resistant cells.[34, 36] In order for cells to become acid resistant in this model, the pH of the hypoxic compartment must sink below the low bound for physiological pH, 7.2 and thus a somewhat lower pH value of 7.185 is set both for the threshold at which cells begin to turn acid resistant and for the pH_{physio} of the malignant cells.

Parameter Selection. A hand fit was carried out first and the parameters were then refined with the genetic algorithm described in Chapter 7. The parameters corresponded to the best fit for the whole tumor volume, quiescent, proliferative, and necrotic compartment volumes, and acid accumulation in the two spheroid regions were determined.[30, 33] The parameters associated with this fit can be found with an explanation of their roles in Table 3.1. A plot of three graphs is presented below in Figure 3.5 where Panel A corresponds to a fit to equilibrium pH values from Alvarez-Pérez et al., Panel B corresponds to a fit of the compartment volumes during the earlier time points of the simulation, and Panel C shows a fit to whole spheroid volume over the full simulation; spheroid volumes are those obtained from Ballangrud et al.

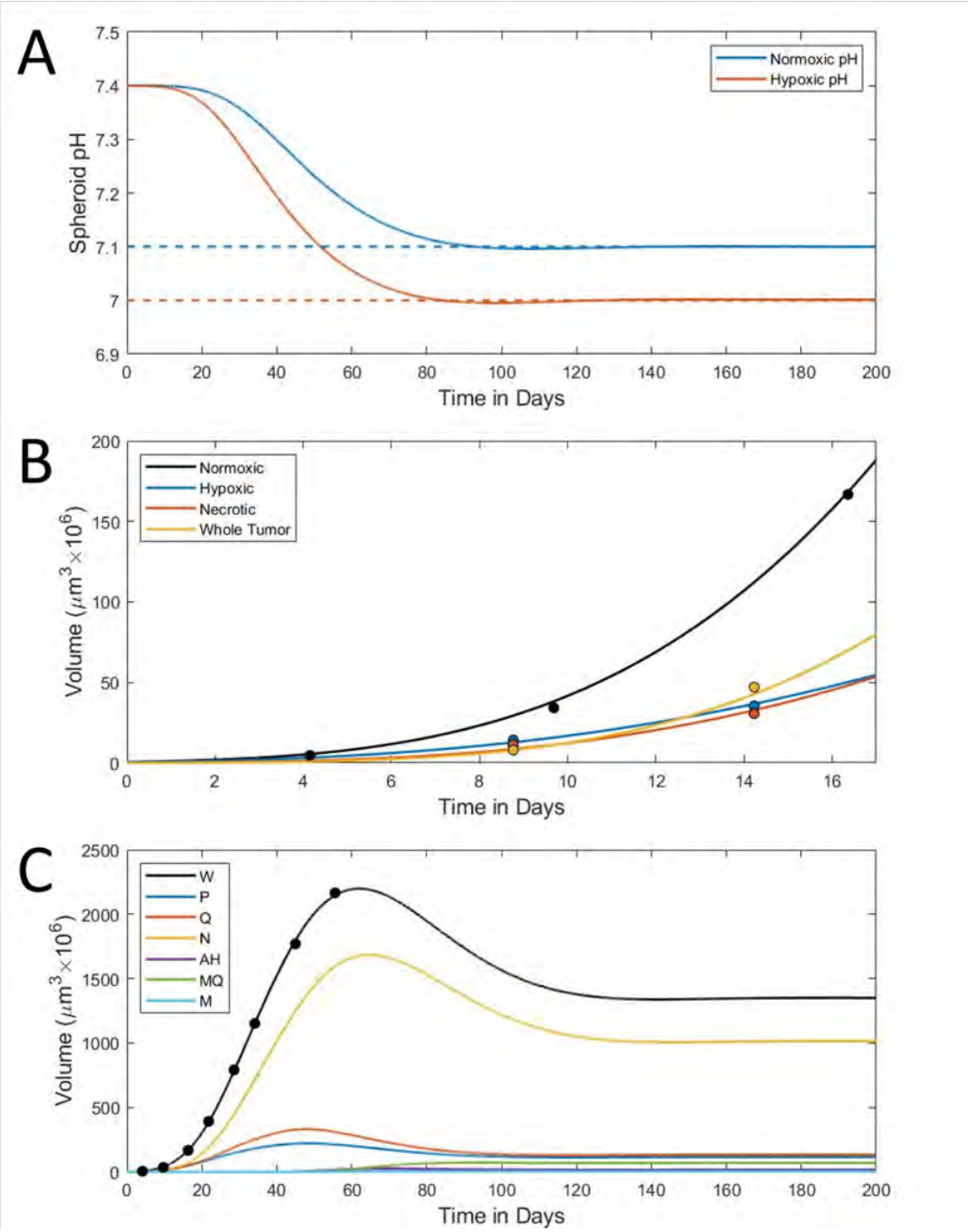

Figure 3.5: The best fit for the spheroid with acidosis. Panel A shows the change in pH of both the normoxic (P, M) and hypoxic (Q, A_H, M_Q) compartments over a window of 200 days where the dotted lines represent the equilibrium value for acid accumulation in each of the compartments as determined from the work of Alvarez-Pérez et al.[33] Panel B is zoomed in for the first 17 days and shows the fit of the data from Ballangrud et al. for the various spheroid compartments.[30] Panel C is the same as B but it shows both a fit of the whole tumor data from Ballangrud et al. and the long-term behavior of the model over the full 200 day period.[30]

Section 3.3

In Vivo Experimental Parameters,

$$v_0, c_v, c_R, s_R, q_R, c_{qv}, c_{qs}, s_v, s_h, f_h, g_h, q$$

A study by Astigiano et al. from 2016 involved the xenotransplantation of 6×10^6 TRAMP C1 cells into the flank of 6 week old male mice. Because the cells were injected subcutaneously, they were able to form essentially spherical tumors, the size of which is considerably easier to quantify than TRAMP prostate cancer *in situ*, which is irregular and has origins in many locations. Measurements of tumor volume were acquired for 10, 12, 14, 17, 19, 21, and 24 days post-injection. As in the spheroid, it is assumed that while the curve for volume is nonlinear, the plot of changing radius over time can be modelled with a linear regression thereby allowing for the determination of an initial volume when the cells were first injected. Additionally, this paper contains data for a treatment with alkaline water which will become relevant later for parametrizing buffer treatment during the experimental phase of this thesis. To determine the initial tumor volume for input in the model, tumor radius for each day was computed from the corresponding tumor volume under the assumption that the tumors were perfect spheres. A linear regression of the tumor radii to the day post-injection was determined in excel, the plot of which is below in Figure 3.6.

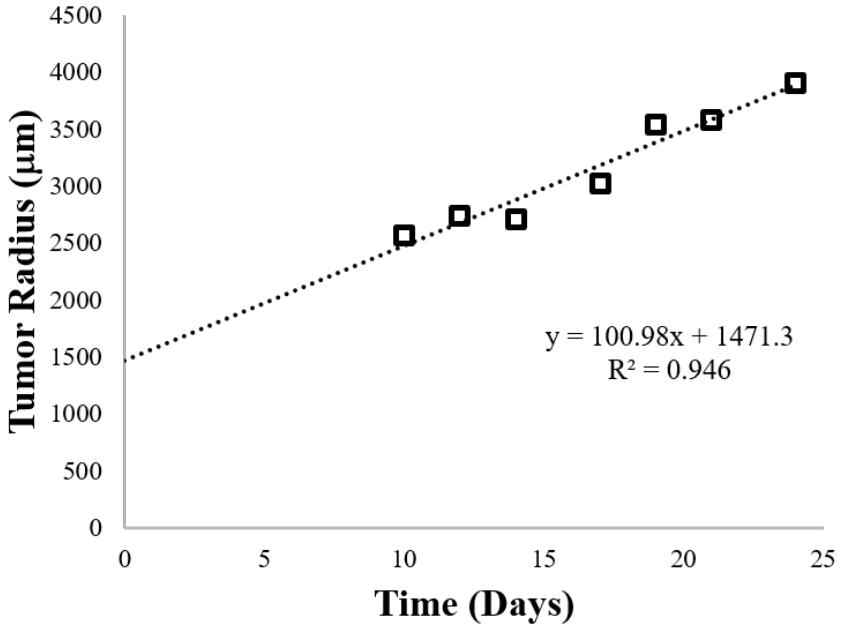

Figure 3.6: Linear fit of the data pulled from Astigiano et al. as observed in Appendix II, Table A2-3

From Figure 3.6, the linear regression has an R^2 value of 0.946 and there is an initial radius of $1471.3\mu m$. It was important to determine the initial radius and thus volume of the tumors because the cells were injected into the flank after being cultured essentially as a monolayer. It is thus assumed that all of the injected cells were proliferative, so the initial conditions for quiescent and necrotic cells were set to zero. Additionally, it was assumed that some of the cells were exposed to vasculature at the site of injection as the original tissue also required oxygen, so the initial condition for vasculature was set to 1.5% of the initial volume. A hand fit of the data was determined, after which the genetic algorithm was applied with 400 individuals and 300 generations as described in Chapter 7. The results of the fit can be found in Appendix I, Figure 7.1 and the parameters are in Table A1-1.

In Vivo Acidosis. Data from two papers by Ibrahim-Hashim et al. included data for the pH of a TRAMP prostate in mice that were 24 weeks and 52 weeks of age.[3, 28] Because they found that the TRAMP mice developed *in situ* prostate tumors and PIN by four weeks of age, it was assumed that day zero for the model corresponds to four weeks of age. The studies recorded a pH value of 6.7 for the prostate of 24 week-old TRAMP mice and 6.4 for 52 week-old mice; these two pH values thus correspond to days 140 and 336 in the model. These data points were used in fitting the hypoxic acid compartment because the vasculature in the normoxic compartment will rapidly clear acid from the environment of these cells.

Only four parameters were manipulated from the initial *in vivo* and acidic spheroid to generate a fit of the data from Astigiano et al. and Ibrahim-Hashim et al.: q which controls the rate at which vasculature clears acid had to decrease somewhat, l which is the rate of acid exchange between the normoxic and hypoxic compartments increased because there are no longer discreet shells in the tumor, c_{qv} had to increase to signal for additional vasculature, and v_1 is a new parameter which governs acid clearance into the tissue (without vasculature). The parameter values can be seen in Table 3.1. Plots of the best fit are seen below in Figure 3.7 in which Panel A shows a fit to the pH values obtained from the two papers by Ibrahim-Hashim et al., Panel B shows the fit to the whole tumor data by Astigiano et al., and Panel C shows the long-term behavior of the model including a linear growth phase of the whole tumor at later time points.

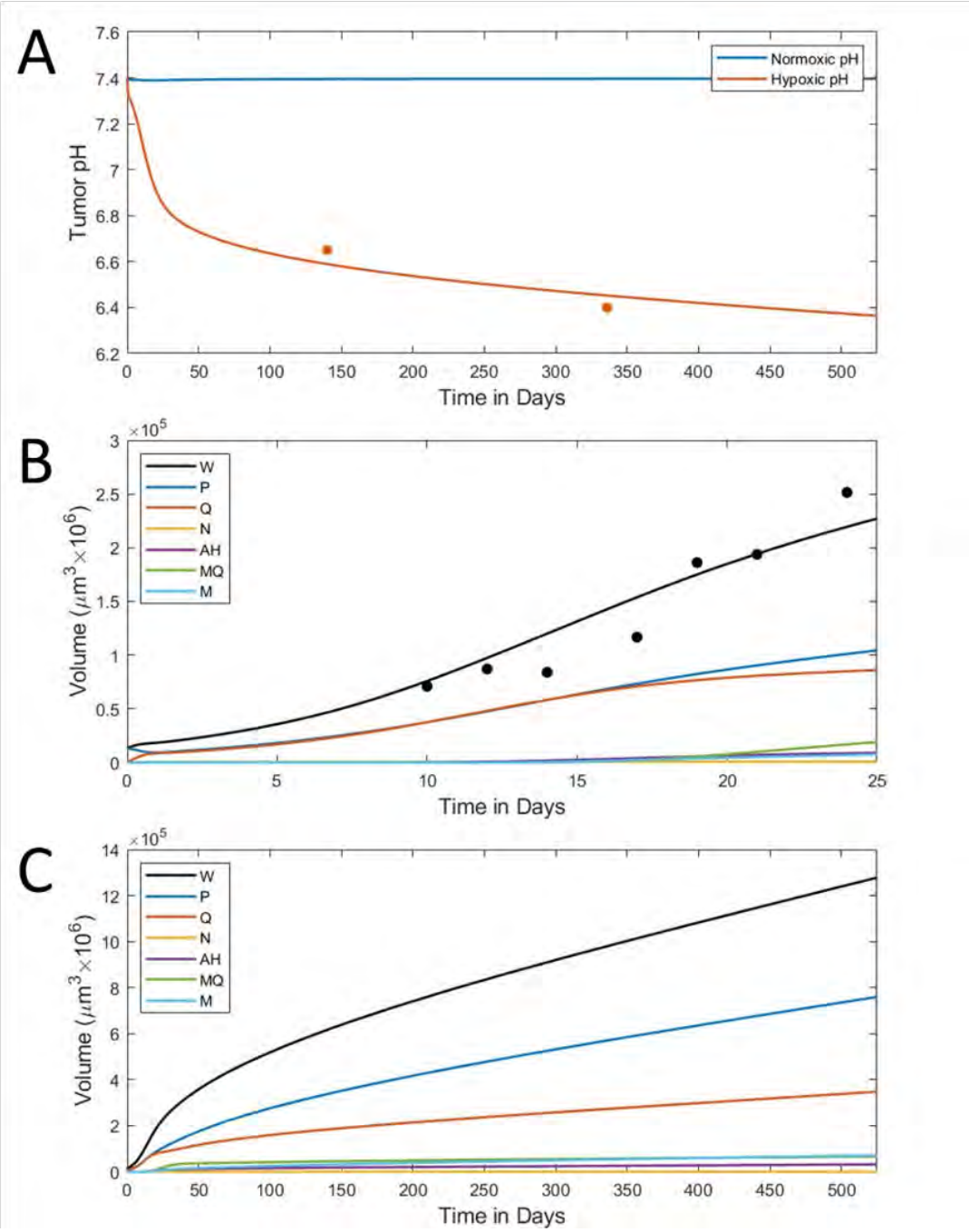

Figure 3.7: Panel A shows the pH of the normoxic compartments (P and M in blue and that of the hypoxic compartments (Q, A_H, and M_Q) in red; datapoints to which the modeled hypoxic pH was matched from Ibrahim-Hashim et al. are shown as red circles in this panel.[3, 28] Panel B shows the short-term behavior of the model over a 25 day period which is the time period over which Astigiano et al. collected data; datapoints for whole tumor volume are shown as black circles to which the black curve was matched.[2] Panel C shows the long-term behavior of the model.

Table 3.1: Model Parameters

	Monolayer	Spheroid	Spheroid Acid	Full Model	Description
d_a	0	0	0	0	Natural Death Rate
c_1	1.961763658	1.961763658	1.961763658	1.961763658	G_1 to S Transition
c_s	3.220357473	3.220357473	3.220357473	3.220357473	S to G_2 Transition
c_2	7.151991545	7.151991545	7.151991545	7.151991545	G_2 to G_1 Transition
v_0	–	2.798	2.798	14.86	Available Nutrients
j	–	0.543	0.543	0.543	TNF-α Production
k	–	0.0005	0.0005	0.0005	TNF-α Removal
s_1	–	1.601	1.601	1.601	B Half-Saturation Constant
c_q	–	76.2	76.2	76.2	C Maximum Rate
s_q	–	259	259	259	C Half-Saturation Constant
e	–	0.427	0.427	0.427	Q Necrotic Death
m	–	0.0284	0.0284	0.0284	Removal of Necrosis
s_n	–	534	534	534	F Half-Saturation Constant
c_f	–	0.01	0.01	0.01	TNF-α Induced Death (P)
k_1	–	–	1.961763658	1.961763658	M_{G1} to M_S Transition
k_s	–	–	3.220357473	3.220357473	M_S to M_{G2} Transition
k_2	–	–	7.151991545	7.151991545	M_{G2} to M_{G1} Transition
k_f	–	–	0.01	0.01	TNF-α Induced Death (M)
m_h	–	–	0.1	0.1	Acquisition of Malignancy
a_h	–	–	0.1	0.1	Acid Resistance
x_h	–	–	8.8×10^{-18}	8.8×10^{-18}	Hypoxic Acid Production
l	–	–	0.094	10	Intratumoral Acid Diffusion
x_m	–	–	8×10^{-18}	8×10^{-18}	Normoxic Acid Production
q	–	–	0.049	0.4	Acid Removal by Environment
c_{ga}	–	–	5.7×10^{-5}	5.7×10^{-5}	Acid Resistant Proliferation
c_{qm}	–	–	0.8	0.8	C_M Maximum Rate
c_R	–	–	–	6	VEGF Production by P, M
s_R	–	–	–	5000	VEGF Stimulation by TNF-α
c_{qv}	–	–	–	85	VEGF Production by Q, M_Q, A_H
q_R	–	–	–	17.935	VEGF Removal
c_v	–	–	–	0.8619	Angiogenesis
s_v	–	–	–	343.17	Describes Vasculature
c_{qs}	–	–	–	0.3733	Describes C
s_h	–	–	–	100	H Half-Saturation Constant
f_h	–	–	–	1.256	Describes H
g_h	–	–	–	0.01	Describes H
v_1	–	–	–	10	Tissue Clearance of Acid

Table 3.1: Grey highlights indicate that a spheroid parameter was changed *in vivo*

Chapter 4

Results

Section 4.1

Buffer Therapy

In a study by Ibrahim-Hashim et al., TRAMP mice were administered $200mM$ sodium bicarbonate buffer therapy in their drinking water beginning at four and ten weeks of age resulting in two outcomes – a complete regression of the malignant cells in mice that received early intervention and essentially no response in those that were treated late.[3] Ibrahim-Hashim et al. found that at four weeks of age the TRAMP mice had tumors confined to the ducts, either *in situ* or as PIN lesions and this was thus set as the first time of buffer therapy administration.[28] Thus, day zero in the model is taken to be four weeks of age in the mice and day 42 (or six weeks into the model) is taken to be mice at ten weeks of age.

The parametrized model was adapted to simulate the administration of buffer

therapy through the subtraction of a term of the form

$$s_b \cdot q_n \cdot L_n \cdot HS(t - \tau)$$

from each of the differential equations corresponding to the acid compartments, L_1 and L_2 or equations 14 and 15 in Chapter 2 of the thesis. Here, the subscript n is either 1 or 2 where 1 corresponds to the hypoxic compartment and 2 corresponds to the normoxic compartment.

A 2012 study by Ibrahim-Hashim et al. found that the pH of the prostate in mice that received early buffer therapy was roughly pH 7.7 at the time of sacrifice. Thus, the buffer therapy parameter, s_b was selected to be equal to 7000 so the pH of the hypoxic compartment was about 7.7 at day 336 which corresponds to week 52 in the experiments.[3] The parameter q_n is defined as the negative of the minimum between zero and the difference between the compartment pH and 8.5; sodium bicarbonate in 0.1 molar aqueous solution has pH 8.3 and the pH of saturated solution ranges between 8 and 9, so the pH of the 0.2 molar aqueous solution used in the experiments was taken to be 8.5.[37] The q_n parameter thus allows the pH of the compartments to increase at most to the pH of the buffer administered but stops the treatment from elevating the pH above that of the buffer. Finally, the term is multiplied by a heaviside function in MATLAB therefore allowing the time at which treatment is first administered to be controlled - this time is represented by τ and is set to 0 (four weeks of age) and 42 (10 weeks of age) for the early and late treatments.

The results of the early and late buffer treatments are shown below in Figure 4.1 and Figure 4.2.

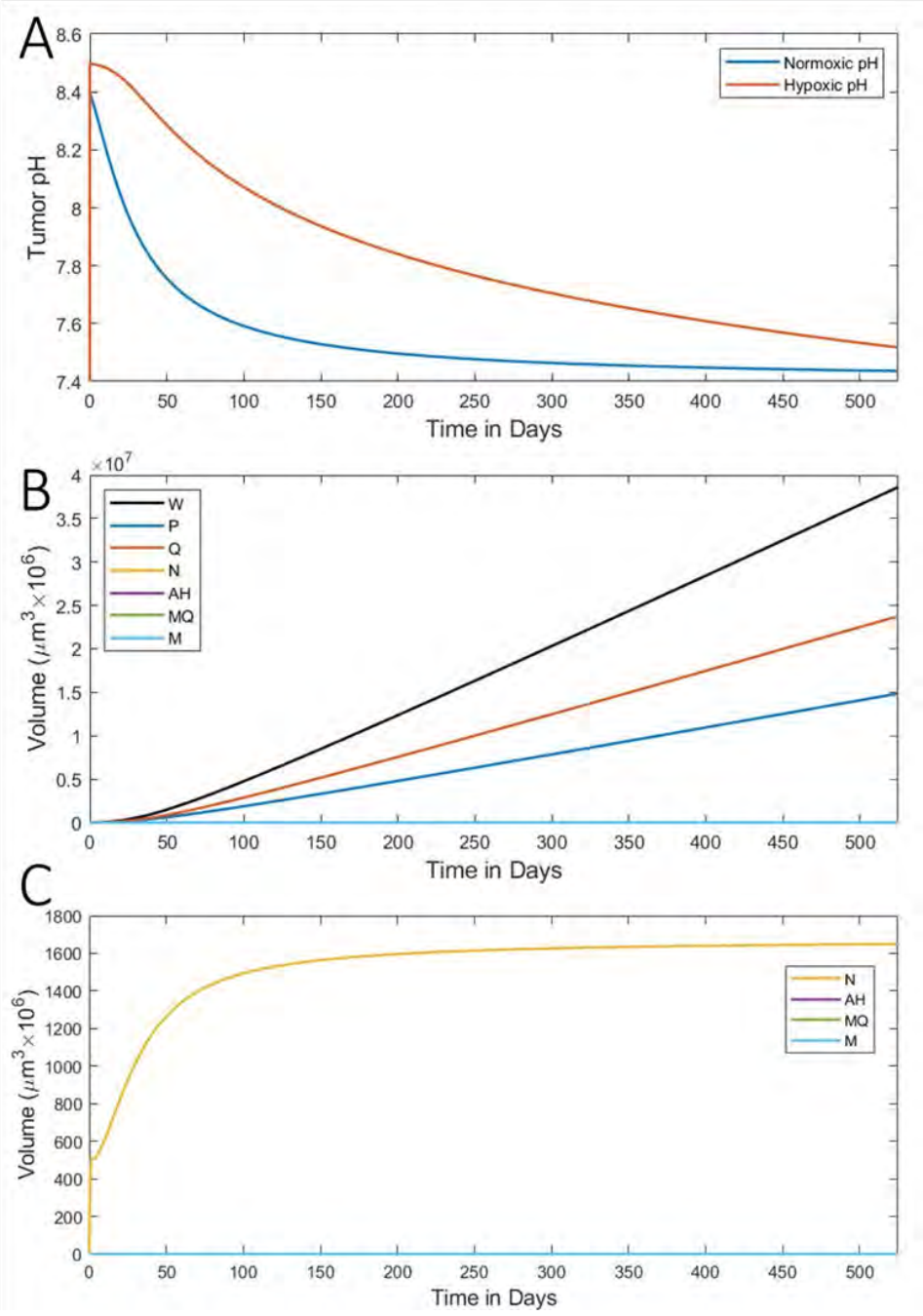

Figure 4.1: This figure shows the result of early buffer therapy on the acid levels and tumor volume. Panel A shows the pH of the normoxic region (comprised of P and M) in blue and that of the hypoxic region (comprised of Q, A_H, M_Q) in red upon the administration of buffer therapy at simulation day zero. Panel B shows the long-term trends in the volume of the various compartments (note that there are no malignant cells); the only visible compartments are the proliferative cells in blue, quiescent cells in red, and the whole tumor volume in black. Panel C shows the compartments which attained volumes much lower than those of W, P, and Q to visualize their dynamics.

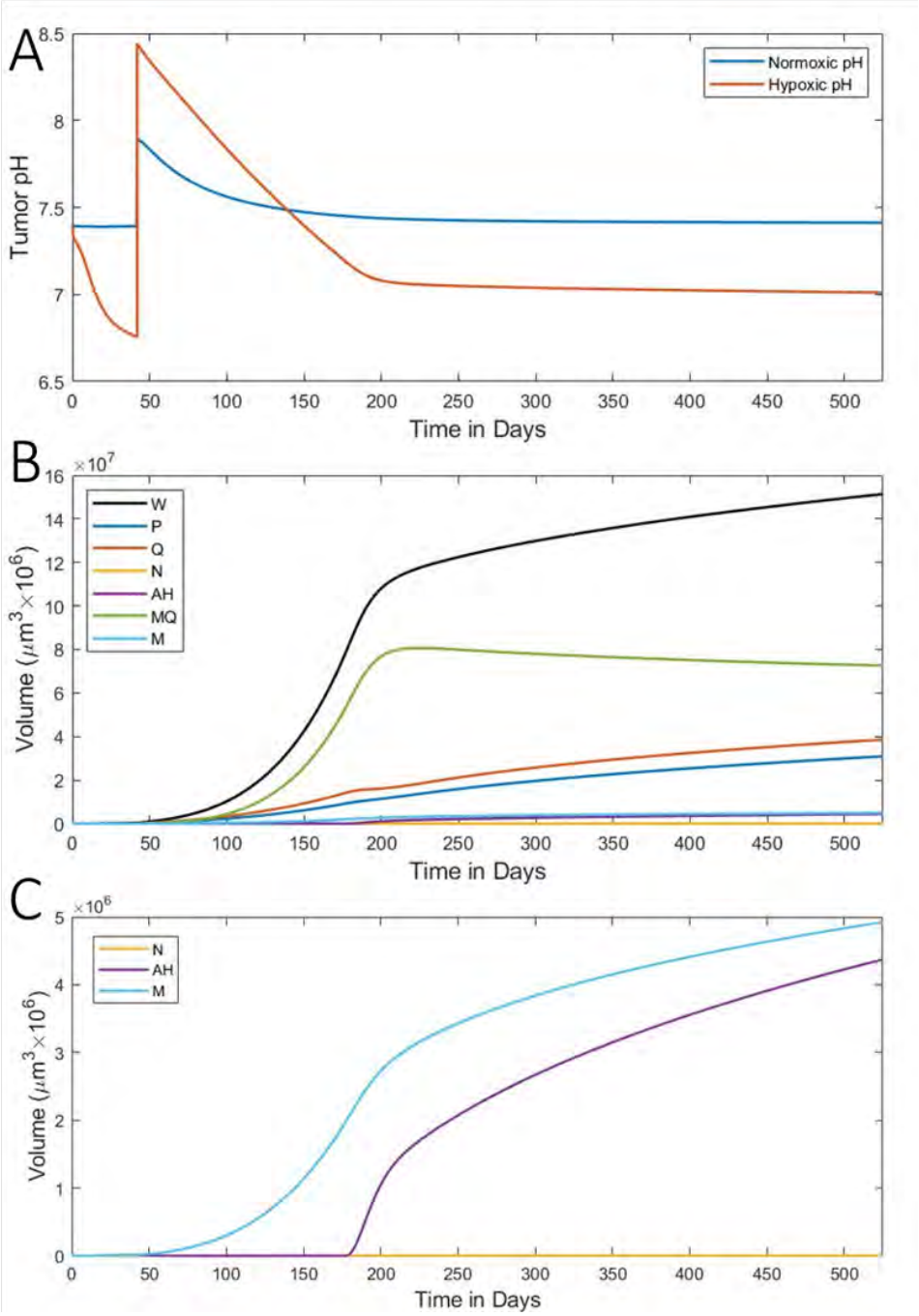

Figure 4.2: This figure shows the results of the late administration of buffer therapy on acid levels and tumor volume. Panel A shows the pH of the normoxic cell compartments in blue and that of the hypoxic compartments in red. Panel B shows the long-term trends of the volumes of the various compartments. Because the volumes of W, M_Q, P, and Q were much greater than other compartments, those of N. A_H, M_Q, and M are displayed in panel C to capture their dynamics.

The early administration of buffer therapy in this *in silico* experiment as shown in Figure 4.1 captures the complete prevention of development of malignancy as observed by Ibrahim-Hashim et al. in the lab.[28] With sufficiently early intervention, the pH of the hypoxic region is unable to reach the threshold at which acid resistant and subsequently malignant cells are hypothesized to develop and as such, acid is unable to drive the tumor toward a malignant and aggressive phenotype. The failure to prevent malignancy with therapy administered six weeks later (at ten weeks of age) is also captured by the model as observed in Figure 4.2.

Interestingly, when buffer therapy is administered late in this model, the malignant cells are able to attain population sizes that exceed those in untreated tumors resulting in a tumor that is more aggressive than it would have been without intervention. This appears to occur because the tumor has adequate time to secrete acid and thereby start the process of the acquisition of acid resistance and malignancy but the buffer therapy then raises the pH above the threshold at which cells die from acid exposure. This leads to a tumor with two growth periods, rapid growth upon the administration of buffer (as seen from day 100 to 200) followed by a slowing of tumor growth which resembles the model without buffer therapy after the pH of the tumor has returned to a lower and harmful level.

Section 4.2

Changes in Angiogenesis

The level of VEGF produced in the model is controlled by two parameters, c_R and c_{qv}. The parameter c_R controls the rate in which the cells in the normoxic proliferative and malignant compartments (P and M) generate VEGF under the influence of

TNF$-\alpha$ while c_{qv} controls the production of VEGF by quiescent, acid resistant, and quiescent malignant cells. The effects of changing these two parameters can be seen in Figure 4.3

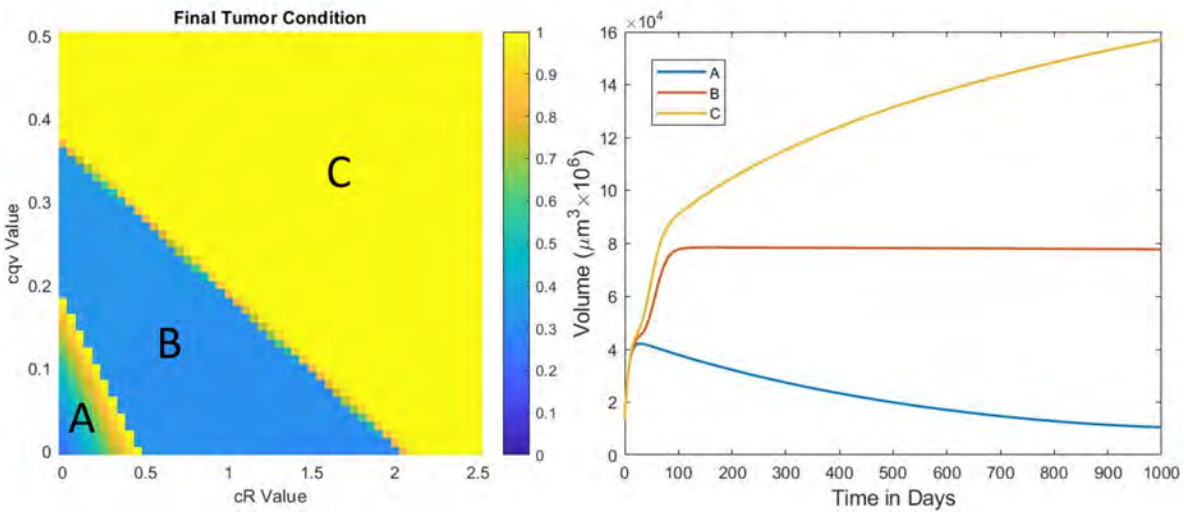

Figure 4.3: The panel at left is a heatmap for which each pixel represents the normalized final tumor volumes in a 1000-day simulation where the x-axis shows the input value of the c_R parameter and the y-axis shows the input value of the c_{qv} parameter. There are three distinct regions of parameter combinations corresponding to three simulation behaviors, denoted A, B, and C. In the heat map, yellow indicates a large tumor volume relative to the maximum and blue represents a smaller tumor volume relative to the maximum. Representative curves for each of the three regions are shown in the panel at right which represents change in whole tumor volume over time.

To visualize the impacts of various combinations of these parameters, a heat map of normalized final tumor volumes (final tumor volume after 1000 days divided by maximum tumor volume attained during the 1000 days) was generated. This heat map shows three distinct regions, each corresponding to a different behavior of the system. Three distinct behaviors are observed when the parameters controlling angiogenesis are varied: death of the tumor, an equilibrium tumor size, and indefinite increase in tumor size. A plot of the ratios of malignant cells to whole tumor volume

and non-malignant cells to whole tumor volume for each of the three aforementioned cases is presented below in Figure 4.4.

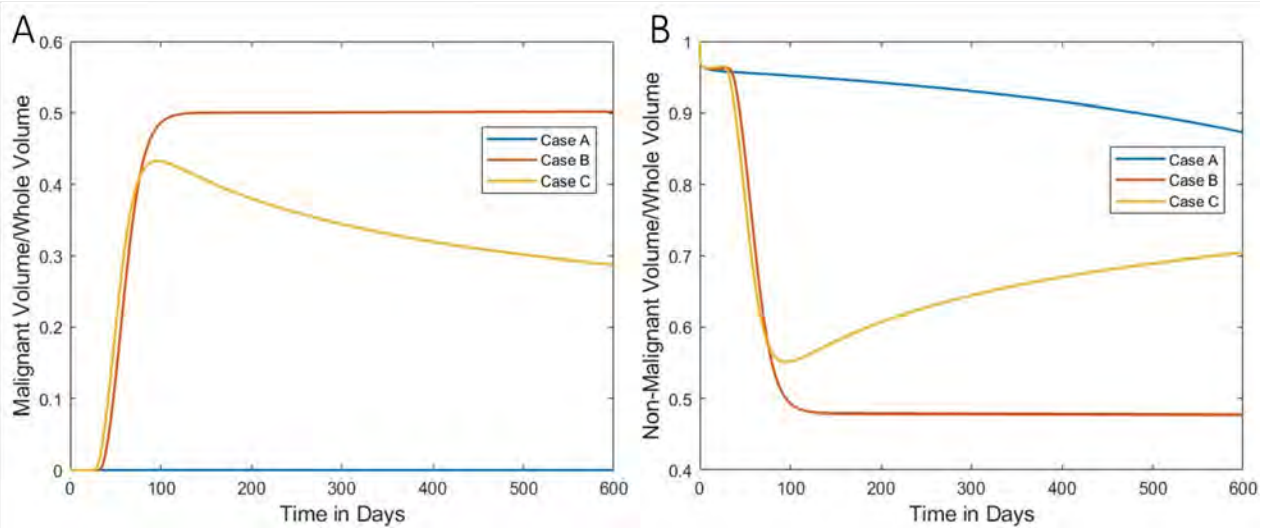

Figure 4.4: Panel A shows the ratio of the volume of the malignant compartments (M and M_Q) to the whole tumor volume over time for each of the three cases described above. Panel B shows the ratio of the volume of the non-malignant compartments (P, Q, A_H) to the whole tumor volume over time. Case A is shown in Blue, Case B is shown in Red, and Case C is shown in yellow.

4.2.1. Case A - Tumor Death

To visualize Case A, the conditions under which the tumor population declines with time, a representative simulation was carried out with parameters:

$$(c_R, c_{qv}) = (0.005, 0.0015)$$

The various compartment volumes of the tumor are visualized below in Figure 4.5.

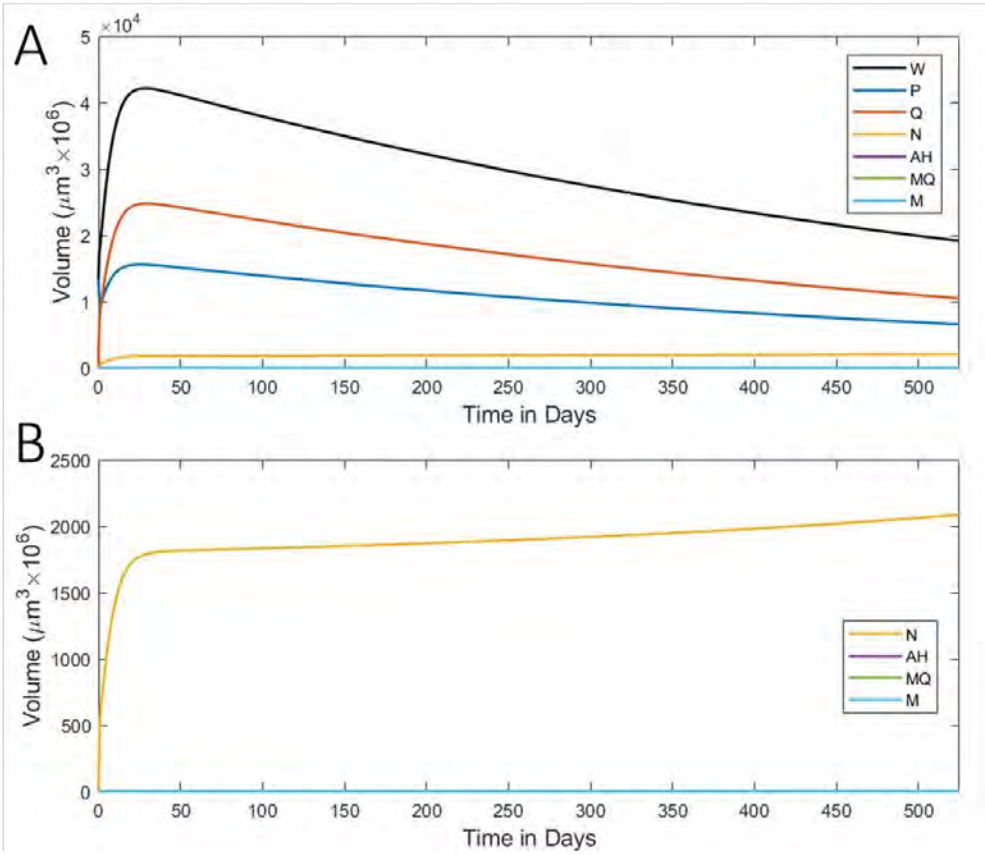

Figure 4.5: This figure is a representative simulation of the "Case A" scenario. Here, panel A shows the volumes of all of the tumor compartments and the whole tumor volume over a 550 day simulation. Because the volumes of N, A_H, M_Q, and M are small compared to W, P, and Q, these are plotted alone in Panel B to visualize their dynamics; the acid resistant and malignant cells do not enter the model here.

Note that the only compartments that are making a significant contribution to the total tumor size are P, Q, and N although the necrotic compartment is considerably smaller than the viable compartments. The acid resistant and malignant compartments all have a volume of zero under these vascular conditions. Next, the various secreted factors and the vasculature are visualized as subplots in Figure 4.6 to evaluate the relative roles of each factor on the death of the tumor.

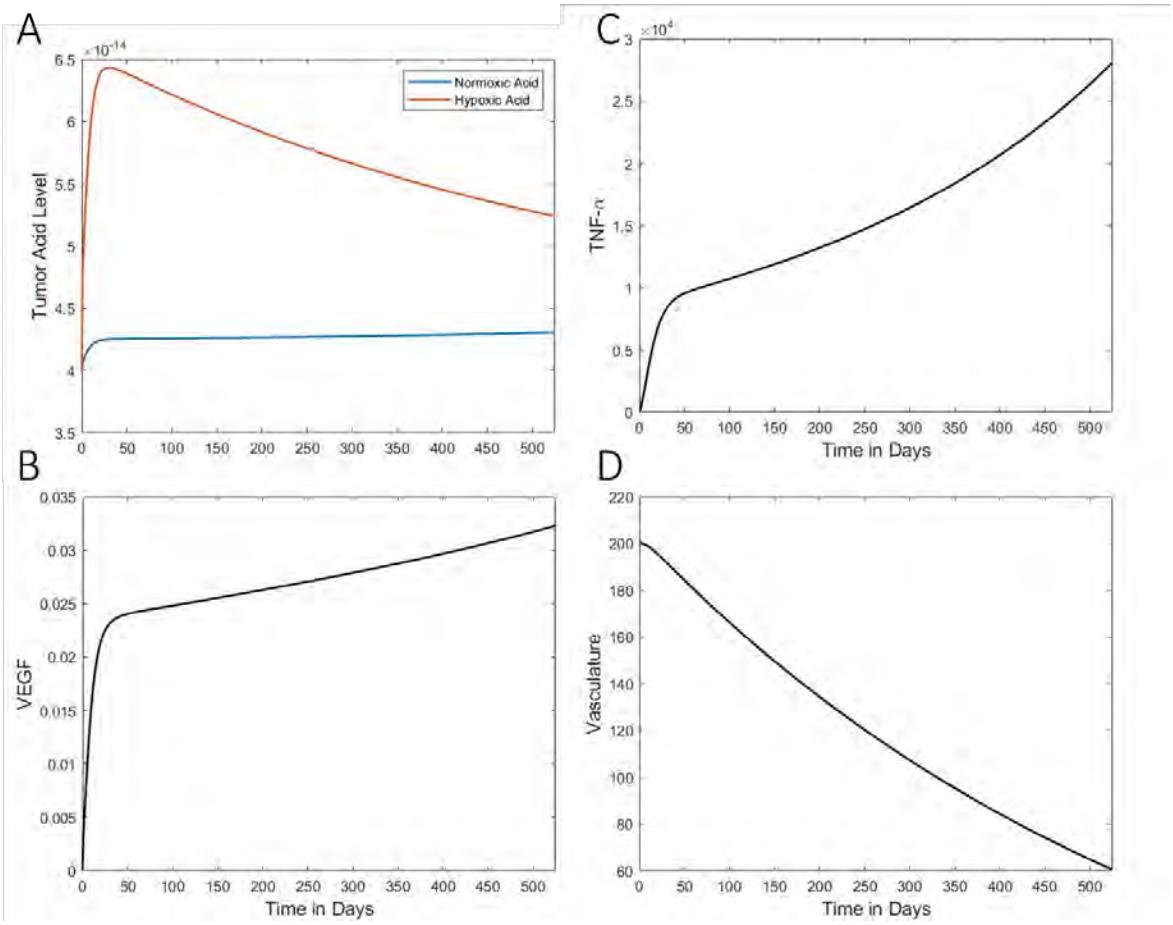

Figure 4.6: Panel A shows the concentration of acid in the normoxic region (blue) and the hypoxic region (red). Panel B shows the change in VEGF level over the duration of the 550 day simulation. Panel C shows the TNF-α level throughout the simulation. Panel D shows the change in vasculature over time.

Over the 550 day period, the acid level of the hypoxic region declines while TNF-α increases. This suggests that the acid is not responsible for the regressing tumor volume but rather that TNF-induced apoptosis is important. Additionally, despite an increasing level of VEGF, the vasculature is lost as the tumor volume decreases, so it is likely that the cells are oxygen deprived which also contributes to their death; they signal for vasculature but VEGF is inadequate to stimulate angiogenesis.

4.2.2. Case B - Size Equilibrium

To visualize Case B, a tumor with volume that reaches a stable equilibrium, the following parameters were entered in the model:

$$(c_R, c_{qv}) = (1, 0.2)$$

As with case A, the volumes of the various compartments of the tumor are plotted in Figure 4.7

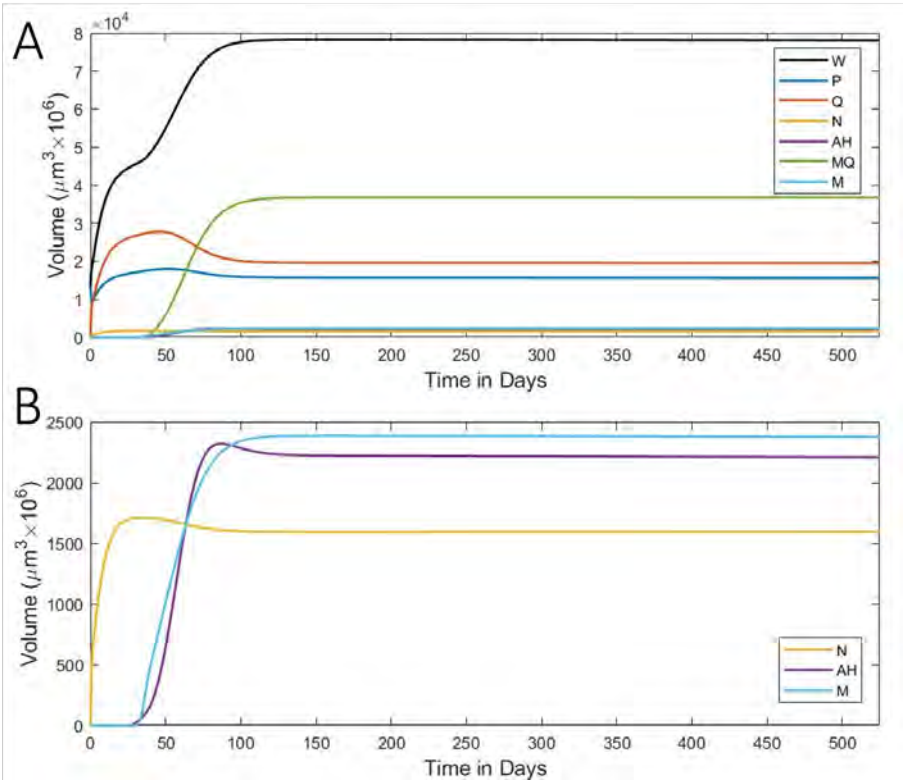

Figure 4.7: This figure is a representative simulation of the "Case B" scenario. Panel A shows the volumes of the tumor compartments and the whole tumor volume over a 550 day simulation. The volumes of N, A_H, and M are considerably smaller than those of W, P, and Q, and M_Q so the smaller compartments are plotted alone in Panel B to visualize their dynamics.

The quiescent malignant cells are the greatest contributor to the whole tumor volume in case B which is in a strong contrast to the entirely nonmalignant cells of Case A which had low angiogenesis. Here, all of the tumor compartments reach a non-zero equilibrium by day 150. Plots of the various other factors are presented in Figure 4.8.

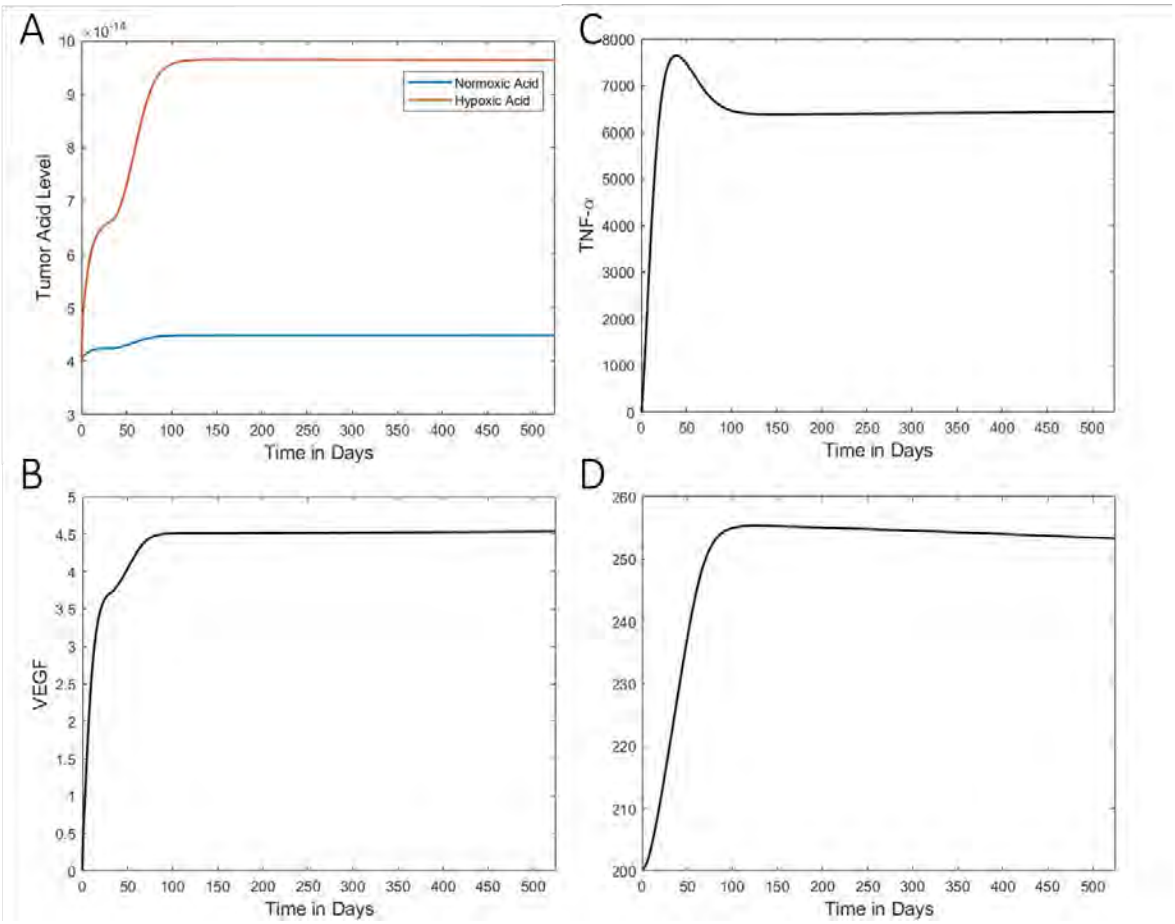

Figure 4.8: Panel A shows the concentration of acid in the normoxic region (blue) and the hypoxic region (red). Panel B shows VEGF, Panel C shows TNF-α, and Panel D shows the change in vasculature over time.

Acid, TNF-α, and VEGF all equilibrate and the TNF-α level is considerably lower than that in Case A while VEGF and acid are considerably higher.

4.2.3. Case C - Unhindered Growth

The final scenario of interest is Case C, a tumor with volume that grows indefinitely. The following parameters were entered in the model:

$$(c_R, c_{qv}) = (2, 0.4)$$

As in the previous cases, the volumes of the various compartments of the tumor are plotted in Figure 4.9

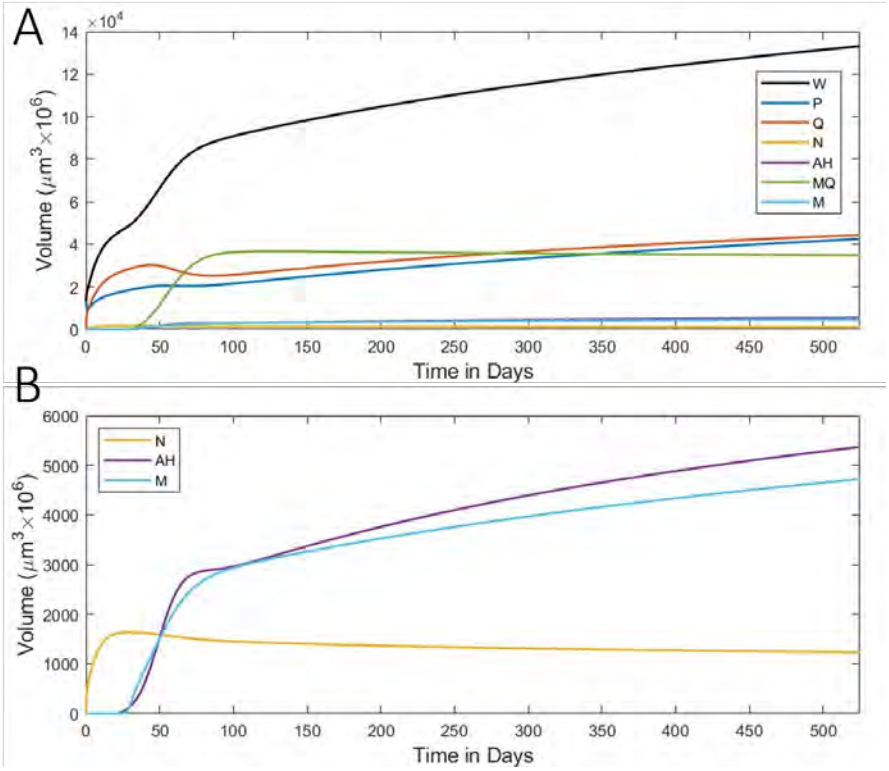

Figure 4.9: This figure is a representative simulation of the "Case C" scenario. Panel A shows the volumes of the tumor compartments and the whole tumor volume over a 550 day simulation. The volumes of N, A_H, and M are considerably smaller than those of W, P, and Q, and M_Q so the smaller compartments are plotted alone in Panel B to visualize their dynamics.

As shown in Figure 4.9, the tumor grows indefinitely but several compartments reach a steady state (M_Q and N). In the first 30 days, the growth of the tumor is primarily due to the proliferative compartment (P), then between day 30 and day 80 the growth of the quiescent malignant compartment is the driver of tumor growth, after which point M_Q equilibrates and compartments P and Q with minor contributions from A_H and M are the drivers of tumor growth. The dynamics of the various secreted factors are now plotted in Figure 4.10.

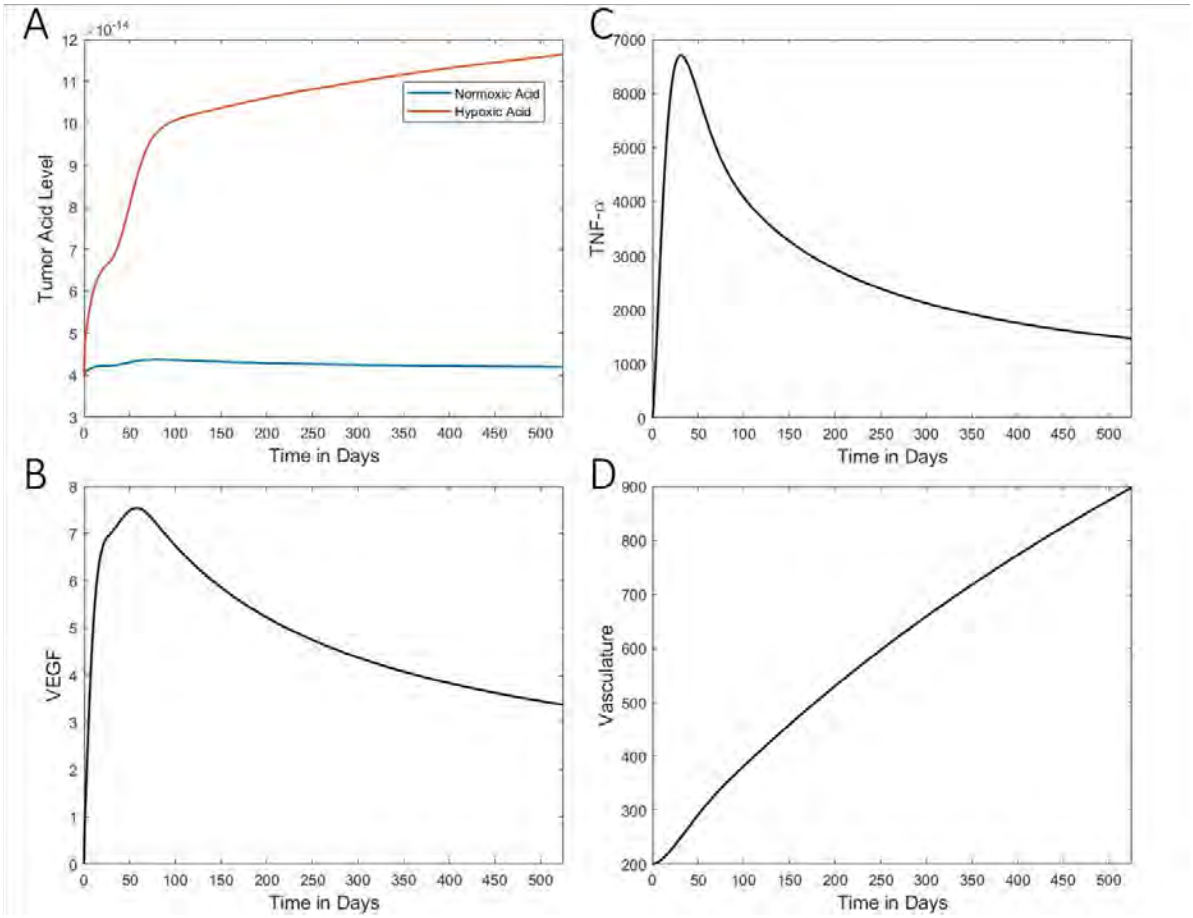

Figure 4.10: Panel A shows the concentration of acid in the normoxic region (blue) and the hypoxic region (red). Panel B shows VEGF, Panel C shows TNF-α, and Panel D shows the change in vasculature over time.

Chapter 5

Sensitivity Analysis

Two methods are used here to evaluate the sensitivity of the model to the various parameters. Tornado plots are generated by running simulations in which all of the parameters remain constant, each parameter is increased by ten percent while the others remain constant, and each parameter is decreased by ten percent while the rest remain constant. An additional analysis was carried out for the xenograft in which a Latin hypercube was generated such that all of the parameters are simultaneously varied randomly with limits of an increase or decrease of ten percent from the original parameter value.

5.0.1. Spheroid Sensitivity

First, the spheroid was analyzed without acidosis to determine the relative impacts of the various parameters controlling spheroid growth. Figure 5.1 shows the tornado plot for a spheroid without acidosis. This is plotting the sum of the whole spheroid volume over all the time steps on the x axis to represent the sensitivity of the model to the changing parameters.

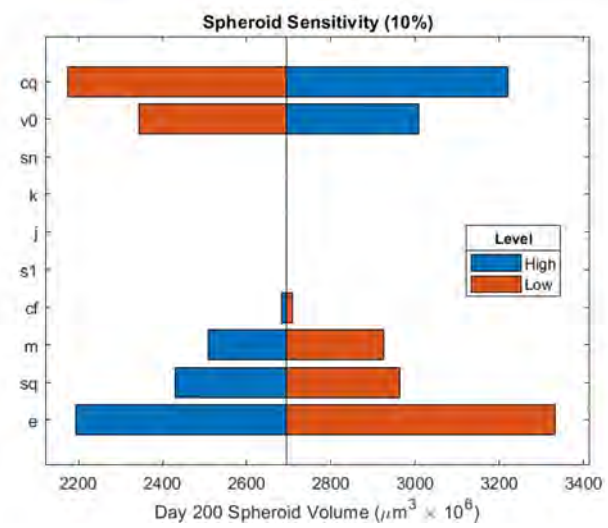

Figure 5.1: A tornado plot for the spheroid where the final spheroid volume in a 200 day period is plotted on the x-axis and the parameters that were permitted to change in the spheroid parametrization are listed on the y-axis. Blue or "high level" denotes that the parameter was increased by 10% and red or "low level" indicates that the parameter was decreased by 10%. The only parameters that are shown here are those that were permitted to vary in the initial parametrization of the spheroid without acidosis.

As seen in the above figure, the most significant parameters for the value of the whole spheroid volume are c_q, v_0, m, s_q, e.

Spheroid with Acidosis. The sensitivity of the spheroid model with acidosis was evaluated at several time points: day 30, 60, and 200. These correspond to times at which the population of cells is increasing maximally (30), the time at which the population reaches its maximum value (60), and a time at which the subpopulations have equilibrated (200). The tornado diagrams in Figure 5.2 reflect the values for the total spheroid volume and the average tumor pH for the three times of interest when the various parameters are increased ten percent, decreased ten percent, or left as they are in the original parametrization; all other parameters remain fixed.

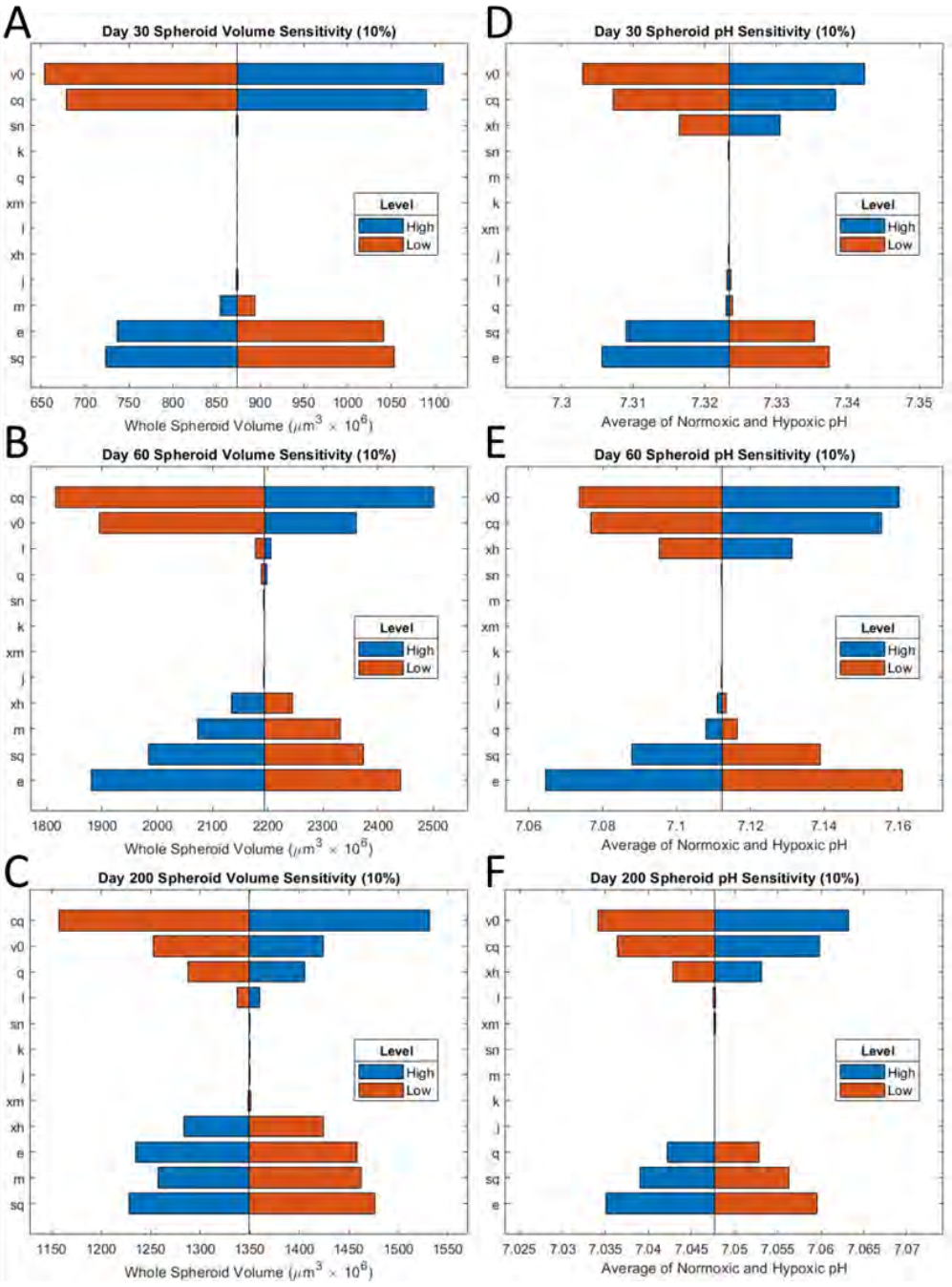

Figure 5.2: This figure contains tornado plots for the aforementioned time points, day 30, 60, and 200. Panels A-C show tornado plot for the tumor volume at each of the time points of interest where the parameter marked on the y-axis was either increased by 10%, decreased by 10%, or left the same while all other parameters were held constant; the x-axis shows the tumor volume. Panels D-F show the tornado plots for the pH averaged across the hypoxic and normoxic tumor compartments for each of the time points with the parameters again increased or decreased by 10% or held constant while all other parameters remained constant; the x-axis shows average pH. Blue or "high level" denotes that the parameter was increased by 10% and red or "low level" indicates that the parameter was decreased by 10%.

The parameters selected for the analysis of the spheroid with acidosis were those which had the greatest impact for the simple spheroid model (c_q, v_0, m, s_q, e), those involved in the generation and impact of TNF$-\alpha$ (j, k, s_n), and those involved in acidosis (x_m, l, q, x_h). These specific parameters are of interest as they may help elucidate the relative importance of TNF$-\alpha$ and acidosis in the cessation in the growth of the spheroid which stabilizes in volume over time.

5.0.2. *In Vivo* Sensitivity

The whole tumor growth in the full *in vivo* model is characterized by two phases, a logistic growth phase at the earliest time points followed by a constant growth rate and thus a linear increase in tumor volume. This trend and a linear fit to the linear portion of the curve is presented below in Figure 5.3.

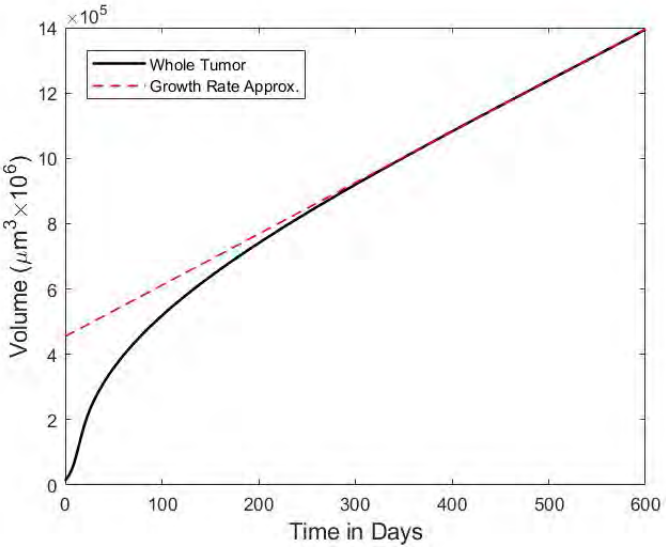

Figure 5.3: This figure shows the whole tumor volume over time for the parametrization established in Chapter 3 in black and its linear regression corresponding to the tumor growth rate during the late time points of the simulation when tumor growth is linear.

The slope of the terminal growth phase of the whole tumor is thus defined as the tumor growth rate. This value is obtained using the MATLAB gradient function on the whole tumor volume and the value for the gradient is taken at the simulation end time. A tornado diagram was generated to show the response of the tumor's growth rate to alterations in individual parameter values. The tumor growth rate where the parameters were left as they were in the original model parametrization is plotted in the center of the tornado plot. The growth rates when each parameter is increased by ten percent while the others remain unaltered are shown as blue bars and those where each parameter is decreased by ten percent while the others remain unaltered are marked by red bars. This tornado diagram can be seen below in Figure 5.4

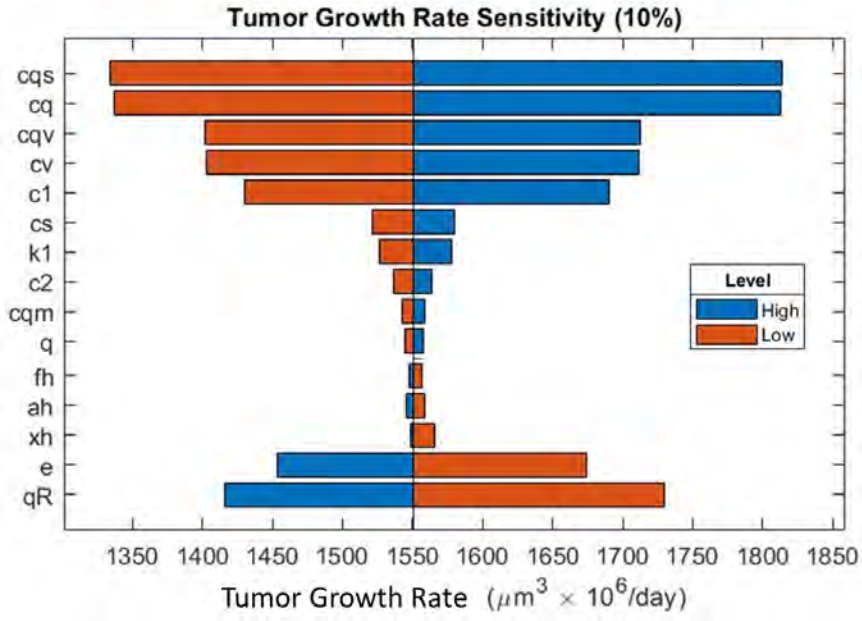

Figure 5.4: A tornado plot for the whole *in vivo* model where the tumor growth rate is plotted on the x-axis and the parameters that were permitted to change in the parametrization that yielded the greatest shifts in tumor growth rate are listed on the y-axis. Blue or "high level" denotes that the parameter was increased by 10% and red or "low level" indicates that the parameter was decreased by 10%.

The tornado diagrams only allow for a determination of the role of parameters with a fixed increase or decrease in their value and all other parameters must be held constant. The parameters do not act in isolation, however, so a secondary analysis was carried out in which all of the parameters were simultaneously varied by random amounts. The full model has 36 parameters so a 36×360 Latin hypercube, the n-dimensional generalization of a Latin square, was generated using MATLAB with all entries ranging from zero to one to generate a near-random distribution of parameter values. The following was then carried out on each entry of the hypercube (denoted here as LH) to give a value by which the parameters could be multiplied such that the parameters can range from a decrease in 10% to and increase in 10% of their value.

$$(LH - 0.5) \cdot 0.1 + 1$$

A vector of the parameters was multiplied component-wise by every row of the hypercube and the resultant matrix thus corresponded to a set of 360 parametrizations for the model. The results of these simulations are presented in Figure 5.5; a scatter plot and linear regression was generated for every pairing of parameter value (on the x-axis) and tumor growth rate (on the y-axis). A linear regression of the data points for each parameter was carried out and the correlation coefficient (r) is listed with the parameter being plotted above each subplot.

Figure 5.6 then shows every parameter and its associated correlation coefficient in a similar format to the previous tornado plot in Figure 5.4 so that they can be compared.

Figure 5.5: Using a Latin Hypercube, 360 randomized parameter combinations were generated within the parameter value ±10%. The values for the parameters were plotted on the x-axes and the tumor's ultimate growth rate was plotted on the y-axis. Correlation coefficients were determined for each pairing of parameter and the tumor growth rate; the parameter and correlation coefficient are listed above each subplot. Any parameter with correlation greater than the arbitrary value of 0.3 is marked with two asterisks.

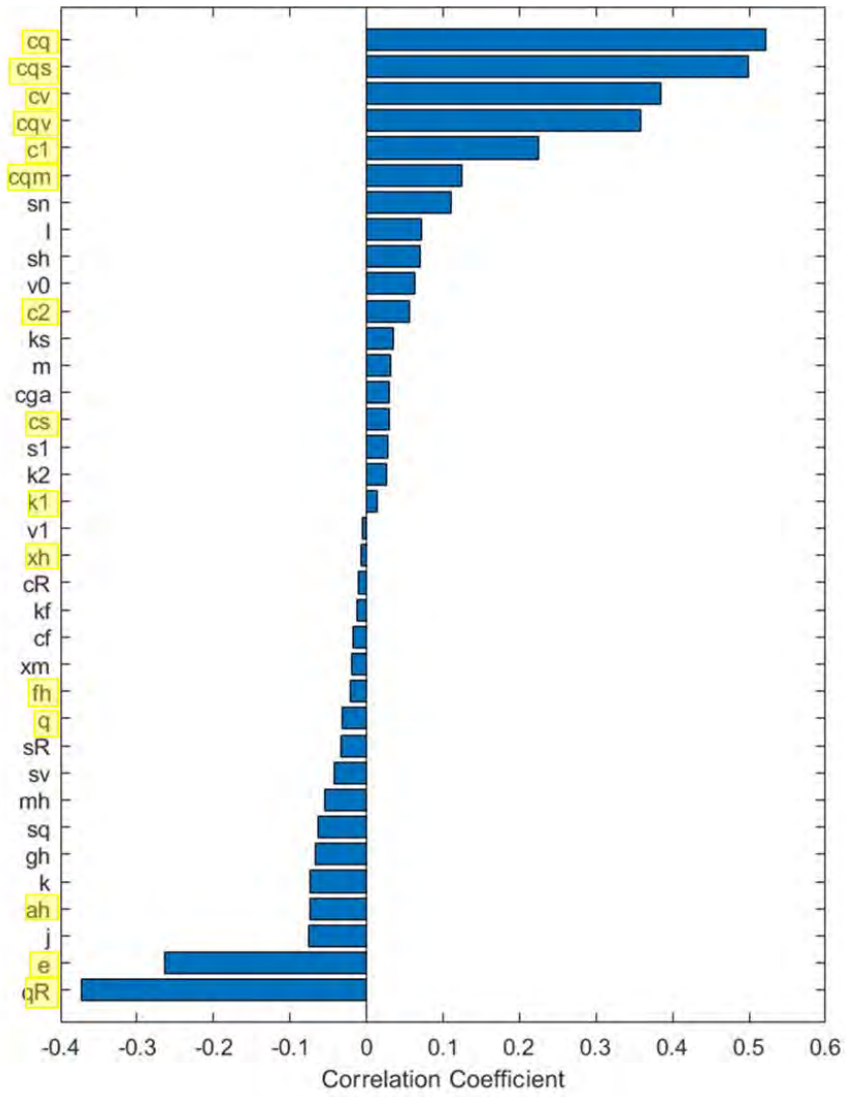

Figure 5.6: This figure presents the correlation coefficient r corresponding to each model parameter as determined from the Latin Hypercube analysis of the parameter correlations to terminal tumor growth rate. The figure is presented such that parameters which had a positive correlation with the tumor growth rate are presented to the right and those with a negative correlation are presented to the left similar to a tornado plot. The parameters which appeared as significant contributors in the original tornado plot are highlighted in yellow along the y-axis.

It should be noted that the parameters that caused the greatest increase in tumor growth rate in the analysis that yielded the tornado plot in Figure 5.4 ($c_{qs}, c_q, c_{qv}, c_v, c_1$) are also the five most highly correlated to an increase in tumor growth rate in the Latin hypercube analysis although their order is not the same. Additionally, the parameters which, when increased 10% for the tornado plot generated the greatest decrease in tumor growth rate (q_R, e) also had the strongest negative correlations for the Latin hypercube analysis. These two analyses are in agreement that perhaps the most important parameters to the terminal tumor growth rate in this model are:

$$c_{qs}, c_q, c_{qv}, c_v, c_1, q_R, \text{ and } e$$

Chapter 6

Equilibrium Analysis

There are likely several equilibria present in this model, three conditions will be explored: the disease-free equilibrium, an equilibrium in which the only cancer cells are malignant, and proof that there cannot be an equilibrium for which the cancer cells are only non-malignant given the assumptions presented in this paper. The disease-free equilibrium will be evaluated both for the spheroid and for the full xenograft model.

Section 6.1

Disease-Free Equilibrium - Spheroid

For the equilibrium to be disease free, the following compartments must equal zero at equilibrium:

$$G_1, S, G_2, Q, A_H, M_Q, M_{G1}, M_S, M_{G2} = 0$$

Thus, it is only necessary to determine equilibrium values for $N, T, V, L_1,$ and L_2. Substituting zero for the disease terms, the following equilibria are determined.

Necrotic Cells:

$$\begin{aligned} \frac{dN}{dt} = 0 &= -m(v_0 + V)N \\ 0 &= N^* \end{aligned} \tag{6.1}$$

TNF-α:

$$\begin{aligned} \frac{dT}{dt} = 0 &= jN - kv_0T \\ 0 &= 0 - k(v_0)T \\ 0 &= T^* \end{aligned} \tag{6.2}$$

Hypoxic Region Acid (L_1):

$$\begin{aligned} \frac{dL_1}{dt} = 0 &= -l(L_1 - L_2) \\ L_1^* &= L_2^* \end{aligned} \tag{6.3}$$

Normoxic Region Acid (L_2):

$$\begin{aligned} \frac{dL_2}{dt} = 0 &= -l(L_2 - L_1) + q(3.9810717 \times 10^{-14} - L_2)(V + v_1) \\ 0 &= 0 + q(3.9810717 \times 10^{-14} - L_2)(V + v_1) \\ L_2^* = L_1^* &= 3.9810717 \times 10^{-14} \end{aligned} \tag{6.4}$$

Thus, the Jacobian on the following page is generated with all variables set to zero except L_1 and L_2 which have value $3.9810717 \times 10^{-14} mmol/(10^6 \mu m^3)$ which is equivalent to physiological pH.

	$\frac{\partial}{\partial G_1}$	$\frac{\partial}{\partial S}$	$\frac{\partial}{\partial G_2}$	$\frac{\partial}{\partial Q}$	$\frac{\partial}{\partial N}$	$\frac{\partial}{\partial T}$	$\frac{\partial}{\partial A_H}$	$\frac{\partial}{\partial M_1}$	$\frac{\partial}{\partial M_S}$	$\frac{\partial}{\partial M_2}$	$\frac{\partial}{\partial M_Q}$	$\frac{\partial}{\partial L_1}$	$\frac{\partial}{\partial L_2}$
$\frac{dG_1}{dt}$	$-c_1$	0	$2c_2$	0	0	0	0	0	0	0	0	0	0
$\frac{dS}{dt}$	$c_1 B$	$-c_s$	0	C	0	0	0	0	0	0	0	0	0
$\frac{dG_2}{dt}$	0	c_s	$-c_2 - d_a$	0	0	0	0	0	0	0	0	0	0
$\frac{dQ}{dt}$	$c_1(1-B)$	0	0	$-e - C$	0	0	0	0	0	0	0	0	0
$\frac{dN}{dt}$	0	0	0	e	$-mv_0$	0	0	0	0	0	0	0	0
$\frac{dT}{dt}$	0	0	0	0	j	$-kv_0$	0	0	0	0	0	0	0
$\frac{dA_H}{dt}$	0	0	0	0	0	0	$c_{ga} - m_h$	0	0	0	0	0	0
$\frac{dM_1}{dt}$	0	0	0	0	0	0	0	$-k_1$	0	$2k_2$	0	0	0
$\frac{dM_S}{dt}$	0	0	0	0	0	0	0	$k_1 B_M$	$-k_s$	0	C_M	0	0
$\frac{dM_2}{dt}$	0	0	0	0	0	0	0	0	k_s	$-k_2 - d_a$	0	0	0
$\frac{dM_Q}{dt}$	0	0	0	0	0	0	m_h	$k_1(1 - B_M)$	0	0	$-C_M$	0	0
$\frac{dL_1}{dt}$	0	0	0	x_h	0	0	x_h	0	0	0	x_h	$-l$	l
$\frac{dL_2}{dt}$	0	0	0	0	0	0	0	x_m	x_m	x_m	0	l	$-l - q$

6.1.1. Model Stability

While it is possible to establish feasible conditions under which the disease-free equilibrium for the spheroid model with acidosis must be stable, these criteria are unlikely to be attained by tumors physiologically. These criteria are determined below where all parameters are taken to be strictly positive. The Jacobian for the acidotic spheroid model is a block triangular matrix. As such, the Jacobian can be partitioned into four blocks, from left to right: a four-by-four, a three-by-three, a four-by-four, and in the bottom right a two-by-two. From "Mathematical Tools for Data Mining: Set Theory, Partial Orders, Combinatorics", if A is a block lower triangular partitioned matrix,

$$\begin{pmatrix} A_{11} & 0 & ... & 0 \\ A_{21} & A_{22} & ... & 0 \\ \vdots & \vdots & \ddots & \vdots \\ A_{m1} & A_{m2} & ... & A_{mm} \end{pmatrix}$$

where $A_{ii} \in R^{p_i \times p_i}$ and $1 \leq i \leq m$, then $spec(A) = \bigcup_{i=1}^{m} spec(A_{ii})$.[38] As such, the eigenvalues of the Jacobian will be determined from the eigenvalues of the blocks as described below.

Block A_{11}. Because block A_{11} is 4×4, its eigenvalues are not straightforward to evaluate algebraically. As such Gerschgorin's Circle theorem is employed to determine the ranges within which the eigenvalues can lie and thus determine criteria for stability. Gerschgorin's Circle Theorem [40] states every eigenvalue for a square matrix must lie within the union of disks in the complex plane centered on diagonal elements, a_{ii}, with a radii defined by the sum of the absolute values of all off-diagonal elements in the i^{th} row:

$$R_i = \sum_{j=1, i \neq j}^{n} \mid a_{ij} \mid$$

Both B and B_M must be less than one. The Gerschgorin Disk radii are computed for the four rows of A_{33} and the signs of their corresponding eigenvalues are discussed below:

(a) **Disk 1** ($i = 1$): $R_1 = 2c_2$

The maximum and minimum eigenvalues associated with this disk are $a_{1,1} \pm R_1$. Thus, if there are eigenvalues contained in this disk the real parts of the eigenvalues can range from

$$-c_1 - 2c_2 \text{ to } -c_1 + 2c_2$$

This will always be negative where $c_1 > 2c_2$.

(b) **Disk 2** ($i = 2$): $R_2 = c_1 B + C$

The real parts of eigenvalues bounded within disk 2 can range from

$$-c_s - c_1 B - C \text{ to } -c_s + c_1 B + C$$

Plugging in the functional forms for B and C, the eigenvalues could range from

$$-c_s - c_1 \frac{v_0}{s_1 + v_0} - c_q \frac{v_0}{s_q + v_0}$$

to

$$-c_s + c_1 \frac{v_0}{s_1 + v_0} + c_q \frac{v_0}{s_q + v_0}$$

This is always negative where

$$c_s > c_1 \frac{v_0}{s_1 + v_0} + c_q \frac{v_0}{s_q + v_0}$$

It should be noted however that both $\frac{v_0}{s_1+v_0}$ and $\frac{v_0}{s_1+v_0}$ are necessarily less than one as the denominators are the sum of the numerator and another positive number. Thus, the above criterion for which the disk must be negative can be simplified to

$$c_s > c_1 + c_q$$

(c) **Disk 3** ($i = 3$): $R_3 = c_s$

The real parts of the eigenvalues bounded within disk 3 can range from

$$-c_s - c_2 - d_a \text{ to } c_s - c_2 - d_a$$

This is always negative where $c_2 + d_a > c_s$

(d) **Disk 4** ($i = 4$): $R_4 = c_1(1 - B)$

The real parts of the eigenvalues bounded within disk 4 can range from

$$-e - C - c_1(1 - B) \text{ to } -e - C + c_1(1 - B)$$

The ranges can be rewritten as

$$-e - c_q\frac{v_0}{s_q + v_0} - c_1\Big(1 - \frac{v_0}{s_1 + v_0}\Big)$$

to

$$-e - c_q\frac{v_0}{s_q + v_0} + c_1\Big(1 - \frac{v_0}{s_1 + v_0}\Big)$$

All of the real parts of this disk are negative where

$$e + c_q\frac{v_0}{s_q + v_0} > c_1\Big(1 - \frac{v_0}{s_1 + v_0}\Big)$$

As before, the fraction $\frac{v_0}{s_1+v_0}$ is necessarily less than 1, and thus the above condition will still be true where:

$$e + c_q\frac{v_0}{s_q + v_0} > c_1$$

Thus, there are conditions established for the parameters such that the four eigenvalues associated with block A_{11} will all be negative. There is a corollary to Gerschgorin's Circle theorem which utilizes the columns that will be evaluated to determine if there is a better statement of the parameter requirements.

Corollary. All eigenvalues for a square matrix must lie within the union of disks in the complex plane centered on diagonal elements, a_{jj}, with radii defined by the

sum of the absolute values of all off-diagonal elements in the j^{th} column:

$$C_j = \sum_{i=1, j \neq i}^{n} \mid a_{ij} \mid$$

The Gerschgorin Disks for the four columns of the block are evaluated below:

(a) **Disk 1** ($j = 1$): $C_1 = c_1$

The eigenvalues that could be associated with this disk range from $-2c_1$ to 0. This will always be negative.

(b) **Disk 2** ($j = 2$): $C_2 = c_s$

The second disk ranges from $-2c_s$ to 0. This disk is always negative.

(c) **Disk 3** ($j = 3$): $C_3 = 2c_2$

Disk three ranges from $-3c_2 - d_a$ to $c_2 - d_a$ This disk is always negative if $d_a > c_2$.

(d) **Disk 4** ($j = 4$): $C_4 = C + e$

The fourth disk ranges from $-2e - 2C$ to 0. This disk is always negative.

Thus, the only requirement for all of the eigenvalues for block 1 to be zero is that $d_a > c_2$.

Block A_{22}. Next, the eigenvalues for the second block, A_{22} are evaluated. The second block presented below is simple to evaluate as it is a lower triangular matrix:

$$\begin{bmatrix} -mv_0 & 0 & 0 \\ j & -kv_0 & 0 \\ 0 & 0 & c_{ga} - m_h \end{bmatrix}$$

The eigenvalues of a lower triangular matrix are the diagonal entries of the matrix and thus the three eigenvalues for block J_{22} are $-mv_0, -kv_0, c_{ga} - m_h$. Because the parameter values are defined to be positive, the eigenvalues $-mv_0$ and $-kv_0$ will always be negative. $c_{ga} - m_h$ will be negative when $m_h > c_{ga}$.

Block A_{33}. Finally, the third block matrix A_{33} is evaluated utilizing Gerschgorin Disks similarly to the first block. Beginning with the rows of the matrix, the following relationships can be determined:

(a) **Disk 1** ($i = 1$): $R_1 = 2k_2$

The real parts of the eigenvalues bounded within disk 1 can range from

$$-k_1 - 2k_2 \text{ to } -k_1 + 2k_2$$

This disk is entirely negative where $k_1 > 2k_2$.

(b) **Disk 2** ($i = 2$): $R_2 = k_1 B_M + C_M$

The real parts of the eigenvalues that could be contained within disk 2 range from

$$-k_s - k_1 B_M - C_M \text{ to } -k_s + k_1 B_M + C_M$$

Substituting in the functional forms for B_M and C_M,

$$-k_s - k_1\frac{v_0}{s_1+v_0} - c_{qm}\frac{v_0}{s_q+v_0}$$

to

$$-k_s + k_1\frac{v_0}{s_1+v_0} + c_{qm}\frac{v_0}{s_q+v_0}$$

This disk is entirely negative where

$$k_s > k_1\frac{v_0}{s_1+v_0} + c_{qm}\frac{v_0}{s_q+v_0}$$

As described previously in block A_{11}, because the fractional terms above must be less than one, the above condition is also true where:

$$k_s > k_1 + c_{qm}$$

(c) **Disk 3** ($i = 3$): $R_3 = k_s$

The real parts of eigenvalues that could be contained within disk 3 range from

$$-k_s - k_2 - d_a \text{ to } k_s - d_a - k_2$$

The disk is entirely negative when $k_2 + d_a > k_s$.

(d) **Disk 4** ($i = 4$): $R_4 = k_1(1 - B_M)$

The real parts of any eigenvalues that could be contained within disk 4 range from

$$-C_M - k_1(1 - B_M) \text{ to } -C_M + k_1(1 - B_M)$$

Substituting in the functional forms, these bounds are equivalent to:

$$-c_{qm}\frac{v_0}{s_q+v_0}-k_1\Big(1-\frac{v_0}{s_1+v_0}\Big)$$

to

$$-c_{qm}\frac{v_0}{s_q+v_0}+k_1\Big(1-\frac{v_0}{s_1+v_0}\Big)$$

The eigenvalues that could be contained in this disk are always negative where

$$c_{qm}\frac{v_0}{s_q+v_0}>k_1\Big(1-\frac{v_0}{s_1+v_0}\Big)$$

Because the fraction $\frac{v_0}{s_1+v_0}$ is less than one, the above is still true where:

$$c_{qm}\frac{v_0}{s_q+v_0}>k_1$$

The aforementioned corollary to Gerschgorin's Circle theorem is evaluated for the columns of this block to again determine if there are simpler relationships between the parameters:

(a) **Disk 1** ($j=1$): $C_1=k_1$

The eigenvalues that can be contained in disk 1 range from $-2k_1$ to 0 and are thus always negative.

(b) **Disk 2** ($j=2$): $C_2=k_s$

The real part of disk 2 ranges from $-2k_s$ to 0 so this disk is also always negative.

(c) **Disk 3** ($j=3$): $C_3=2k_2$

Disk 3 ranges from $-3k_2 - d_a$ to $-d_a + k_2$ and is thus always negative where $d_a > k_2$.

(d) **Disk 4** ($j = 4$): $C_4 = C_M$

Disk 4 ranges from $-2C_M$ to 0 and is also always negative.

Block A_{44}. The determinant for the bottom right block, A_{44} is determined:

$$\begin{aligned} det(A_{44} - \lambda I) = \begin{vmatrix} -l-\lambda & l \\ l & -l-q-\lambda \end{vmatrix} &= (-l-\lambda)(-l-q-\lambda) - l^2 \\ &= l^2 + lq + l\lambda + l\lambda + q\lambda + \lambda^2 - l^2 \\ &= \lambda^2 + (2l+q)\lambda + lq \end{aligned}$$

From the quadratic formula, the eigenvalues for this block are thus:

$$\begin{aligned} \lambda &= \frac{-(2l+q) \pm \sqrt{(2l+q)^2 - 4lq}}{2} \\ &= \frac{-(2l+q) \pm \sqrt{4l^2 + 4lq + q^2 - 4lq}}{2} \\ \lambda &= \frac{-(2l+q) \pm \sqrt{(2l)^2 + q^2}}{2} \end{aligned}$$

For the eigenvalue in which the terms in the numerator are subtracted, the real portion must be negative because all parameters are defined to be positive. Additionally, the eigenvalue for which the numerator terms are added will always be negative because the parameters l and q are taken to be strictly positive and thus:

$$2l + q > \sqrt{(2l)^2 + q^2}$$

$$(2l + q)^2 > (2l)^2 + q^2$$

$$4l^2 + 2lq + q^2 > 4l^2 + q^2$$

$$2lq > 0$$

Thus, the eigenvalues associated with A_{44} are both negative.

Spheroid Stability Criteria. Thus, sufficiency criteria can be established such that all eigenvalues must be negative, thereby corresponding to a stable disease-free equilibrium in the spheroid. Using the relationships from blocks 1 and 3 for which the columns were considered, the criteria are as follows:

(a) $d_a > c_2$

(b) $m_h > c_{ga}$

(c) $d_a > k_2$

These criteria are unlikely to be met physiologically because the death rate of cancer cells is not likely greater than their proliferation rate. Another set of criteria can be established when the Gerschgorin disks associated with the rows of A_{11} and A_{33} are considered. These are stated as follows:

(a) $c_1 > 2c_2$; $c_s > c_1 + c_q$; $c_2 + d_a > c_s$; and $e + c_q \frac{v_0}{s_q + v_0} > c_1$

(b) $m_h > c_{ga}$

(c) $k_1 > 2k_2$; $k_s > k_1 + c_q$; $k_2 + d_a > k_s$; and $c_{qm} \frac{v_0}{s_q + v_0} > k_1$

Criteria (a) and (c) are largely the same here except for the addition of e in the last condition for criterion (a) and as such only one criterion will be discussed. Only considering the second condition of criterion (a), if the nutrients are restricted such that v_0 is sufficiently small, then $c_s > c_1\frac{v_0}{s_1+v_0} + c_q\frac{v_0}{s_q+v_0}$ will necessarily be true and it is under these conditions that the tumor can die and a disease-free equilibrium will be stable. Where v_0 is not small though, then the second criterion is best stated as $c_s > c_1 + c_q$.

Considering the first three conditions from criterion (a), the following emerges:

$$\begin{aligned} c_2 + d_a &> c_s \\ c_2 + d_a &> c_1 + c_q \\ c_2 + d_a - c_q &> c_1 \\ c_2 + d_a - c_q &> 2c_2 \\ d_a &> c_q + c_2 \end{aligned}$$

It is unlikely that $d_a > c_q + c_2$ for the same reason as the criteria from column-derived Gerschgorin disks; it is not likely that a tumor will have a death rate that is greater than its proliferation rate. The same results will occur when considering criterion (c). Thus, unless the nutrients available are severely restricted, a stable disease free equilibrium in the spheroid is biologically unlikely; a stable disease-free equilibrium is however possible under treatment that restricts access of the spheroid to nutrients.

6.1.2. Substituted Parameters

Next, to analyze the stability of the spheroid under its current parametrization, the various parameter values that were found for the spheroid model with acidosis are plugged into the Jacobian yielding the following.

$$\begin{bmatrix}
-1.9618 & 0 & 14.304 & 0 & 0 & 0 & 0 & 0 & 0 & 0 & 0 & 0 & 0 \\
1.2479 & -3.2204 & 0 & 0.8144 & 0 & 0 & 0 & 0 & 0 & 0 & 0 & 0 & 0 \\
0 & 3.2204 & -7.152 & 0 & 0 & 0 & 0 & 0 & 0 & 0 & 0 & 0 & 0 \\
0.7139 & 0 & 0 & -1.2414 & 0 & 0 & 0 & 0 & 0 & 0 & 0 & 0 & 0 \\
0 & 0 & 0 & 0.427 & -0.07946 & 0 & 0 & 0 & 0 & 0 & 0 & 0 & 0 \\
0 & 0 & 0 & 0 & 0.543 & \text{-1.399E-4} & 0 & 0 & 0 & 0 & 0 & 0 & 0 \\
0 & 0 & 0 & 0 & 0 & 0 & -0.3999 & 0 & 0 & 0 & 0 & 0 & 0 \\
0 & 0 & 0 & 0 & 0 & 0 & 0 & -1.9618 & 0 & 14.304 & 0 & 0 & 0 \\
0 & 0 & 0 & 0 & 0 & 0 & 0 & 1.2479 & -3.2204 & 0 & 0.03206 & 0 & 0 \\
0 & 0 & 0 & 0 & 0 & 0 & 0 & 0 & 3.2204 & -7.152 & 0 & 0 & 0 \\
0 & 0 & 0 & 0 & 0 & 0 & 0.4 & 0.7139 & 0 & 0 & -0.03206 & 0 & 0 \\
0 & 0 & 0 & \text{3.91E-18} & 0 & 0 & \text{3.91E-18} & 0 & 0 & 0 & \text{3.91E-18} & -0.17 & 0.17 \\
0 & 0 & 0 & 0 & 0 & 0 & 0 & \text{4.13E-17} & \text{4.13E-17} & \text{4.13E-17} & 0 & 0.17 & -0.5
\end{bmatrix}$$

After plugging in the various parameters and computing the eigenvalues using MATLAB the following nine eigenvalues emerge and thus the equilibrium is unstable:

$$-0.3999, -0.07946, -0.0001399, -1.724, -0.572, -0.098, -0.096, 0.322, 0.542$$

Section 6.2

Disease-Free Equilibrium - Full Model

As per section 6.0.1, the following variables are zero at equilibrium:

$$G_1, S, G_2, Q, N, A_H, M_Q, M_{G1}, M_S, M_{G_2}$$

Thus, the only remaining variables to evaluate are T, R, V, L_1, and $L2$. It has been determined that $L_1^* = L_2^*$.

TNF-α:

$$\begin{aligned} \frac{dT}{dt} = 0 &= jN - k(v_0 + V)T \\ 0 &= 0 - k(v_0 + V)T \\ 0 &= T^* \end{aligned} \tag{6.5}$$

VEGF:

$$\begin{aligned} \frac{dR}{dt} = 0 &= -q_R(v_0 + V)R \\ 0 &= R^* \end{aligned} \tag{6.6}$$

Normoxic Region Acid (L_2):

$$\begin{aligned} \frac{dL_2}{dt} = 0 &= -l(L_2 - L_1) + q(3.9810717 \times 10^{-14} - L_2)(V + v_1) \\ 0 &= 0 + q(3.9810717 \times 10^{-14} - L_2)(V + v_1) \\ L_2^* &= L_1^* = 3.9810717 \times 10^{-14} \end{aligned} \tag{6.7}$$

Vasculature:

$$\begin{aligned} \frac{dV}{dt} = 0 &= (1 - D_V)c_v \frac{R(v_0 + V)}{s_v + R + v_0 + V} - D_V V \\ 0 &= 0 - D_V V \\ 0 &= 0 \cdot V \end{aligned} \tag{6.8}$$

The Jacobian for the disease-free equilibrium can be seen on the next page. Note that the order of the equations was changed prior to the calculation of the Jacobian to make the block triangular matrix easier to analyze.

	$\frac{\partial}{\partial G_1}$	$\frac{\partial}{\partial S}$	$\frac{\partial}{\partial G_2}$	$\frac{\partial}{\partial Q}$	$\frac{\partial}{\partial N}$	$\frac{\partial}{\partial T}$	$\frac{\partial}{\partial A_H}$	$\frac{\partial}{\partial R}$	$\frac{\partial}{\partial V}$	$\frac{\partial}{\partial M_Q}$	$\frac{\partial}{\partial M_1}$	$\frac{\partial}{\partial M_S}$	$\frac{\partial}{\partial M_2}$	$\frac{\partial}{\partial L_1}$	$\frac{\partial}{\partial L_2}$
$\frac{dG_1}{dt}$	$-c_1$	0	$2c_2$	0	0	0	0	0	0	0	0	0	0	0	0
$\frac{dS}{dt}$	c_1B	$-c_s$	0	C	0	0	0	0	0	0	0	0	0	0	0
$\frac{dG_2}{dt}$	0	c_s	$-c_2-d_a$	0	0	0	0	0	0	0	0	0	0	0	0
$\frac{dQ}{dt}$	$c_1(1-B)$	0	0	$-eH-C$	0	0	0	0	0	0	0	0	0	0	0
$\frac{dN}{dt}$	0	0	0	eH	$-m(V+v_0)$	0	0	$-q_R(V+v_0)$	0	c_qv	0	0	0	$-l$	l
$\frac{dT}{dt}$	0	0	0	0	j	$-k(V+v_0)$	0	$\frac{c_v(V+v_0)}{V+s_v+v_0}$	0	0	0	0	0	l	$-l-q(v_1+V)$
$\frac{dA_H}{dt}$	0	0	0	0	0	0	$c_{ga}-m_h$		0	0	0	0	0		
$\frac{dR}{dt}$	0	0	0	c_qv	0	0	c_qv	0	0	c_qv	0	0	0	0	0
$\frac{dV}{dt}$	0	0	0	0	0	0	0	0	0	0	0	0	0	0	0
$\frac{dA_H}{dt}$	0	0	0	0	0	0	m_h	0	0	$-C_M$	$k_1(1-B_M)$	0	0	0	0
$\frac{dM_1}{dt}$	0	0	0	0	0	0	0	0	0	0	$-k_1$	0	$2k_2$	0	0
$\frac{dM_S}{dt}$	0	0	0	0	0	0	0	0	0	C_M	k_1B_M	$-k_s$	0	0	0
$\frac{dM_2}{dt}$	0	0	0	0	0	0	0	0	0	0	0	k_s	$-k_2-d_a$	0	0
$\frac{dL_1}{dt}$	0	0	0	0	0	0	x_h	0	0	x_h	0	0	0	$-l$	l
$\frac{dL_2}{dt}$	0	0	0	0	0	0	0	0	0	0	x_m	x_m	x_m	l	$-l-q(v_1+V)$

6.2.1. Model Stability

This section serves to show that it is not possible to define parameter conditions under which the disease-free equilibrium in the *in vivo* model is guaranteed to be stable where all parameters are assumed strictly positive. As in the acidotic spheroid model, the Jacobian for the full model disease-free equilibrium is a lower block triangular matrix. Thus, from "Mathematical Tools for Data Mining: Set Theory, Partial Orders, Combinatorics", it is again true that the spectrum for the matrix is the same as the union of the spectra of its partitioned blocks. Thus, as in section 6.1.1, the Jacobian is partitioned into blocks as marked in the Jacobian.

Block A_{11}. The first block is most readily analyzed using Gerschgorin's circle theorem as the eigenvalues of a matrix must lie within the union of disks in the complex plane defined for each row as being centered on the diagonal element of the matrix with a radius equal to the sum of the off-diagonal elements. Except for the element entered in the fourth row, fourth column of the block, this block is identical to Block A_{11} as described in section 6.1.1 for the spheroid. As such, the work to determine the criteria of the first disks will not be reproduced here but the criteria are listed.

(a) **Disk 1** ($i = 1$): Always negative where $c_1 > 2c_2$.

(b) **Disk 2** ($i = 2$): Always negative where:

$$c_s > c_1 \frac{v_0 + V^*}{s_1 + v_0 + V^*} + c_q \frac{v_0 + V^*}{s_q + v_0 + V^*}$$

It should be noted however that both $\frac{v_0+V^*}{s_1+v_0+V^*}$ and $\frac{v_0+V^*}{s_1+v_0+V^*}$ are necessarily less than one as the denominators are the sum of the numerator and another

positive number. Thus, the above criterion for which the disk must be negative can be simplified to the following, especially where v_0 is small and vasculature is low

$$c_s > c_1 + c_q$$

(c) **Disk 3** ($i = 3$): Always negative where $c_2 + d_a > c_s$

(d) **Disk 4** ($i = 4$): $R_4 = c_1(1 - B)$

The real parts of the eigenvalues bounded within disk 4 can range from

$$-eH - C - c_1(1 - B) \text{ to } -eH - C + c_1(1 - B)$$

The ranges can be rewritten as

$$-e - c_q \frac{v_0 + c_{qs}V^*}{s_q + v_0 + c_{qs}V^*} - c_1\Big(1 - \frac{v_0 + V^*}{s_1 + v_0 + V^*}\Big)$$

to

$$-e - c_q \frac{v_0 + c_{qs}V^*}{s_q + v_0 + c_{qs}V^*} + c_1\Big(1 - \frac{v_0 + V^*}{s_1 + v_0 + V^*}\Big)$$

All of the real parts of this disk are negative where

$$e + c_q \frac{v_0 + c_{qs}V^*}{s_q + v_0 + c_{qs}V^*} + c_1 \frac{v_0 + V^*}{s_1 + v_0 + V^*} > c_1$$

As in the analysis of the spheroid, the Gerschgorin Disks for the four columns of the block are also evaluated by the same work as section 6.1.1; the only disk that differs is disk 4, so the results of disks 1-3 are simply reproduced here from the previous

section:

(a) **Disk 1** ($j = 1$): This will always be negative.

(b) **Disk 2** ($j = 2$): This disk is always negative.

(c) **Disk 3** ($j = 3$): This disk is always negative if $d_a > c_2$.

(d) **Disk 4** ($j = 4$): $C_4 = C + eH$

The fourth disk ranges from $-2eH - 2C$ to 0. This disk is always negative.

Block A_{22}. Block A_{22} is a lower triangular matrix so its eigenvalues can be read off the diagonal and the eigenvalues are thus $-m(V+v_0)$, $-k(V+v_0)$, and $c_{ga}-m_h$. The first two eigenvalues are always negative because the parameters and compartments are taken to be positive and the third is negative where $m_h > c_{ga}$.

Block A_{33}. The third block is again analyzed by the Gerschgorin Circle Theorem, first in its rows and then in the columns:

$$A_{33} = \begin{bmatrix} -q_R(V+v_0) & 0 & c_{qv} & 0 & 0 & 0 \\ \frac{c_v(V+v_0)}{V+s_v+v_0} & 0 & 0 & 0 & 0 & 0 \\ 0 & 0 & -C_M & k_1(1-B_M) & 0 & 0 \\ 0 & 0 & 0 & -k_1 & 0 & 2k_2 \\ 0 & 0 & C_M & k_1 B_M & -k_s & 0 \\ 0 & 0 & 0 & 0 & k_s & -k_2 - d_a \end{bmatrix}$$

(a) **Disk 1** ($i = 1$): $R_1 = c_{qv}$

The real values of this disk can range from $-q_R(V+v_0)-c_{qv}$ to $-q_R(V+v_0)+c_{qv}$ and it is thus always negative where $q_R(V + v_0) > c_{qv}$.

(b) **Disk 2** ($i = 2$): $R_2 = \frac{c_v(V+v_0)}{V+s_v+v_0}$

The diagonal element corresponding to disk 2 is zero; unless $\frac{c_v(V+v_0)}{V+s_v+v_0}$ is zero which is not possible under the assumption that the parameters are strictly positive, it is not possible to guarantee that the disk is always negative.

(c) **Disk 3** ($i = 3$): $R_3 = k_1(1 - B_M)$

This disk can range from $-C_M - k_1(1 - B_M)$ to $-C_M + k_1(1 - B_M)$. The disk is always negative when $C_M > k_1(1 - B_M)$.

(d) **Disk 4** ($i = 4$): $R_4 = 2k_2$

Disk 4 ranges from $-k_1-2k_2$ to $-k_1+2k_2$ and is thus always negative if $k_1 > 2k_2$.

(e) **Disk 5** ($i = 5$): $R_5 = C_M + k_1B_M$

Disk 5 ranges from $-k_S - C_M - k_1B_M$ to $-k_S + C_M + k_1B_M$ and is thus always negative when $k_S > C_M + k_1B_M$

(f) **Disk 6** ($i = 6$): $R_6 = k_s$

The real values of Disk 6 range from $-k_2 - d_a - k_s$ to $-k_2 - d_a + k_s$ and is always negative when $k_2 + d_a > k_s$.

Disk 2 from the rows of this block makes it impossible to establish criteria in which the eigenvalues are guaranteed to be negative. As such, the columns will be considered in the corollary to Gerschgorin's Circle Theorem.

(a) **Disk 1** ($j = 1$): $C_1 = \frac{c_v(V+v_0)}{V+s_v+v_0}$

Disk 1 ranges from $-q_R(V^* + v_0) - \frac{c_v(V+v_0)}{V+s_v+v_0}$ to $-q_R(V^* + v_0) + \frac{c_v(V+v_0)}{V+s_v+v_0}$. The real parts of this disk are always negative when $q_R(V^* + v_0) > \frac{c_v(V+v_0)}{V+s_v+v_0}$

(b) **Disk 2** ($j = 2$): $C_2 = 0$

This disk suggests that one of the eigenvalues is zero as the column is all zeros.

(c) **Disk 3** ($j = 3$): $C_3 = C_M + c_{qv}$

This disk can range from $-2C_M - c_{qv}$ to c_{qv} and it is thus not possible to guarantee that this disk is always negative.

(d) **Disk 4** ($j = 4$): $C_4 = k_1$

Disk 4 ranges from $-2k_1$ to 0 and is thus always negative.

(e) **Disk 5** ($j = 5$): $C_5 = k_s$

Disk 5 ranges from $-2k_s$ to 0 and is thus always negative.

(f) **Disk 6** ($j = 6$): $C_6 = 2k_2$

Disk 6 ranges from $-3k_2 - d_a$ to $k_2 - d_a$ and is always negative if $d_a > k_2$.

There are no conditions under which the union of the Gerschgorin Disks associated with Block A_{33} have strictly negative real parts and it is thus not possible to establish conditions that guarantee that all eigenvalues in this matrix are negative.

Block A_{44}. The determinant of this 2×2 block is determined as follows:

$$
\begin{aligned}
det(A_{44} - \lambda I) &= \begin{vmatrix} -l-\lambda & l \\ l & -l-q(v_1+V)-\lambda \end{vmatrix} \\
&= (-l-\lambda)(-l-q(v_1+V)-\lambda) - l^2 \\
&= l^2 + lq(v_1+V) + l\lambda + l\lambda + q(v_1+V)\lambda + \lambda^2 - l^2 \\
&= \lambda^2 + (2l + q(v_1+V))\lambda + lq(v_1+V)
\end{aligned}
$$

From the quadratic formula, the eigenvalues for this block are thus:

$$
\begin{aligned}
\lambda &= \frac{-(2l+q(v_1+V)) \pm \sqrt{(2l+q(v_1+V))^2 - 4lq(v_1+V)}}{2} \\
&= \frac{-(2l+q(v_1+V)) \pm \sqrt{4l^2 + 4lq(v_1+V) + q^2(v_1+V)^2 - 4lq(v_1+V)}}{2} \\
&= \frac{-(2l+q(v_1+V)) \pm \sqrt{4l^2 + q^2(v_1+V)^2}}{2}
\end{aligned}
$$

As with the spheroid, when the square root term in the numerator is subtracted then the eigenvalue must be negative because all of the compartments and parameters are defined to be non-negative. When the term is added, the following inequality is obtained, therefore indicating that the numerator (and thus the eigenvalue) is always negative:

$$
\begin{aligned}
(2l+q(v_1+V)) &> \sqrt{(2l+q(v_1+V))^2 - 4lq(v_1+V)} \\
(2l+q(v_1+V))^2 &> (2l+q(v_1+V))^2 - 4lq(v_1+V) \\
4lq(v_1+V) &> (2l+q(v_1+V))^2 - (2l+q(v_1+V))^2 \\
4lq(v_1+V) &> 0
\end{aligned}
$$

Both eigenvalues associated with block A_{44} will always be negative since the parameters and vasculature are assumed to be positive.

Block A_{22} makes it impossible to set criteria under which this equilibrium will always be stable using Gerschgorin's circle theorem. It will always be possible for positive eigenvalues to exist when all parameters in this model are assumed positive.

6.2.2. Substituted Parameters

Because V^* can be any number in this equilibrium, it is set to zero for simplicity. The eigenvalues obtained using MATLAB from the following matrix are as follows, indicating that the equilibrium is unstable:

$$-0.00743, -0.422, 0, -266.5, 0.8009492, -6.306283 + 3.150423i, -6.306283 - 3.150423i,$$

$$-5.084582, -1.801961, -22.19804, -6.513404 + 3.160107i, -6.513404 - 3.160107i,$$

$$0.7024726, -0.05326382, -0.099998$$

$$
\begin{bmatrix}
-1.9618 & 0 & 14.304 & 0 & 0 & 0 & 0 & 0 & 0 & 0 & 0 & 0 & 0 & 0 & 0 \\
1.771 & -3.2204 & 0 & 4.135 & 0 & 0 & 0 & 0 & 0 & 0 & 0 & 0 & 0 & 0 & 0 \\
0 & 3.2204 & -7.152 & 0 & 0 & 0 & 0 & 0 & 0 & 0 & 0 & 0 & 0 & 0 & 0 \\
0.1908 & 0 & 0 & -4.562 & 0 & 0 & 0 & 0 & 0 & 0 & 0 & 0 & 0 & 0 & 0 \\
0 & 0 & 0 & 0.427 & -0.422 & 0 & 0 & 0 & 0 & 0 & 0 & 0 & 0 & 0 & 0 \\
0 & 0 & 0 & 0 & 0.543 & -0.00743 & 0 & 0 & 0 & 0 & 0 & 0 & 0 & 0 & 0 \\
0 & 0 & 0 & 0 & 0 & 0 & -0.099998 & 0 & 0 & 0 & 0 & 0 & 0 & 0 & 0 \\
0 & 0 & 0 & 85 & 0 & 0 & 85 & -266.5 & 0 & 85 & 0 & 0 & 0 & 0 & 0 \\
0 & 0 & 0 & 0 & 0 & 0 & 0 & 2.37E-6 & 0 & 0 & 0 & 0 & 0 & 0 & 0 \\
0 & 0 & 0 & 0 & 0 & 0 & 0.1 & 0 & 0 & -0.0434 & 0.1908 & 0 & 0 & 0 & 0 \\
0 & 0 & 0 & 0 & 0 & 0 & 0 & 0 & 0 & 0 & -1.9618 & 0 & 14.304 & 0 & 0 \\
0 & 0 & 0 & 0 & 0 & 0 & 0 & 0 & 0 & 0.0434 & 1.771 & -3.2204 & 0 & 0 & 0 \\
0 & 0 & 0 & 0 & 0 & 0 & 0 & 0 & 0 & 0 & 0 & 3.2204 & -7.152 & 0 & 0 \\
0 & 0 & 0 & 8.8E-18 & 0 & 0 & 8.8E-18 & 0 & 0 & 8.8E-18 & 0 & 0 & 0 & -10 & 10 \\
0 & 0 & 0 & 0 & 0 & 0 & 0 & 0 & 0 & 0 & 8E-18 & 8E-18 & 8E-18 & 10 & -14
\end{bmatrix}
$$

Chapter 7

Numerical Methods

All of the simulations in this thesis were carried out in MATLAB; the simulations for the monolayer, spheroid, and acidotic spheroid were solved using ode45 and the those for the *in vivo* model were solved using ode23s. Additional functions included GRABIT to acquire data from paper figures and lhsdesign to develop the Latin hypercube matrix. The methods employed to develop the genetic algorithm used here for parameter optimization are described below.

Section 7.1

Genetic Algorithm

After hand fitting the model parameters to best fit the data, a custom genetic algorithm was employed to optimize the parameter values. Genetic algorithms are a means of optimization that resemble biological evolution. For this algorithm, a hand fit is first carried out with parameters restricted to biologically feasible values to provide the algorithm with a starting point. Next, the parameter ranges are established by setting maximum and minimum values to each parameter that is allowed to vary,

as one order of magnitude smaller and one order of magnitude larger than the hand fit value. An individual is defined as a given parameter vector. Next, a matrix of n individuals where $n \mod 4 = 0$ is initialized by setting individual 1 to the hand-fit vector and randomly selecting parameters from within the previously established range for every parameter for the remaining $n - 1$ individuals.

After generating a matrix of individuals, each individual is fed as a parameter vector into the differential equation solver, ode45. Vectors containing data from the biological literature as well as the resultant curves from the ode solver are then evaluated using a custom fitness function. The function is used to compute a value for relative mean squared error (rMSE) as follows:

$$\begin{aligned} rMSE_j &= \sum_{i=1}^{a} \left(\frac{x(t_i) - d(t_i)}{d(t_i)} \right)^2 \\ rMSE_{tot} &= \sum_{j=1}^{b} rMSE_j \end{aligned} \tag{7.1}$$

where $x(t_i)$ is the model value at a given time point, $d(t_i)$ is the data point at the same time, and i ranges from 1 to the number of data points available (a). Relative mean squared error is computed for each of the model curves for which data is available and the total rMSE ($rMSE_{tot}$) is calculated as the sum of these errors such that j ranges from 1 to the number of data sets, b.

Next, the first $n/2$ individuals of the fitness matrix are determined by a tournament style competition of the original set of n individuals. Individuals are randomly paired and the individual with the lowest rMSE is selected for the fitness matrix where their parameter values and rMSE is stored. The $n/2$ best individuals from the random pairings are then permitted to "reproduce" which accounts for the following

$n/4$ individuals. Reproduction is simulated by again randomly pairing the individuals in the fitness matrix to form the "parents" and then randomly selecting parent parameter values from each of their vectors of parameters, thereby generating offspring with different combinations of preexisting parameters. The offspring are added as the $n/2+1$ to the $3n/4$ individuals of the fitness matrix. Finally, $n/4$ individuals are randomly selected from the first $n/2$ fitness matrix individuals and develop "mutations" by randomly increasing or decreasing a random parameter by an amount between 0 and 100%; the mutated parameters values are constrained by the initially assigned parameter ranges.

This process constitutes one "generation". The algorithm is permitted to run until the rMSE stabilizes and at least 25 generations have passed with no change in rMSE. This 25 generations of stability is arbitrary but the fit with the algorithm is considerably more accurate than a hand fit and negligible changes in fit based on very small shifts in parameter values are not of interest at this time.

MATLAB code for the algorithm's functions as applied to the spheroid can be found in Appendix 4. The code was modified to accommodate additional equations and parameters for the acidotic spheroid and *in vivo* fit but is in essence the same.

Bibliography

[1] Anderson, Michael, et al. "Probe for the Measurement of Cell Surface PH in Vivo and Ex Vivo." *Proceedings of the National Academy of Sciences*, vol. 113, no. 29, 2016, pp. 8177–8181., doi:10.1073/pnas.1608247113.

[2] Astigiano, Simonetta, et al. Systemic Alkalinisation Delays Prostate Cancer Cell Progression in TRAMP Mice. *Journal of Enzyme Inhibition and Medicinal Chemistry*, vol. 32, no. 1, 2017, pp. 363-368., doi:10.1080/14756366.2016.1252760.

[3] Ibrahim-Hashim, Arig, et al. Systemic Buffers Inhibit Carcinogenesis in TRAMP Mice. *Journal of Urology*, vol. 188, no. 2, 2012, pp. 624–631., doi:10.1016/j.juro.2012.03.113.

[4] Gatenby, Robert A., and Robert J. Gillies. "Why Do Cancers Have High Aerobic Glycolysis?" *Nature Reviews Cancer*, vol. 4, no. 11, 2004, pp. 891–899., doi:10.1038/nrc1478.

[5] Gillies, Robert J., and Robert A. Gatenby. "Metabolism and Its Sequelae in Cancer Evolution and Therapy." *The Cancer Journal*, vol. 21, no. 2, 2015, pp. 88–96., doi:10.1097/ppo.0000000000000102.

[6] Damaghi, Mehdi, and Robert Gillies. Phenotypic Changes of Acid-Adapted Cancer Cells Push Them toward Aggressiveness in Their Evolution in the Tumor Microenvironment. *Cell Cycle*, vol. 16, no. 19, 2016, pp. 1739-1743., doi:10.1080/15384101.2016.1231284.

[7] Fang, Jennifer S., et al. Adaptation to Hypoxia and Acidosis in Carcinogenesis and Tumor Progression. *Seminars in Cancer Biology*, vol. 18, no. 5, 2008, pp. 330-337., doi:10.1016/j.semcancer.2008.03.011.

[8] Gasnier, Anne, and Nassim Parvizi. "Updates on the Diagnosis and Treatment of Prostate Cancer." *The British Journal of Radiology*, vol. 90, no. 1075, 2017, p. 20170180., doi:10.1259/bjr.20170180.

[9] Hamilton, W, et al. "Clinical Features of Colorectal Cancer before Diagnosis: a Population-Based Case–Control Study." *British Journal of Cancer*, vol. 93, no. 4, 2005, pp. 399–405., doi:10.1038/sj.bjc.6602714.

[10] Damodaran, Shivashankar, et al. "Newly Diagnosed Metastatic Prostate Cancer: Has the Paradigm Changed?" *Urologic Clinics of North America*, vol. 44, no. 4, 2017, pp. 611–621., doi:10.1016/j.ucl.2017.07.008.

[11] Chen, Fang-Zhi, and Xiao-Kun Zhao. "Prostate Cancer: Current Treatment and Prevention Strategies." Iranian Red Crescent Medical Journal, vol. 15, no. 4, 2013, pp. 279–284., doi:10.5812/ircmj.6499.

[12] He, Yixuan, et al. Predictive Modeling of Neuroblastoma Growth Dynamics in Xenograft Model After Bevacizumab Anti-VEGF Therapy. *Bulletin of Mathe-*

matical Biology, vol. 80, no. 8, 2018, pp. 2026-2048., doi:10.1007/s11538-018-0441-3.

[13] Nath, Sritama, and Gayathri R. Devi. "Three-Dimensional Culture Systems in Cancer Research: Focus on Tumor Spheroid Model." *Pharmacology & Therapeutics*, vol. 163, 2016, pp. 94–108., doi:10.1016/j.pharmthera.2016.03.013.

[14] Hirschhaeuser, Franziska, et al. "Multicellular Tumor Spheroids: An Underestimated Tool Is Catching up Again." *Journal of Biotechnology*, vol. 148, no. 1, 2010, pp. 3–15., doi:10.1016/j.jbiotec.2010.01.012.

[15] Ortmann, Brian, et al. "Cell Cycle Progression in Response to Oxygen Levels." *Cellular and Molecular Life Sciences*, vol. 71, no. 18, 2014, pp. 3569–3582., doi:10.1007/s00018-014-1645-9.

[16] Tang, Lei, et al. "Computational Modeling of 3D Tumor Growth and Angiogenesis for Chemotherapy Evaluation." *PLoS ONE*, vol. 9, no. 1, 2014, doi:10.1371/journal.pone.0083962.

[17] Itakura, Jun, et al. "Concomitant over-Expression of Vascular Endothelial Growth Factor and Its Receptors in Pancreatic Cancer." *International Journal of Cancer*, vol. 85, no. 1, 2000, pp. 27–34., doi:10.1002/(sici)1097-0215(20000101)85:13.0.co;2-8.

[18] Roberts, Emma, et al. "The Role of Vascular Endothelial Growth Factor in Metastatic Prostate Cancer to the Skeleton." *Prostate Cancer*, vol. 2013, 2013, pp. 1–8., doi:10.1155/2013/418340.

[19] Faes, Seraina, et al. "Acidic PH Reduces VEGF-Mediated Endothelial Cell Responses by Downregulation of VEGFR-2; Relevance for Anti-Angiogenic Therapies." *Oncotarget*, vol. 7, no. 52, 2016, pp. 86026–86038., doi:10.18632/oncotarget.13323.

[20] Wallace, Dorothy I., and Xinyue Guo. "Properties of Tumor Spheroid Growth Exhibited by Simple Mathematical Models." Frontiers in Oncology, vol. 3, 2013, doi:10.3389/fonc.2013.00051.

[21] Wang, Xia, and Yong Lin. "Tumor Necrosis Factor and Cancer, Buddies or Foes?" Acta Pharmacologica Sinica, vol. 29, no. 11, 2008, pp. 1275–1288., doi:10.1111/j.1745-7254.2008.00889.x.

[22] Nabors, L. Burt, et al. "Tumor Necrosis Factor Alpha Induces Angiogenic Factor Up-Regulation in Malignant Glioma Cells: A Role for RNA Stabilization and HuR." *Cancer Res.*, vol. 63, no. 14, 2003, pp. 4181-4187.

[23] Heiden, M. G. Vander, et al. "Understanding the Warburg Effect: The Metabolic Requirements of Cell Proliferation." *Science*, vol. 324, no. 5930, 2009, pp. 1029–1033., doi:10.1126/science.1160809.

[24] Warburg, O. "On the Origin of Cancer Cells." *Science*, vol. 123, no. 3191, 1956, pp. 309–314., doi:10.1126/science.123.3191.309.

[25] Greenberg, N. M., et al. "Prostate Cancer in a Transgenic Mouse." *Proceedings of the National Academy of Sciences*, vol. 92, no. 8, 1995, pp. 3439–3443., doi:10.1073/pnas.92.8.3439.

[26] Huss, Wendy J, et al. "Autochthonous Mouse Models for Prostate Cancer: Past, Present and Future." Seminars in Cancer Biology, vol. 11, no. 3, 2001, pp. 245–259., doi:10.1006/scbi.2001.0373.

[27] Alizadeh, M., and S. Alizadeh. "Survey of Clinical and Pathological Characteristics and Outcomes of Patients With Prostate Cancer." *Global Journal of Health Science*, vol. 6, no. 7, 2014, doi:10.5539/gjhs.v6n7p49.

[28] Ibrahim-Hashim, Arig, et al. "Defining Cancer Subpopulations by Adaptive Strategies Rather Than Molecular Properties Provides Novel Insights into Intratumoral Evolution." *Cancer Research*, vol. 77, no. 9, 2017, pp. 2242–2254., doi:10.1158/0008-5472.can-16-2844.

[29] Robertson-Tessi, M., et al. "Impact of Metabolic Heterogeneity on Tumor Growth, Invasion, and Treatment Outcomes." *Cancer Research*, vol. 75, no. 8, 2015, pp. 1567–1579., doi:10.1158/0008-5472.can-14-1428.

[30] Ballangrud, Ase M, et al. Characterization of LNCaP Prostate Cancer Cell Spheroids. *Clinical Cancer Research*, vol. 5, Oct. 1999, pp. 3171-3176.

[31] Ghosh, Paramita M, et al. Role of RhoA Activation in the Growth and Morphology of a Murine Prostate Tumor Cell Line. *Oncogene*, vol. 18, no. 28, 1999, pp. 4120-4130., doi:10.1038/sj.onc.1202792.

[32] Wallace, Dorothy I., et al. "A Model for Spheroid versus Monolayer Response of SK-N-SH Neuroblastoma Cells to Treatment with 15-Deoxy-PGJ2." *Computational and Mathematical Methods in Medicine*, vol. 2016, 2016, pp. 1–11., doi:10.1155/2016/3628124.

[33] Alvarez-Pérez, Jose, et al. "Microscopic Images of Intraspheroidal PH by 1H Magnetic Resonance Chemical Shift Imaging of PH Sensitive Indicators." *Magnetic Resonance Materials in Physics, Biology and Medicine*, vol. 18, no. 6, 2005, pp. 293–301., doi:10.1007/s10334-005-0013-z.

[34] Griffiths, Jr. "Are Cancer Cells Acidic?" *British Journal of Cancer*, vol. 64, no. 3, 1991, pp. 425–427., doi:10.1038/bjc.1991.326.

[35] Ippolito, Joseph E., et al. "Extracellular PH Modulates Neuroendocrine Prostate Cancer Cell Metabolism and Susceptibility to the Mitochondrial Inhibitor Niclosamide." *Plos One*, vol. 11, no. 7, 2016, doi:10.1371/journal.pone.0159675.

[36] Sun, Huiyan, et al. "Warburg Effects in Cancer and Normal Proliferating Cells: Two Tales of the Same Name." *Genomics, Proteomics & Bioinformatics*, vol. 17, no. 3, 2019, pp. 273–286., doi:10.1016/j.gpb.2018.12.006.

[37] National Center for Biotechnology Information. PubChem Database. Sodium bicarbonate, CID=516892, https://pubchem.ncbi.nlm.nih.gov/compound/Sodium-bicarbonate (accessed on May 14, 2020)

[38] "7.4 Spectra of Special Matrices." Mathematical Tools for Data Mining: Set Theory, Partial Orders, Combinatorics, by Dan A. Simovici and Chabane Djeraba, Springer, 2014, pp. 357–358.

[39] MATLAB and Statistics Toolbox Release 2018a, The MathWorks, Inc., Natick, Massachusetts, United States.

[40] S. Gersgorin (S. Gerschgorin), "Uber die Abgrenzung der Eigenwerte einer Matrix", Bulletin de l'Académie des Sciences de l'URSS. Classe des sciences mathematiques et na, 1931, no. 6, 749–754

Appendix I

Spheroid Parametrization Without Acid

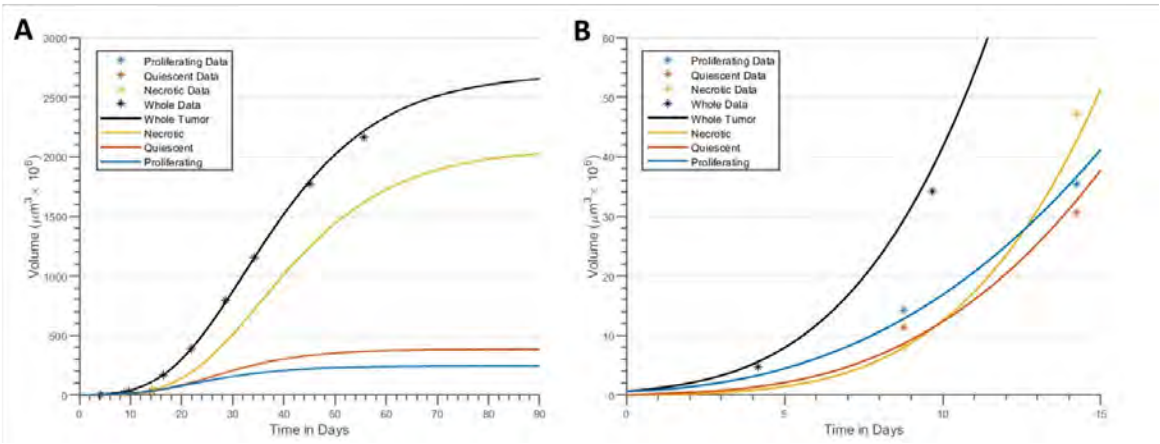

Figure 7.1: Panel A represents the long-term fit of the whole tumor volume to the values for tumor volume described in Table 1. Additionally, panel A qualitatively shows the volume of each compartment and the volume of the entire spheroid reaching a constant volume over a long period of time, as anticipated. Panel B shows the fit of the model to the regional spheroid volumes described in Table A2-2 in the short term.

In Vivo Parametrization Without Acid

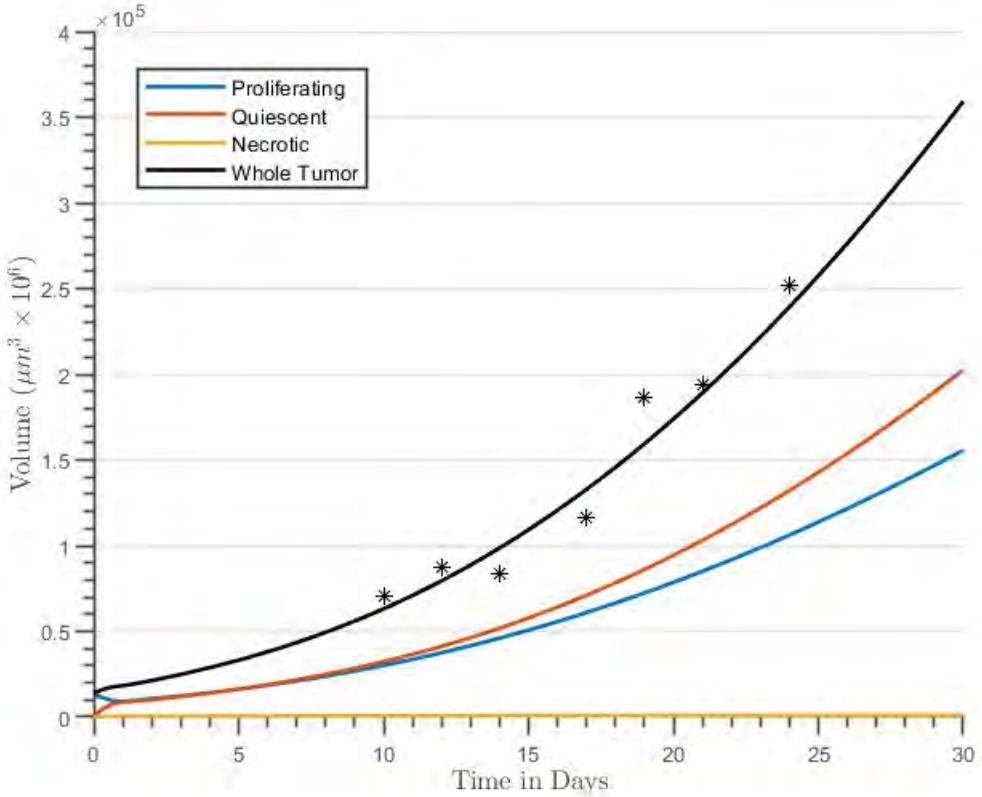

Figure 7.2: Fit of the data from Astigiano et al. as observed in Table A2-3 using the *in vivo* tumor parameters seen in Table A1-1.

Table of Parameters for the Base Model (No Acid)

Table A1-1: *In vivo* Parameters		
Parameter	Value	Explanation
d_a	0	Natural Death Rate
c_1	1.961763658	G_1 to S Transition
c_s	3.220357473	S to G_2 Transition
c_2	7.151991545	G_2 to G_1 Transition
v_0	14.8629058785908	Available Nutrients
j	0.542510626458240	TNF-α Production
k	0.0005	TNF-α Removal
s_1	1.60067459244845	Describes B
s_q	258.628255950016	Describes C
e	0.427326531579406	Q Necrosis
m	0.0283884658509696	Removal of Necrosis
s_n	534.453837615470	Describes F
c_q	76.1888838144399	Describes C
c_f	0.01	TNF-α Induced Death (P)
c_v	0.861901279053398	Angiogenesis
c_R	6	VEGF Production by P
s_R	5000	VEGF Stimulation by TNF-α
q_R	17.9354396208518	VEGF Removal
c_{qv}	50	VEGF Production by Q
c_{qs}	0.373345804060691	Describes C
s_v	343.170179716681	Describes Vasculature
s_h	100	Describes H
f_h	1.25635942479245	Describes H
g_h	0.01	Describes H

Appendix II

This appendix is comprised of tabulated data either taken directly from the literature using the MATLAB function GRABIT or processed from articles as described in the body of the thesis.

Table A2-1: Spheroid Data (Ballangrud et al.)		
day	volume (μm^3)	radius (μm)
0	0.6×10^6	52.3223868
4.155	4.7221×10^6	104.075584
9.686	3.424×10^7	201.441238
16.36	1.668×10^8	341.483045
21.82	3.916×10^8	453.855941
28.62	7.921×10^8	573.980495
34.15	1.152×10^9	650.311284
45	1.770×10^9	
55.57	2.165×10^9	

Table A2-2: Spheroid Compartment Data (Ballangrud et al.)				
Day	Radius (μm)	Necrotic (μm)	Quiescent (μm)	Proliferative (μm)
8.7660	200	124	42.3971	33.6029
14.2323	300	224	40.7414	35.2586

Table A2-3: Whole In Vivo Data (Astigiano et al.)			
day	adjusted day	volume (μm^3)	radius (μm)
10	24.08642	70947905659	2568.13
12	26.08642	87083211548	2749.679
14	28.08642	84041189828	2717.281
17	31.08642	$1.16697 \times 10^1 1$	3031.5
19	33.08642	$1.86121 \times 10^1 1$	3541.894
21	35.08642	$1.93735 \times 10^1 1$	3589.548
24	38.08642	$2.51437 \times 10^1 1$	3915.435

Appendix III

This appendix consists of the partial derivatives associated with the Jacobians for the spheroid model with acidosis and for the full *in vivo* model with acidosis.

Spheroid Partials

Acidotic Spheroid: Partial Derivatives (a)			
	$\frac{\partial}{\partial G_1}$	$\frac{\partial}{\partial S}$	$\frac{\partial}{\partial G_2}$
$\frac{dG_1}{dt}$	$-c_1 - c_f F - D_2$	0	$2c_2$
$\frac{dS}{dt}$	$c_1 B\left[1 - \frac{G_1}{s_1+G_1+v_0}\right] - \frac{CQ}{s_q+P+v_0}$	$-c_s - \frac{CQ}{s_q+P+v_0} - c_f F - D_2$	$-\frac{CQ}{s_q+P+v_0}$
$\frac{dG_2}{dt}$	0	c_s	$-c_2 - d_a - c_f F - D_2$
$\frac{dQ}{dt}$	$c_1\left[1 - B + \frac{BG_1}{s_1+G_1+v_0}\right] + \frac{CQ}{s_q+P+v_0}$	$\frac{CQ}{s_q+P+v_0}$	$\frac{CQ}{s_q+P+v_0}$
$\frac{dN}{dt}$	D_2	D_2	D_2
$\frac{dT}{dt}$	0	0	0
$\frac{dA_H}{dt}$	0	0	0
$\frac{dM_{G1}}{dt}$	0	0	0
$\frac{dM_S}{dt}$	0	0	0
$\frac{dM_{G2}}{dt}$	0	0	0
$\frac{dM_Q}{dt}$	0	0	0
$\frac{dL_1}{dt}$	0	0	0
$\frac{dL_2}{dt}$	0	0	0

Acidotic Spheroid: Partial Derivatives (b)					
	$\frac{\partial}{\partial Q}$	$\frac{\partial}{\partial N}$	$\frac{\partial}{\partial T}$	$\frac{\partial}{\partial A_H}$	$\frac{\partial}{\partial M_{G1}}$
$\frac{dG_1}{dt}$	0	0	$-\frac{c_f s_n}{(s_n+T)^2} G_1$	0	0
$\frac{dS}{dt}$	C	0	$-\frac{c_f s_n}{(s_n+T)^2} S$	0	0
$\frac{dG_2}{dt}$	0	0	$-\frac{c_f s_n}{(s_n+T)^2} G_2$	0	0
$\frac{dQ}{dt}$	$-C - D_1 - a_h - eH$	0	0	0	0
$\frac{dN}{dt}$	$D_1 + eH$	$-mv_0$	0	D_3	D_4
$\frac{dT}{dt}$	0	j	$-kv_0$	0	0
$\frac{dA_H}{dt}$	$a_h q_3$	0	0	$c_{ga} - m_h - D_3$	0
$\frac{dM_{G1}}{dt}$	0	0	$-\frac{k_f s_n}{(s_n+T)^2} M_{G1}$	0	$-k_1 - k_f F - D_4$
$\frac{dM_S}{dt}$	0	0	$-\frac{k_f s_n}{(s_n+T)^2} M_S$	0	$k_1 B_M \left[1 - \frac{M_{G1}}{s_1+M_{G1}+v_0}\right] - \frac{C_M M_Q}{s_q+M+v_0}$
$\frac{dM_{G2}}{dt}$	0	0	$-\frac{k_f s_n}{(s_n+T)^2} M_{G2}$	0	0
$\frac{dM_Q}{dt}$	0	0	0	m_h	$k_1 \left[1 - B_M + \frac{M_{G1}}{s_1+M_{G1}+v_0}\right] + \frac{C_M M_Q}{s_q+M+v_0}$
$\frac{dL_1}{dt}$	x_h	0	0	x_h	0
$\frac{dL_2}{dt}$	0	0	0	0	x_m

Acidotic Spheroid: Partial Derivatives (c)					
	$\frac{\partial}{\partial M_S}$	$\frac{\partial}{\partial M_{G2}}$	$\frac{\partial}{\partial M_Q}$	$\frac{\partial}{\partial L_1}$	$\frac{\partial}{\partial L_2}$
$\frac{dG_1}{dt}$	0	0	0	0	$-\frac{\partial(D_2)}{\partial L_2} G_1$
$\frac{dS}{dt}$	0	0	0	0	$-\frac{\partial(D_2)}{\partial L_2} S$
$\frac{dG_2}{dt}$	0	0	0	0	$-\frac{\partial(D_2)}{\partial L_2} G_2$
$\frac{dQ}{dt}$	0	0	0	$-\frac{\partial(D_1)}{\partial L_1} Q$	0
$\frac{dN}{dt}$	D_4	D_4	D_3	$\frac{\partial(D_1)}{\partial L_1} Q + \frac{\partial(D_3)}{\partial L_1}(A_H + M_Q)$	$\frac{\partial(D_2)}{\partial L_2} P + \frac{\partial(D_4)}{\partial L_2} M$
$\frac{dT}{dt}$	0	0	0	0	0
$\frac{dA_H}{dt}$	0	0	0	$-\frac{\partial(D_3)}{\partial L_1} A_H$	0
$\frac{dM_{G1}}{dt}$	0	$2k_2$	0	0	$-\frac{\partial(D_4)}{\partial L_2} M_{G1}$
$\frac{dM_S}{dt}$	$-k_s - \frac{C_M M_Q}{s_q+M+v_0} - k_f F - D_4$	$-\frac{C_M M_Q}{s_q+M+v_0}$	C_M	0	$-\frac{\partial(D_4)}{\partial L_2} M_S$
$\frac{dM_{G2}}{dt}$	k_2	$-k_2 - d_a - k_f F - D_4$	0	0	$-\frac{\partial(D_4)}{\partial L_2} M_{G2}$
$\frac{dM_Q}{dt}$	$\frac{C_M M_Q}{s_q+M+v_0}$	$\frac{C_M M_Q}{s_q+M+v_0}$	$-C_M - D_3$	$-\frac{\partial(D_3)}{\partial L_1} M_Q$	0
$\frac{dL_1}{dt}$	0	0	x_h	$-l$	l
$\frac{dL_2}{dt}$	x_m	x_m	0	l	$-l - q$

Full Model Partials

Full Model: Partial Derivatives (a)		
	$\frac{\partial}{\partial G_1}$	$\frac{\partial}{\partial S}$
$\frac{dG_1}{dt}$	$-c_1 - c_f F - D_2$	0
$\frac{dS}{dt}$	$c_1 B\left[1 - \frac{G_1}{s_1+G_1+v_0+V}\right] - \frac{CQ}{s_q+P+v_0+c_{qs}V}$	$-c_s - \frac{CQ}{s_q+P+v_0+c_{qs}V} - c_f F - D_2$
$\frac{dG_2}{dt}$	0	c_s
$\frac{dQ}{dt}$	$c_1\left[1 - B + \frac{BG_1}{s_1+G_1+v_0+V}\right] + \frac{CQ}{s_q+P+v_0+c_{qs}V} - \frac{ef_hVQ}{(s_h+f_hP+g_hQ+V)^2}$	$\frac{CQ}{s_q+P+v_0+c_{qs}V} - \frac{ef_hVQ}{(s_h+f_hP+g_hQ+V)^2}$
$\frac{dN}{dt}$	$\frac{ef_hVQ}{(s_h+f_hP+g_hQ+V)^2} + D_2$	$\frac{ef_hVQ}{(s_h+f_hP+g_hQ+V)^2} + D_2$
$\frac{dT}{dt}$	0	0
$\frac{dR}{dt}$	$c_R\frac{T}{s_R+T}$	$c_R\frac{T}{s_R+T}$
$\frac{dV}{dt}$	0	0
$\frac{dA_H}{dt}$	0	0
$\frac{dM_{G1}}{dt}$	0	0
$\frac{dM_S}{dt}$	0	0
$\frac{dM_{G2}}{dt}$	0	0
$\frac{dM_Q}{dt}$	0	0
$\frac{dL_1}{dt}$	0	0
$\frac{dL_2}{dt}$	0	0

Full Model: Partial Derivatives (b)				
	$\frac{\partial}{\partial G_2}$	$\frac{\partial}{\partial Q}$	$\frac{\partial}{\partial N}$	$\frac{\partial}{\partial T}$
$\frac{dG_1}{dt}$	$2c_2$	0	0	$-\frac{c_f s_n}{(s_n+T)^2} G_1$
$\frac{dS}{dt}$	$-\frac{CQ}{s_q+P+v_0+c_{qs}V}$	C	0	$-\frac{c_f s_n}{(s_n+T)^2} S$
$\frac{dG_2}{dt}$	$-c_2 - d_a - c_f F - D_2$	0	0	$-\frac{c_f s_n}{(s_n+T)^2} G_2$
$\frac{dQ}{dt}$	$\frac{CQ}{s_q+P+v_0+c_{qs}V} - \frac{e f_h VQ}{(s_h+f_h P+g_h Q+V)^2}$	$-C - D_1 - a_h q_3 - e(H + \frac{\partial H}{\partial Q} Q)$	0	0
$\frac{dN}{dt}$	$\frac{e f_h VQ}{(s_h+f_h P+g_h Q+V)^2} + D_2$	$e(H + \frac{\partial H}{\partial Q} Q) + D_1$	$-m(v_0 + V)$	0
$\frac{dT}{dt}$	0	0	j	$-k(v_0 + V)$
$\frac{dR}{dt}$	$c_r \frac{T}{s_R+T}$	c_{qv}	0	$\frac{c_R s_R}{(s_R+T)^2}(P + M)$
$\frac{dV}{dt}$	0	0	0	0
$\frac{dA_H}{dt}$	0	$a_h q_3$	0	0
$\frac{dM_{G1}}{dt}$	0	0	0	$-\frac{k_f s_n}{(s_n+T)^2} M_{G1}$
$\frac{dM_S}{dt}$	0	0	0	$-\frac{k_f s_n}{(s_n+T)^2} M_S$
$\frac{dM_{G2}}{dt}$	0	0	0	$-\frac{k_f s_n}{(s_n+T)^2} M_{G2}$
$\frac{dM_Q}{dt}$	0	0	0	0
$\frac{dL_1}{dt}$	0	x_h	0	0
$\frac{dL_2}{dt}$	0	0	0	0

Full Model: Partial Derivatives (c)		
	$\frac{\partial}{\partial R}$	$\frac{\partial}{\partial V}$
$\frac{dG_1}{dt}$	0	0
$\frac{dS}{dt}$	0	$c_1 \frac{s_1+G_1}{(s_1+G_1+v_0+V)^2} G_1 + \frac{c_{qs}(s_q+P)}{(s_q+P+v_0+V)^2} Q$
$\frac{dG_2}{dt}$	0	0
$\frac{dQ}{dt}$	0	$-c_1 \frac{s_1+G_1}{(s_1+G_1+v_0+V)^2} G_1 - \frac{c_{qs}(s_q+P)}{(s_q+P+v_0+V)^2} Q + e \frac{s_h+f_h P+g_h Q}{(s_h+f_h P+g_h Q+V)^2} Q$
$\frac{dN}{dt}$	0	$-e \frac{s_h+f_h P+g_h Q}{(s_h+f_h P+g_h Q+V)^2} Q - mN$
$\frac{dT}{dt}$	0	-kT
$\frac{dR}{dt}$	$-q_R(v_0 + V)$	$-q_R R$
$\frac{dV}{dt}$	$\frac{c_v(1-D_V)(v_0+V)}{s_v+R+v_0+V}\left[1 - \frac{R}{s_v+R+v_0+V}\right]$	$c_v \frac{(s_v+R)R}{(s_v+R+v_0+V)^2}(1 - D_V) - D_V$
$\frac{dA_H}{dt}$	0	0
$\frac{dM_{G1}}{dt}$	0	0
$\frac{dM_S}{dt}$	0	$k_1 \frac{s_1 M_{G1}}{(s_1+M_{G1}+v_0+V)^2} M_{G1} + \frac{c_{qm}(s_q+M)}{(s_q+M+v_0+c_{qm}V)^2} M_Q$
$\frac{dM_{G2}}{dt}$	0	0
$\frac{dM_Q}{dt}$	0	$-k_1 \frac{s_1 M_{G1}}{(s_1+M_{G1}+v_0+V)^2} M_{G1} - \frac{c_{qm}(s_q+M)}{(s_q+M+v_0+c_{qm}V)^2} M_Q$
$\frac{dL_1}{dt}$	0	0
$\frac{dL_2}{dt}$	0	$q(3.9810717 \times 10^{-14} - L_2)$

Full Model: Partial Derivatives (d)			
	$\frac{\partial}{\partial A_H}$	$\frac{\partial}{\partial M_{G1}}$	$\frac{\partial}{\partial M_S}$
$\frac{dG_1}{dt}$	0	0	0
$\frac{dS}{dt}$	0	0	0
$\frac{dG_2}{dt}$	0	0	0
$\frac{dQ}{dt}$	0	0	0
$\frac{dN}{dt}$	D_3	D_4	D_4
$\frac{dT}{dt}$	0	0	0
$\frac{dR}{dt}$	c_{qv}	$c_R \frac{T}{s_R+T}$	$c_R \frac{T}{s_R+T}$
$\frac{dV}{dt}$	0	0	0
$\frac{dA_H}{dt}$	$c_{ga} - m_h - D_3$	0	0
$\frac{dM_{G1}}{dt}$	0	$-k_1 - k_f F - D_4$	0
$\frac{dM_S}{dt}$	0	$k_1 B_M \left[1 - \frac{M_{G1}}{(s_1+M_{G1}+v_0+V)}\right] - \frac{C_M M_Q}{s_q+M+v_0+c_{qs}V}$	$-k_s - \frac{C_M M_Q}{s_q+M+v_0+c_{qs}V} - k_f F - D_4$
$\frac{dM_{G2}}{dt}$	0	0	k_s
$\frac{dM_Q}{dt}$	m_h	$k_1 \left[1 - B_M + \frac{B_M M_{G1}}{(s_1+M_{G1}+v_0+V)}\right] + \frac{C_M M_Q}{s_q+M+v_0+c_{qs}V}$	$\frac{C_M M_Q}{s_q+M+v_0+c_{qs}V}$
$\frac{dL_1}{dt}$	x_h	0	0
$\frac{dL_2}{dt}$	0	x_m	x_m

Full Model: Partial Derivatives (e)				
	$\frac{\partial}{\partial M_{G2}}$	$\frac{\partial}{\partial M_Q}$	$\frac{\partial}{\partial L_1}$	$\frac{\partial}{\partial L_2}$
$\frac{dG_1}{dt}$	0	0	0	$-\frac{\partial(D_2)}{\partial L_2} G_1$
$\frac{dS}{dt}$	0	0	0	$-\frac{\partial(D_2)}{\partial L_2} S$
$\frac{dG_2}{dt}$	0	0	0	$-\frac{\partial(D_2)}{\partial L_2} G_2$
$\frac{dQ}{dt}$	0	0	$-\frac{\partial(D_1)}{\partial L_1} Q$	0
$\frac{dN}{dt}$	D_4	D_3	$\frac{\partial(D_1)}{\partial L_1} Q + \frac{\partial(D_3)}{\partial L_1}(A_H + M_Q)$	$\frac{\partial(D_2)}{\partial L_2} P + \frac{\partial(D_4)}{\partial L_2} M$
$\frac{dT}{dt}$	0	0	0	0
$\frac{dR}{dt}$	$c_R \frac{T}{s_R+T}$	c_{qv}	0	0
$\frac{dV}{dt}$	0	0	0	$-\frac{\partial(D_V)}{\partial L_2} \left[c_v \frac{R(v_0+V)}{s_v+R+v_0+V} + V\right]$
$\frac{dA_H}{dt}$	0	0	$-\frac{\partial(D_3)}{\partial L_1} A_H$	0
$\frac{dM_{G1}}{dt}$	$2k_2$	0	0	$-\frac{\partial(D_4)}{\partial L_2} M_{G1}$
$\frac{dM_S}{dt}$	$-\frac{C_M M_Q}{s_q+M+v_0+c_{qs}V}$	C_M	0	$-\frac{\partial(D_4)}{\partial L_2} M_S$
$\frac{dM_{G2}}{dt}$	$-k_2 - d_a - k_f F - D_4$	0	0	$-\frac{\partial(D_4)}{\partial L_2} M_{G2}$
$\frac{dM_Q}{dt}$	$\frac{C_M M_Q}{s_q+M+v_0+c_{qs}V}$	$-C_M - D_3$	$-\frac{\partial(D_3)}{\partial L_1} M_Q$	0
$\frac{dL_1}{dt}$	0	x_h	$-l$	l
$\frac{dL_2}{dt}$	x_m	0	l	$-l - q(v_1 + V)$

Appendix IV

Spheroid Genetic Algorithm Solver

```
1
2  function [] = solve_tramp_spheroidGenetic
3
4  close all
5  clear all
6
7  c1 = 1.961763658; %Ghosh et al. Role of RhoA activation in
       the growth and morphology of a murine prostate tumor cell
       line
8  c2 = 7.151991545; %Ghosh et al. Role of RhoA activation in
       the growth and morphology of a murine prostate tumor cell
       line
9  da = 0; %There is no notable data recording apoptosis so I
       take it as zero
10 cf = 0.001;
11 e = 0.419;
12 m = 0.028;
13 j = 3;
14 k = .05;
15 s1 = 1.2;
16 cq = 75;
17 sq = 270;
18 sn = 1000;
19 v0 = 2.76;
20 cs = 3.220357473; %Ghosh et al. Role of RhoA activation in
       the growth and morphology of a murine prostate tumor cell
       line
```

```
21
22 parVec = [c1 c2 da cf e m j k s1 cq sq sn v0 cs];
23 numPars = length(parVec);
24 parameterRanges = zeros(2,numPars);
25 parameterRanges(1,1:2) = parVec(1:2);
26 parameterRanges(2,1:2) = parVec(1:2);
27 parameterRanges(1,14) = parVec(14);
28 parameterRanges(2,14) = parVec(14);
29 parameterRanges(1,3:13) = parVec(3:13)/10;
30 parameterRanges(2,3:13) = parVec(3:13)*10;
31 parameterRanges(1,8) = parVec(8)/100;
32 parameterRanges(1,4) = parVec(4)/100;
33
34 %% Initialization Algorithm
35 individuals = 1000; % note, this MUST be divisible by 4
36 generations = 1000;
37 emptyMat = zeros(individuals,numPars+1);
38 parMat = emptyMat;
39
40 % Time
41 Tf = 60; %total time in days
42 dt = .01; %time step
43 tspan = 0:dt:Tf; %time span with Tf days incrementing by time
       step dt
44
45 % Intial Conditions
46 G10 = 0.5955*0.6; %Determined from the percentages in Ghosh
     et al. and volume in Enmon et al.
47 S0 = 0.2883*0.6; %Determined from the percentages in Ghosh et
       al. and volume in Enmon et al.
48 G20 = 0.1163*0.6; %Determined from the percentages in Ghosh
     et al. and volume in Enmon et al.
49 Q0 = 0; %The radius is small so I assume all cells are
     receiving oxygen
50 N0 = 0; %If there is no hypoxia there is likely no necrosis
51 T0 = 0; %No necrotic cells no produce TNF-alpha
52
53 x0 = [G10 S0 G20 Q0 N0 T0];
54
55 saveParamList = zeros(generations, numPars+1);
```

```
56
57 % Data
58 BallangrudW = [4.155 4.7221; 9.686 34.24; 16.36 166.8; 21.82
       391.6; 28.62 792.1; 34.15 1152; 45 1770; 55.57 2165];%; 0
       0.6; 55.57 2165];
59 BallangrudN = [8.766043512 7986447.935/10^6; 14.23231661
       47079589.16/10^6];
60 BallangrudQ = [8.766043512 11312160.25/10^6; 14.23231661
       30644226/10^6];
61 BallangrudP = [8.766043512 14211713.46/10^6; 14.23231661
       35373520.37/10^6];
62
63 % initializes a parameter matrix within the presented ranges
       above
64 for i = 1:individuals
65     for hj = 1:numPars
66         parMat(i,hj) = parameterRanges(1,hj)+((
               parameterRanges(2,hj)-parameterRanges(1,hj))*rand
               (1,1));
67     end
68 end
69
70 parMat(1,:) = [parVec 0];
71 % [1.96176365800000 7.15199154500000 0 0.0100000000000000
       0.424436140690927 0.0286306389614026 0.452839322174707
       0.000500000000000000 1.57028445806767 76.2775807224025
       260.396218587230 605.851505759063 2.79087965840100
       3.22035747300000 0];
72
73 %% Execute the Algorithm
74
75 for gen = 1:generations
76     % reinitialization
77     tournamentVec = randperm(individuals);
78     reprodVec = randperm(individuals/2);
79
80     if gen == 1
81         start = 1;
82     else
83         start = individuals/2+1;
```

```
84          parMat(1:individuals,1:numPars+1) = fitMat;
85      end
86
87      for i = start:individuals
88
89          [t,x] = ode45(@math27_TumorModel_spheroid, tspan, x0,
                []), parMat(i,:));
90          G1 = x(:,1);
91          S = x(:,2);
92          G2 = x(:,3);
93          Q = x(:,4);
94          N = x(:,5);
95
96          P = G1 + S + G2;
97          W = G1+S+G2+Q+N;
98
99          parMat(i,numPars + 1) = fitFun(dt,P,BallangrudP,Q,
                BallangrudQ,N,BallangrudN,W,BallangrudW);
100 %          parMat(:,1:numPars) = fitMat(:,1:numPars);
101
102     end
103
104     fitMat = zeros(individuals,numPars+1);
105
106     % competition
107     for pr = 0:2:individuals-2
108
109         tournamentA = tournamentVec(pr+1);
110         genA = parMat(tournamentA,1:numPars);
111         fitA = parMat(tournamentA,numPars+1);
112
113         tournamentB = tournamentVec(pr+2);
114         genB = parMat(tournamentB,1:numPars);
115         fitB = parMat(tournamentB,numPars+1);
116
117         if fitA < fitB
118             fitMat(pr/2+1,1:numPars) = genA;
119             fitMat(pr/2+1,numPars+1) = fitA;
120         else
121             fitMat(pr/2+1,1:numPars) = genB;
```

```
122             fitMat(pr/2+1,numPars+1) = fitB;
123         end
124     end
125     fitMat = sortrows(fitMat(1:individuals/2,:),numPars+1);
126
127     % reproduction, selects parameters from either parent
128     for i = 1:2:individuals/2-1
129
130         reprodA = reprodVec(i);
131         reprodB = reprodVec(i+1);
132
133         for changeLoop = 1:numPars
134             genRpos = ((i-1)/2)+(individuals/2) + 1;
135             parentPick = cat(1,(fitMat(reprodA,:)),(fitMat(
                    reprodB,:)));
136             fitMat(genRpos,changeLoop) = parentPick(randi(2),
                    changeLoop);
137         end
138     end
139
140
141     % mutation
142     for m = 3/4*individuals+1:individuals
143
144         indivMutant = reprodVec(m-3/4*individuals);
145         parMutant = randi(numPars);
146         fitMat(m,1:numPars) = fitMat(indivMutant,1:numPars);
147         fitMat(m,parMutant) = 2*rand(1,1) * fitMat(
                indivMutant,parMutant);
148
149         if fitMat(m,parMutant) < parameterRanges(1,parMutant)
150             fitMat(m,parMutant) = parameterRanges(1,parMutant
                    );
151         elseif fitMat(m,parMutant) > parameterRanges(2,
                parMutant)
152             fitMat(m,parMutant) = parameterRanges(2,parMutant
                    );
153         end
154     end
155
```

```
156     %picking the fittest to plot from first half of
            individuals
157     fit = fitMat(1,numPars+1);
158
159     bestParVec = fitMat(1,1:numPars);
160     [t,x] = ode45(@math27_TumorModel_spheroid, tspan, x0, [],
            bestParVec);
161     G1 = x(:,1);
162     S = x(:,2);
163     G2 = x(:,3);
164     Q = x(:,4);
165     N = x(:,5);
166     T = x(:,6);
167     P = G1 + S + G2;
168     W = G1+S+G2+Q+N;
169
170     namestr = ['Change in Spheroid Volume No Treatment - ',
            num2str(gen)];
171
172     figure (1)
173     clf(figure(1))
174     axes('FontName', 'Times New Roman', 'FontSize', 16)
175     plot(t, P, 'b', 'LineWidth',1.5);
176     hold on
177     plot(t, Q, 'g', 'LineWidth',1.5);
178     hold on
179     plot(t, N, 'r', 'LineWidth',1.5);
180     hold on
181     plot(t, W, 'k', 'LineWidth',1.5);
182     hold on
183     plot(BallangrudP(:,1), BallangrudP(:,2), '*b', '
            MarkerSize',6);
184     hold on
185     plot(BallangrudQ(:,1), BallangrudQ(:,2), '*g', '
            MarkerSize',6);
186     hold on
187     plot(BallangrudN(:,1), BallangrudN(:,2), '*r', '
            MarkerSize',6);
188     hold on
```

```
189     plot(BallangrudW(:,1), BallangrudW(:,2), '*k', '
            MarkerSize',6);
190     hold on
191     ylim([0 2300])
192     xlabel('Time in Days','FontSize', 13);
193     ylabel('Volume (um^3*10^6)','FontSize', 13);
194     l2=legend('Proliferating', 'Quiescent', 'Necrotic','Whole
            ','Location','northwest');
195     title(namestr);
196     set(l2, 'FontSize', 12);
197     text(0.3,0.65*2300,[' rMSE: ',num2str(fit)])
198     drawnow
199     pause(0.001)
200
201     printPNG(figure(1),['SpheroidFitAcid-',num2str(gen),'.png
            ']);
202
203     saveParamList(gen,:) = [bestParVec fit];
204     save('paramTrialScaleShift','saveParamList')
205 end
206 figure (2)
207 clf(figure(2))
208 axes('FontName', 'Times New Roman', 'FontSize', 16)
209 plot(t, P, 'b', 'LineWidth',1.5);
210 hold on
211 plot(t, Q, 'g', 'LineWidth',1.5);
212 hold on
213 plot(t, N, 'r', 'LineWidth',1.5);
214 hold on
215 plot(t, W, 'k', 'LineWidth',1.5);
216 hold on
217 plot(BallangrudP(:,1), BallangrudP(:,2), '*b', 'MarkerSize'
        ,6);
218 hold on
219 plot(BallangrudQ(:,1), BallangrudQ(:,2), '*g', 'MarkerSize'
        ,6);
220 hold on
221 plot(BallangrudN(:,1), BallangrudN(:,2), '*r', 'MarkerSize'
        ,6);
222 hold on
```

```
223 plot(BallangrudW(:,1), BallangrudW(:,2), '*k', 'MarkerSize'
    ,6);
224 hold on
225 xlim([0 20])
226 ylim([0 175])
227 xlabel('Time in Days','FontSize', 13);
228 ylabel('Volume (um^3*10^6)','FontSize', 13);
229 l2=legend('Proliferating', 'Quiescent', 'Necrotic','Whole','
    Location','northwest');
230 title(namestr);
231 set(l2, 'FontSize', 12);
232 text(0.3,0.65*2300,[' rMSE: ',num2str(fit)])
233 drawnow
234 pause(0.001)
235
236 printPNG(figure(2),['SpheroidFitAcidZoom-','.png']);
237 end
```

Spheroid Equation Input

```
function dxdt = tramp_spheroid(~, x, par)

dxdt = NaN(6,1);

G1 = x(1); %Proliferating Tumor Cells G1 Stage
S = x(2); %Proliferating Tumor Cells S Stage
G2 = x(3); %Proliferating Tumor Cells G2 Stage
Q = x(4); %Quiescent Cells
N = x(5); %Necrotic/Hypoxic Cells
T = x(6); %TNF-alpha

% Constant Parameters
c1 = par(1);
c2 = par(2);
da = par(3);
cf = par(4);
e = par(5);
m = par(6);
j = par(7);
k = par(8);
s1 = par(9);
cq = par(10);
sq = par(11);
sn = par(12);
v0 = par(13);
cs = par(14);

% Proliferating Tumor Cells
P = G1+S+G2; %Proliferative Region
W = G1+S+G2+Q+N; %Whole Tumor

% Function Parameters
B = (v0)./(s1+G1+(v0));
C = cq.*(v0)./(sq+P+v0);
H = 1;
F = T./(sn+T);

% Model Equations
```

```
39 dxdt(1) = 2.*c2.*G2-c1.*B.*G1-c1.*(1-B).*G1-cf.*F.*G1; % G1
40 dxdt(2) = c1*B.*G1-cs.*S+C.*Q-cf.*F.*S; % S
41 dxdt(3) = cs.*S-c2.*G2-da*G2-cf.*F.*G2; % G2
42 dxdt(4) = c1.*(1-B).*G1-C.*Q-e*H*Q; % Q
43 dxdt(5) = e.*H.*Q- m*v0*N; % N
44 dxdt(6) = (j.*N) - (k*v0*T); % T
45
46 end
```

Fitness Function

```
function fitness = fitFun(tStep,model1,data1,model2,data2,
    model3,data3,model4,data4)
% rMSE = ((s-d)/d)^2

switch nargin
    case 3 % this is what we used for xenograft where 1 is
        whole volume
        modelTime1 = round(data1(:,1)/tStep,0);
        RMSE1 = sum(((model1(modelTime1)-data1(:,2))./(data1
            (:,2))).^2);

        fitness = RMSE1;

    case 5
        modelTime1 = round(data1(:,1)/tStep,0);
        RMSE1 = sum(((model1(modelTime1)-data1(:,2))./(data1
            (:,2))).^2);

        modelTime2 = round(data2(:,1)/tStep,0);
        RMSE2 = sum(((model2(modelTime2)-data2(:,2))./(data2
            (:,2))).^2);

        fitness = RMSE1 + RMSE2;

    case 7 %this is what we used for spheroid
        % 1 is proliferative, 2 is quiescent, 3 is necrotic

        modelTime1 = round(data1(:,1)/tStep,0);
        RMSE1 = sum(((model1(modelTime1)-data1(:,2))./(data1
            (:,2))).^2);

        modelTime2 = round(data2(:,1)/tStep,0);
        RMSE2 = sum(((model2(modelTime2)-data2(:,2))./(data2
            (:,2))).^2);

        modelTime3 = round(data3(:,1)/tStep,0);
        RMSE3 = sum(((model3(modelTime3)-data3(:,2))./(data3
            (:,2))).^2);
```

```
31
32          fitness = 5*RMSE1 + RMSE2 + RMSE3;
33
34      case 9
35          modelTime1 = round(data1(:,1)/tStep,0);
36          RMSE1 = sum(((model1(modelTime1)-data1(:,2))./(data1
                (:,2))).^2);
37
38          modelTime2 = round(data2(:,1)/tStep,0);
39          RMSE2 = sum(((model2(modelTime2)-data2(:,2))./(data2
                (:,2))).^2);
40
41          modelTime3 = round(data3(:,1)/tStep,0);
42          RMSE3 = sum(((model3(modelTime3)-data3(:,2))./(data3
                (:,2))).^2);
43
44          modelTime4 = round(data4(:,1)/tStep,0);
45          RMSE4 = sum(((model4(modelTime4)-data4(:,2))./(data4
                (:,2))).^2);
46
47          fitness = 3*RMSE1 + 3*RMSE2 + 3*RMSE3 + RMSE4;
48  end
49  end
```